Instabilities in Multiphysics Problems: Micro- and Nano-electromechanical Systems, and Heat-Conducting Thermoelastoviscoplastic Solids

Davide Spinello

Dissertation submitted to the Faculty of the
Virginia Polytechnic Institute and State University
in partial fulfillment of the requirements for the degree of

Doctor of Philosophy
in
Engineering Mechanics

Prof. Romesh C. Batra, Chair
Prof. Scott W. Case
Prof. Edmund G. Henneke
Prof. Michael W. Hyer
Prof. Robert C. Rogers

August 28, 2006
Blacksburg, Virginia

Keywords: MEMS, NEMS, Multiphysics,
Instabilities, Thermoelastoviscoplasticity,
Meshless methods

Instabilities in Multiphysics Problems: Micro- and Nano-electromechanical Systems, and Heat-Conducting Thermoelastoviscoplastic Solids

Davide Spinello

(Abstract)

We investigate (i) pull-in instabilities in a microelectromechanical (MEM) beam due to the Coulomb force and in MEM membranes due to the Coulomb and the Casimir forces, and (ii) thermomechanical instability in a heat-conducting thermoelastoviscoplastic solid due to thermal softening overcoming hardening caused by strain- and strain-rate effects. Each of these nonlinear multiphysics problems is analyzed by the meshless local Petrov-Galerkin (MLPG) method. The moving least squares (MLS) approximation is used to generate basis functions for the trial solution, and the basis for test functions is taken to be either the weight functions used in the MLS approximation, or the same as for the trial solution. In this case the method becomes Bubnov-Galerkin. Essential (displacement, temperature, electric potential) boundary conditions are enforced by the method of Lagrange multipliers. For the electromechanical problem, the pull-in voltage and the corresponding deflection are extracted by combining the MLPG method with either the displacement iteration pull-in extraction algorithm or the pseudoarclength continuation method. For the thermomechanical problem, the localization of deformation into narrow regions of intense plastic deformation is delineated. For every problem studied, computed results are found to compare well with those obtained either analytically or by the finite element (FE) method. For the same accuracy, the MLPG method generally requires fewer nodes but more CPU time than the FE method; thus additional computational cost is compensated somewhat by the increased efficiency of the MLPG method.

Acknowledgments

I wish to express my first acknowledgement to my advisor, Dr. Romesh C. Batra. Under his guidance and his continuous support throughout the years of my doctoral studies, I had the great privilege to dedicate myself to research. I was motivated by his example towards excellence, and enlightened by his passion for science.

I express my deepest gratitude to my parents, my brothers, my sister, my late grandfathers, my grandmothers, and my entire family for their never ending unconditional support and encouragement. They gave me the unique opportunity to dedicate myself to studies.

I would like to thank my other committee members, Dr. Edmund G. Henneke, Dr. Scott W. Case, Dr. Michael W. Hyer, and Dr. Robert C. Rogers, and the entire faculty and staff of the Engineering Science & Mechanics department for giving me the chance to complete my studies in this wonderful institution. I also would like to thank my colleagues working with Dr. Batra for their valuable help and suggestions. I wish them all the best of luck for their future.

The dissertation would not be complete without the collaboration over the past few years with my friend and colleague Dr. Maurizio Porfiri. The scientific interaction with him and his friendship represent for me a unique experience.

I also would like to express my gratitude to all my friends in my home country (Italy), and to all my international friends met during my stay at Virginia Tech for the great time I could spend with them.

This work was partially supported by the ONR grants N0014-1-98-0300 and N0014-06-0567 to Virginia Polytechnic Institute & State University with Dr. Batra as the principal investigator. Views expressed herein are those of the author and neither of the ONR nor of Virginia Polytechnic Institute & State University.

Contents

List of Figures

List of Tables

Chapter 1

Pull-in instability in electrostatically actuated MEMS

1.1 Introduction

Recent technological developments have opened promising research opportunities and engineering priorities in micromechanics. It is now possible to manufacture mechanical parts such as resonators, sensors, gears, and levers on a micron length scale, and to produce tiny needles to inject fluid into a living organism without stimulating nerve cells. The use of existing integrated circuit technology in the design and production of microelectromechanical systems (MEMS) allows these devices to be batch-manufactured thereby reducing the production cost.

The thorough understanding, prediction, and control of MEMS behavior at the micro scale are critical issues in their design. Multiphysics modeling is required, since coupling among different fields such as solid and fluid mechanics, thermomechanics, and electromagnetism is involved.

MEMS devices find wide applications as sensors and actuators. The analysis of methods of actuation and sensing has been a topic of interest over the past several years. Different actuation and sensing properties such as piezoresistive, piezoelectric, electrostatic, thermal, electromagnetic, and optical have been used (see e.g. Fargas Marquès, Costa Castelló & Shkel (2005) for details). Comparisons among the aforementioned techniques in relation to the fabrication methods can be found in Fargas Marquès et al. (2005), and Burns, Zook, Horning, Herb & Guckel (1995). There is no one optimal sensing and actuating method, and the choice mainly depends on the particular application.

Electrostatics is often the preferred sensing and actuating technique (Fargas Marquès et al. (2005)). An electrostatically actuated MEMS is generally an elastic perfect conductor sus-

pended above a stationary rigid perfect conductor (see e.g. Pelesko & Bernstein (2002)). A dielectric medium, usually air, fills the gap between them. The overall system behaves as a variable gap capacitor. An applied DC voltage is used to induce displacements of the deformable body, and a consequent change in the system capacitance. Typical applications are transistors, switches, micro-mirrors, pressure sensors, micro-pumps, moving valves and micro-grippers, see e.g. Newell (1968), Nguyen, Katehi & Rebeiz (1998), Juneau, Unterkofler, Seliverstov, Zhang & Judy (2003), Hung & Senturia (1999), Gupta & Senturia (1997), Teymoory & Abbaspour-Sany (2002), and Chu, Nelson, Tachiki & Pister (1996). When an AC component is superimposed on the steady voltage to excite harmonic motions of the system, resonant devices are obtained. These devices are used in signal filtering, and chemical and mass sensing, see e.g. Abdel-Rahman, Younis & Nayfeh (2002), Nayfeh & Younis (2005), Rhoads, Shaw & Turner (2006), Tilmans & Legtenberg (1994*b*), Younis & Nayfeh (2003), Krylov & Maimon (2004), Kuang & Chen (2004), and Xie, Lee & Lim (2003).

The applied electrostatic voltage has an upper limit, beyond which the corresponding electrostatic force is not balanced by the elastic restoring force in the deformable conductor that eventually snaps and touches the lower rigid plate, and the MEMS collapses. This phenomenon, called *pull-in instability*, was simultaneously observed experimentally by Taylor (1968), and Nathanson, Newell, Wickstrom & Davis (1967). The critical displacement field, and the critical voltage associated with this instability are called *pull-in displacement* and *pull-in voltage*. Their accurate estimate is crucial in the design of electrostatically actuated MEMS. In particular, in micro-mirrors (Hung & Senturia (1999)) and micro-resonators (Tilmans & Legtenberg (1994*a*)) the designer avoids this instability in order to achieve stable motions; on the other hand in switching applications (Nguyen et al. (1998)) the designer exploits this effect to optimize the performance of the device.

A simple lumped mass-spring system for estimating pull-in parameters has been proposed by Nathanson et al. (1967) (see Fig. 1.1). The elasticity of the deformable body is lumped into the spring stiffness κ, F_{S} is the spring restoring force, V is the applied voltage, F_{E} is the electrostatic force, m is the mass of the movable electrode, g_0 is the initial gap between the two conductors, $\bar{u}$ is the displacement of the movable electrode, and $g = g_0 + \bar{u}$ is the actual gap. This model qualitatively describes the pull-in phenomenon but it overestimates the pull-in voltages for many applications (Pamidighantam, Puers, Baert & Tilmans (2002)). Moreover, it does not incorporate the inherent nonlinearities of the electrostatic and the restoring forces (Chu et al. (1996), Castañer & Senturia (1999)).

Several researchers have focused on accurately predicting the pull-in parameters. Li & Aluru (2003) modeled the nonlinear coupling between electrical and mechanical effects by using a three-dimensional (3-D) nonlinear field theory. The governing equations for both the deformable body and the dielectric medium are written in Lagrangian description, and are

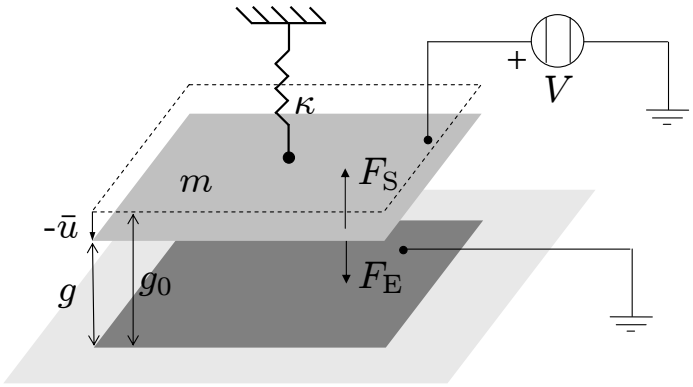

Figure 1.1: Sketch of the lumped mass-spring model.

solved numerically (Li & Aluru (2003), De & Aluru (2004)). Several computer algorithms based on 3-D finite element (FE) analysis have been developed (see e.g. Senturia, Harris, Johnson, Kim, Nabors, Shulman & White (1992), Shi, Ramesh & Mukherjee (1996)) and used to simulate MEMS (see e.g. Gabbay, Mehner & Senturia (2000), Pamidighantam et al. (2002)). Different computational techniques have been exploited in order to optimize algorithms used in the 3-D analyses, see e.g. Senturia, Aluru & White (1997).

In order to alleviate the computational expense associated with the 3-D analyses, considerable efforts have been devoted to the development of reliable distributed reduced-order models for MEMS. Theories of rods and strings (1-D), and plates, shells and membranes (2-D) can be derived intrinsically (see e.g. Antman (2004), Naghdi (1972)), or can be deduced from the 3-D theory (induced theories) (see e.g. Antman (2004), Naghdi (1980)).

For a wide class of electrostatic MEMS, the deformable electrode is initially a flat body, as shown in Fig. 1.2, whose thickness is much smaller than the characteristic length L (Pelesko & Triolo (2001)). Such electrodes can be regarded as 2-D plate-like bodies. Since the thickness is very small as compared to the characteristic length L, an approximate distributed model can be employed, where the kinematics is described only through the transverse displacement field u of points on its mid-surface (see e.g. Timoshenko (1970)). The actual gap g is therefore given by $g_0 + u$. Microplates have been studied by Francais & Dufour (1999), Ng, Jiang, Lam & Reddy (2004), and Zhao, Abdel-Rahman & Nayfeh (2004).

When the bending stiffness of the deformable electrode is negligible as compared to its in-plane stretching stiffness, and the initial gap is much smaller than the characteristic length L, it is possible to approximate the electrode as a linear elastic membrane. Mansfield (1989) has

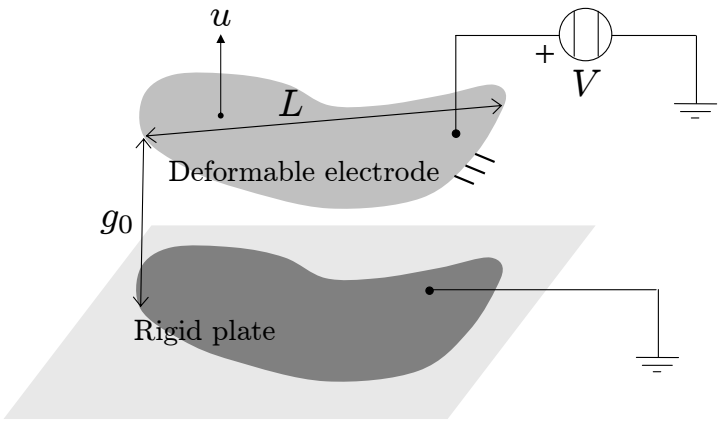

Figure 1.2: Geometry of an electrostatic MEMS with the plate-like body as the deformable electrode.

proposed that the membrane approximation is valid for $L/h \geq 400$. As discussed in Pelesko (2002), the membrane approximation is accurate and reliable for many MEMS devices such as micro-pumps made of thin glassy polymers, and grating light valves comprised of stretched thin ribbons.

For another class of electrostatic MEMS, the deformable electrode is a slender body with the length much larger than the others two dimensions (Fargas Marquès et al. (2005)). These MEMS can be modeled by a beam theory. When the deformable electrode is very slender, the transverse displacement u of a point of its mid-surface is sufficient to describe the kinematics within a good approximation (see e.g. Timoshenko (1970)). This 1-D distributed model may also be adopted for thin rectangular electrodes that undergo cylindrical bending. In this case, for symmetry reasons, the plate theory is equivalent to the beam theory.

From an electrical point of view, the variable gap capacitor equivalent to the 2-D and the 1-D structures described above is modeled by assuming that the actual gap g is differentially uniform, that is, the two conductors are locally parallel to each other. This assumption is consistent with the approximation introduced above in the mechanical models, see e.g. Pelesko & Bernstein (2002). This implies that the capacitance of the system (and therefore the applied electrostatic force) does not depend on the spatial derivatives of g.

Tilmans & Legtenberg (1994*b*) modeled a wide clamped-clamped microbeam with the Euler-Bernoulli beam theory. This assumption is justified for small deflections. Osterberg & Senturia (1997) employed an effective Young's modulus to account for the plane stress and the plane strain deformations appropriate for narrow and wide beams or plates undergoing cylindrical deformations respectively. Abdel-Rahman et al. (2002) studied large deflections

and accounted for the mid-plane stretching (see e.g. Landau & Lifshitz (1986) for details about the large displacement beam theory); they could thus analyze systems with initial gaps comparable to the thickness of the beam.

In the large deflection theory the governing equations are nonlinear, and the problem of numerically extracting the pull-in parameters is more challenging. The shooting method used by Abdel-Rahman et al. (2002) produces stiff differential equations whose solutions are sensitive to initial estimates of unknown parameters and may eventually diverge. Younis, Abdel-Rahman & Nayfeh (2003) employed two variants of the Galerkin method by using the beam mode shapes as basis functions. In the first variant the electrostatic force is expanded in Taylor series around its value in the undeformed configuration and terms up to the fifth order are retained. The second variant accounts for the exact electrostatic force. The value of the pull-in parameter computed with the first method does not agree well with that obtained with the shooting method. The pull-in parameter obtained from the second variant is very sensitive to the number of modes used as basis, and acceptable results are obtained only when an odd number of modes greater than one are included in the basis functions. The use of mode shapes as basis functions limits the applicability of the method to geometries for which eigenvalues and eigenfunctions can be easily computed. Kuang & Chen (2004) used the differential quadrature method; their computed results seem very accurate. Nevertheless, the global nature of the method seems to forbid its application to complex MEMS geometries.

The rest of the Chapter is organized as follows. In Sec. 1.2 we formulate the initial-boundary-value problem for an electromechanical system where the deformable electrode is modeled as 3-D perfect conductor undergoing finite deformations. The coupling phenomenon in a two conductors system is illustrated. Expressions for the electrostatic potential in the form of boundary integrals are given both in the Eulerian and the Lagrangian descriptions.

In Sec. 1.3 the meshless local Petrov-Galerkin (MLPG) method* is used to investigate the behavior of electrostatically actuated MEMS modeled as elastic membranes. In order to find the MEMS deformations beyond the pull-in instability the pseudoarclength continuation method (see e.g. Doedel, Keller & Kernevez (1991*a*), Doedel, Keller & Kernevez (1991*b*)) is employed for solving the system of nonlinear equations resulting from the MLPG formulation. The method is applied to four distinct geometries: a rectangle, a circular disk, an annular disk, and an elliptic disk. For rectangular geometry the effect of partial electrodes is studied. For the annular disk, symmetry breaking after pull-in instability is investigated. For the rectangular, circular, and annular nanomembranes the effect of the Casimir force on the pull-in parameters is analyzed. It is shown that beyond a certain size, the pull-in instability occurs at zero voltage. Symmetry breaking in annular nanomembranes due to the combined effects of the Coulomb and the Casimir forces is also analyzed.

*A very brief review of meshless methods is given in Chapter 2.

In Sec. 1.4 a consistent electromechanical model of a narrow microbeam, that accounts for its finite width and finite thickness is derived. Kuang & Chen's (2004) model is improved by retaining the large deflection theory and by introducing in it a novel capacitance estimate obtained by fitting data from a fully converged numerical solution obtained with the method of moments. An expression for the electrostatic force is established which accounts for the fringing field capacitance due to the finite width, the finite thickness, and the aspect ratio of the microbeam. The resulting nonlinear fourth-order ordinary differential equation is solved by two different methods: reducing the distributed system to a one-degree-of-freedom system, and solving governing equations of the continuous problem with the MLPG and the FE methods in conjunction with the displacement iteration pull-in extraction (DIPIE) algorithm developed in Bochobza-Degani, Elata & Nemirovsky (2002). The consistent electromechanical model is also used to study vibrations of narrow microbeams predeformed by an electric field. It is shown that the reduced one-degree-of-freedom model is able to reproduce results of the 3-D FE simulations, accurately estimate the pull-in parameters of a narrow microbeam, and capture the behavior of its fundamental frequency up to pull-in.

1.2 Formulation of the three-dimensional problem

1.2.1 Coupling in electromechanical systems

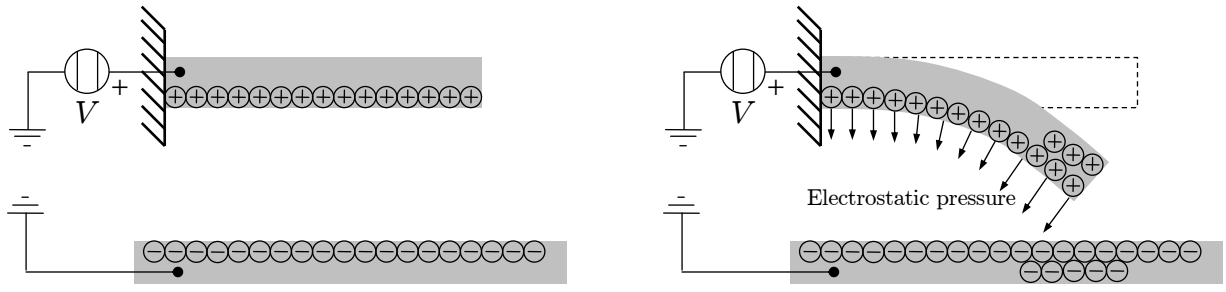

(a) (b)

Figure 1.3: Simple example to illustrate electromechanical coupling in electrostatic MEMS.

The following illustrative example to explain the coupling phenomenon in electromechanical systems is taken from Li & Aluru (2003). Consider the electrostatically actuated cantilever microbeam exhibited in Fig. 1.3. When potential difference V is applied between the top deformable electrode and the bottom ground plane, electrostatic charges are induced on

surfaces of the two conductors (Fig. 1.3(a)). These charges generate an electrostatic force acting along the normal to the bounding surface in the present configuration. Consequently the elastic body deforms, the charges redistribute on the surfaces of the conductors, and the electrostatic force changes (Fig. 1.3(b)). The process continues until a new equilibrium configuration is reached in which the electrostatic force is balanced by the internal forces in the deformed system.

1.2.2 Mechanical deformations

An electrostatically actuated MEMS can undergo large deformations depending on its geometry and the applied voltage. Here we briefly outline governing equations for large deformations of an electromechanical system where the deformable electrode is modeled as a 3-D continuum (see Li & Aluru (2003), De & Aluru (2004)).

Let Ω be the 3-D region occupied by the deformable electrode in the reference configuration. With respect to a set of rectangular Cartesian coordinate axes, let (x^1, x^2, x^3) and $(x^1_\star, x^2_\star, x^3_\star)$ be the coordinates of a material point in the reference and the present configurations respectively. Equilibrium equations in Lagrangian description are (Gurtin (1981))

$$\varrho_0(\ddot{\mathbf{u}} - \mathbf{b}) = \mathrm{Div}\mathbf{F}\mathbf{S}, \tag{1.1a}$$

$$\mathbf{S} = \mathbf{S}^{\mathrm{T}}. \tag{1.1b}$$

Eqs. (1.1a) and (1.1b) are the balance of linear momentum, and the balance of moment of momentum respectively. $\mathbf{S}$ is the second Piola-Kirchhoff stress tensor, $\mathbf{u} = \mathbf{x}_\star - \mathbf{x}$ the displacement field, and $\mathbf{F} = \mathbf{1} + \mathrm{Grad}\mathbf{u}$ the deformation gradient. $\mathbf{1}$ is the second-order identity tensor, ϱ_0 the mass density in the reference configuration, and $\mathbf{b}$ the external body force per unit mass. A superimposed dot means material derivative, and Div and Grad are the divergence and the gradient operators with respect to coordinates x^i in the reference configuration.

Assuming that the body is made of an elastic material, the constitutive equation for $\mathbf{S}$ is (Gurtin (1981))

$$\mathbf{S} = \hat{\mathbf{S}}(\mathbf{F}) \tag{1.2}$$

where $\hat{\mathbf{S}}$ represents the response of the material. The set of Eqs. (1.1)-(1.2) is completed with the following boundary conditions

$$\mathbf{u} = \bar{\mathbf{u}} \quad \text{on } \Gamma_{\mathbf{u}}, \tag{1.3a}$$

$$\mathbf{P}\mathbf{n} = \bar{\mathbf{t}} \quad \text{on } \Gamma_{\mathbf{n}}, \tag{1.3b}$$

and initial conditions

$$\mathbf{u}(\mathbf{x},0) = \mathbf{u}_0(\mathbf{x}), \tag{1.4a}$$

$$\dot{\mathbf{u}}(\mathbf{x},0) = \mathbf{v}_0(\mathbf{x}), \tag{1.4b}$$

where $\mathbf{n}$ is the outward unit normal in the reference configuration, $\mathbf{P} = \mathbf{FS}$ is the first Piola-Kirchhoff stress tensor, $\bar{\mathbf{t}}$ the surface traction per unit undeformed area, and $\Gamma_{\mathbf{u}}$ and $\Gamma_{\mathbf{n}}$ are parts of the boundary of Ω where displacements and tractions are prescribed respectively. Furthermore, $\mathbf{u}_0$ and $\mathbf{v}_0$ give, respectively, the initial displacement and the initial velocity fields.

We require that the total force on the boundary $\Gamma_{\mathbf{n}}$ equal the total force on the part $\Gamma_{\mathbf{n}^\star}$ of the present boundary into which $\Gamma_{\mathbf{n}}$ is deformed (Gurtin (1981)). Thus

$$\int_{\Gamma_{\mathbf{n}}} \bar{\mathbf{t}} \mathrm{d}\Gamma = \int_{\Gamma_{\mathbf{n}^\star}} f_{\mathrm{e}}^\star \mathbf{n}^\star \mathrm{d}\Gamma^\star, \tag{1.5}$$

where $\mathbf{n}^\star$ is the outward unit normal to the present boundary $\Gamma^\star$, and $f_{\mathrm{e}}^\star$ is the electrostatic pressure acting along the normal to $\Gamma^\star$. Eq. (1.5) embodies the constraint that the electrostatic pressure acts along the normal to the boundary, a consequence of the assumptions that the bodies are perfect conductors. Therefore, the traction $\bar{\mathbf{t}}$ is given by

$$\bar{\mathbf{t}} = f_{\mathrm{e}}(\det \mathbf{F})\mathbf{F}^{-\mathrm{T}}\mathbf{n}. \tag{1.6}$$

Here, $f_{\mathrm{e}}(\mathbf{x}) = f_{\mathrm{e}}^\star(\mathbf{x}_\star(\mathbf{x}))$, where the same symbol has been used to denote the function and its value. For brevity we will retain this notation in the remainder of this Chapter.

In order to solve the initial-boundary-value problem defined by Eqs. (1.1), (1.2), (1.3), and (1.4), we need an explicit form of the function $\hat{\mathbf{S}}$ in Eq. (1.2) and of f_{e} in Eq. (1.6). The simplest choice is to linearize the response function $\hat{\mathbf{S}}$ around $\mathbf{F} = \mathbf{1}$. In this case (see e.g. Batra (2005))

$$\mathbf{S} = \mathbf{S}^0 + \mathbf{C}\hat{\mathbf{E}} + \mathrm{O}(\|\hat{\mathbf{E}}^2\|), \tag{1.7}$$

where

$$2\hat{\mathbf{E}} = \mathrm{Grad}\mathbf{u} + (\mathrm{Grad}\mathbf{u})^{\mathrm{T}} + (\mathrm{Grad}\mathbf{u})^{\mathrm{T}}\,\mathrm{Grad}\mathbf{u}, \tag{1.8}$$

is the Green-St. Venant strain tensor, and $\lim_{\|\hat{\mathbf{E}}^2\|\to 0} \mathrm{O}(\|\hat{\mathbf{E}}^2\|)/\|\hat{\mathbf{E}}^2\| = \text{const.}$ $\mathbf{S}^0$ in Eq. (1.7) is the prestress in the reference configuration, and $\mathbf{C}$ is the fourth order elasticity tensor. When $\mathbf{S}^0 = \mathbf{0}$, and the material of the body is isotropic, Eq. (1.7) reduces to

$$\mathbf{S} = \hat{\lambda}(\mathrm{tr}\hat{\mathbf{E}})\mathbf{1} + 2\hat{\mu}\hat{\mathbf{E}}, \tag{1.9}$$

where $\hat{\lambda}$ and $\hat{\mu}$ are the moduli of the material. The form of the fourth order tensor $\mathbf{C}$ for transversely isotropic and orthotropic bodies is given in Batra (2005).

For small deformations the third term on the right hand side of Eq. (1.8) is neglected resulting in affine strain-displacement relation. Furthermore, for infinitesimal deformations, the distinction between different stress tensors and different strain tensors disappears, and Eq. (1.5) becomes $\bar{\mathbf{t}} = f_{\mathrm{e}}\mathbf{n}$.

In the remainder of this Chapter we will not consider the effect of body forces, and thus set $\mathbf{b} = \mathbf{0}$ in Eq. (1.1a). Furthermore, we will model deformable bodies as membranes and beams. Surface tractions $\bar{\mathbf{t}}$ on the top and the bottom surfaces of membranes usually appear as body forces in equations governing their deformations. For beam problems, the approach we will follow is similar to that used in structural mechanics to study Saint-Venant problems, see e.g. Iesan (1987). That is, deformations of a slender body are studied by initially solving a 2-D problem defined on the cross section and using these results to build a 1-D model of a beam with distributed loads acting along its length. Therefore, surface tractions due to the electrostatic pressure will appear as distributed forces in the governing equations.

We discuss below the evaluation of the electrostatic force f_{e} exerted on the boundary of a two-conductor system.

1.2.3 Electrostatic force

Consider the two-conductor system depicted in Fig. 1.4, where Ω_1 and Ω_2 are the 3-D regions of space occupied by the two conductors in their reference configurations, and $\Omega_1^\star$ and $\Omega_2^\star$ in their corresponding present configurations. The region exterior to $\Omega_1^\star \cup \Omega_2^\star$ is denoted by $\bar{\Omega}$. Boundaries of $\Omega_1^\star$ and $\Omega_2^\star$ are denoted by $\Gamma_1^\star$ and $\Gamma_2^\star$ respectively, and Γ_1 and Γ_2 are the corresponding ones in the reference configurations.

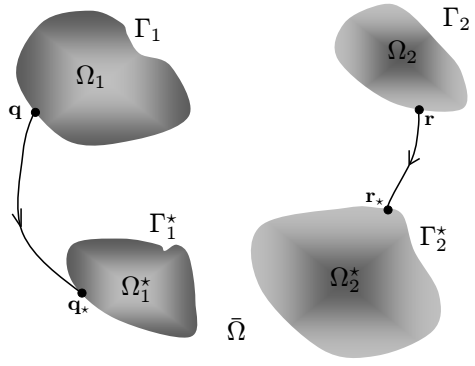

Figure 1.4: Two-conductor system.

The boundary-value problem for the electrostatic potential ϕ formulated in the present con-

figuration is (see e.g. Pelesko & Triolo (2001))

$$\begin{aligned} \triangle\phi &= 0 \quad \text{in } \bar{\Omega}, && \text{(1.10a)} \\ \phi &= \bar{\phi}_1 \quad \text{on } \Gamma_1^\star, && \text{(1.10b)} \\ \phi &= \bar{\phi}_2 \quad \text{on } \Gamma_2^\star, && \text{(1.10c)} \\ \phi &\to 0 \quad \text{as } |\mathbf{x}| \to \infty. && \text{(1.10d)} \end{aligned}$$

Here we have neglected inertia effects associated with the electric field because the speed of electric waves is considerably more than that of the mechanical waves. Thus ϕ is a harmonic function, and the boundary-value problem defined by Eqs. (1.10) is studied in the potential theory. It is likely that its solution will depend upon the decay rate of ϕ in Eq. (1.10d).

The solution of the boundary-value problem (1.10) can be written as a boundary integral (Shi, Ramesh & Mukherjee (1995)):

$$\phi(\mathbf{q}_\star) = \int_{\Gamma^\star} G^\star(\mathbf{q}_\star, \mathbf{r}_\star)\sigma^\star(\mathbf{r}_\star)\mathrm{d}\Gamma^\star + c_{\mathrm{T}}, \tag{1.11}$$

where $\Gamma^\star = \Gamma_1^\star \cup \Gamma_2^\star$ is the overall surface of the conductors, $\mathbf{q}_\star$ and $\mathbf{r}_\star$ are the observation and the source points on $\Gamma^\star$, $\sigma^\star$ is the surface charge density and $G^\star$ is the Green function. The constant c_{T} is determined from the potential at infinity. Eq. (1.11) gives the electrostatic potential in the present configuration of the system.

Let $\mathbf{n}^\star \mathrm{d}\Gamma^\star$ be an oriented surface element in the current configuration, with $\mathbf{n}^\star$ the outward unit normal. The area element $\mathrm{d}\Gamma^\star$ is expressed in terms of the corresponding area element $\mathrm{d}\Gamma$ by (see Gurtin (1981))

$$\mathrm{d}\Gamma^{\star\,2} = (\det \mathbf{F})^2(\mathbf{n} \cdot (\mathbf{F}^{\mathrm{T}}\mathbf{F})^{-1}\mathbf{n})\mathrm{d}\Gamma^2. \tag{1.12}$$

Therefore, Eq. (1.11) can be written in Lagrangian description as

$$\Phi(\mathbf{q}) = \int_{\Gamma} G(\mathbf{q}, \mathbf{r})\sigma(\mathbf{r})(\det \mathbf{F})\sqrt{\mathbf{n} \cdot (\mathbf{F}^{\mathrm{T}}\mathbf{F})^{-1}\mathbf{n}}\,\mathrm{d}\Gamma + C_{\mathrm{T}} \tag{1.13}$$

where $\sigma(\mathbf{r}) = \sigma^\star(\mathbf{r}_\star(\mathbf{r}))$, and $G(\mathbf{q}, \mathbf{r}) = G^\star(\mathbf{q}_\star(\mathbf{q}), \mathbf{r}_\star(\mathbf{r}))$.

The electrostatic potential energy stored in $\bar{\Omega}$ for the two-conductor system is given by

$$U_{\mathrm{e}} = \frac{\epsilon}{2}\int_{\bar{\Omega}} \mathrm{grad}\phi \cdot \mathrm{grad}\phi \mathrm{d}\bar{\Omega}, \tag{1.14}$$

where grad is the gradient operator with respect to the present coordinates, and ϵ is the dielectric constant of the medium comprising $\bar{\Omega}$. The electrostatic traction at the observation point $\mathbf{q}_\star$ in the present configuration is given by

$$[f_{\mathrm{e}}^\star \mathbf{n}^\star](\mathbf{q}_\star) = -\frac{\epsilon}{2}[(\mathrm{grad}\phi \cdot \mathrm{grad}\phi)\mathbf{n}^\star](\mathbf{q}_\star). \tag{1.15}$$

Using the relation

$$\mathrm{Grad}\Phi = \mathbf{F}^{\mathrm{T}}\mathrm{grad}\phi, \tag{1.16}$$

imposing the condition (1.5), and substituting in it from Eqs. (1.15) and (1.12) we obtain the electrostatic traction $\bar{\mathbf{t}}$ at the observation point $\mathbf{q}$ in the reference configuration:

$$\bar{\mathbf{t}}(\mathbf{q}) = -\frac{\epsilon}{2}\left[(\det\mathbf{F})\left(\mathrm{Grad}\Phi\cdot\left(\mathbf{F}^{\mathrm{T}}\mathbf{F}\right)^{-1}\mathrm{Grad}\Phi\right)\mathbf{F}^{-\mathrm{T}}\mathbf{n}\right](\mathbf{q}). \tag{1.17}$$

Thus the solution of the 3-D problem for MEMS requires solving the initial-boundary-value problems defined by Eqs. (1.1)-(1.4) and (1.10) with the surface traction per unit undeformed area given by Eq. (1.17). If the surface charge distribution σ in the reference configuration is considered as the unknown instead of the electrostatic potential ϕ, the solution of the boundary value problem in terms of σ is given by Eq. (1.13). In this case σ will appear in the expression (1.17) for $\bar{\mathbf{t}}$.

Note that the initial-boundary-value problem (1.1)-(1.4) is defined on the known region Ω_1 but the boundary-value problem (1.10) is defined in $\bar{\Omega}$ which is exterior to $\Omega_1^\star \cup \Omega_2^\star$. Assuming that the body 2 is rigid as is often the case in MEMS, then $\Omega_2^\star = \Omega_2$. The electrical and the mechanical problems are strongly coupled since $\Omega_1^\star$ is unknown a priori, and the boundary-value problem (1.10) requires that $\Omega_1^\star$ be known. A possibility is to use an iterative technique to solve the coupled electromechanical problem.

We also emphasize that the mechanical deformations of the material occupying the region $\bar{\Omega}$ have been neglected. However, when $\bar{\Omega}$ is occupied by a fluid then deformations of this fluid should also be considered. This requires reformulation of the above problem.

When the MEMS undergoes small deformations and the effect of body force is negligible, then the problem reduces to solving the following coupled set of equations:

$$\begin{aligned}
\varrho_0\ddot{\mathbf{u}} &= \mathrm{Div}\left[\hat{\lambda}\left(\mathrm{tr}\tilde{\mathbf{E}}\right)\mathbf{1} + 2\hat{\mu}\tilde{\mathbf{E}}\right] \quad \text{in } \Omega, && \text{(1.18a)}\\
\mathbf{u} &= \bar{\mathbf{u}} \quad \text{on } \Gamma_{\mathbf{u}}, && \text{(1.18b)}\\
\bar{\mathbf{t}} &= f_{\mathrm{e}}\mathbf{n} = -\frac{\epsilon}{2}\left(\mathrm{Grad}\phi\cdot\mathrm{Grad}\phi\right)\mathbf{n} \quad \text{on } \Gamma_{\mathbf{n}}, && \text{(1.18c)}\\
\mathrm{Div}\left[\mathrm{Grad}\phi\right] &= 0 \quad \text{in } \bar{\Omega}, && \text{(1.18d)}\\
\phi &= \bar{\phi}_1 \quad \text{on } \Gamma_1, && \text{(1.18e)}\\
\phi &= \bar{\phi}_2 \quad \text{on } \Gamma_2, && \text{(1.18f)}\\
\phi &\to 0 \quad \text{as } |\mathbf{x}| \to \infty, && \text{(1.18g)}
\end{aligned}$$

and initial conditions (1.4). Here, $\tilde{\mathbf{E}} = \left[\mathrm{Grad}\mathbf{u} + (\mathrm{Grad}\mathbf{u})^{\mathrm{T}}\right]/2$ is the small deformation strain tensor. If the surface charge distribution σ is considered as the unknown for the electrostatic problem, the solution of the boundary-values problem defined by Eqs. (1.18d)-(1.18g) is given by

$$\phi(\mathbf{q}) = \int_\Gamma G(\mathbf{q},\mathbf{r})\sigma(\mathbf{r})\mathrm{d}\Gamma + c_{\mathrm{T}}. \tag{1.19}$$

Consequently, σ appears in Eq. (1.18c). For infinitesimal deformations, $\bar{\Omega}$ equals the exterior of the region $\Omega_1 \cup \Omega_2$ and is known. Thus the boundary-value problem (1.18d)-(1.18g) can be solved without analyzing the mechanical problem. Knowing ϕ, the initial-boundary-value problem defined by Eqs. (1.18a)-(1.18c) and (1.4) can be analyzed either analytically or numerically. Thus the electrical and the mechanical problems become uncoupled in a way similar to that in linear thermoelasticity. This uncoupling of the two problems is valid even for anisotropic MEMS.

The electrostatic pressure $f_{\rm e}$ can also be determined by first finding the capacitance of the two conductor system $\Omega_1 \cup \Omega_2$. When Ω_1 and Ω_2 are flat bodies and are parallel to each other, $f_{\rm e}$ is obtained by differentiating the energy stored in the capacitor with respect to the local distance g between Ω_1 and Ω_2. This approach is used in Sec. 1.4.3 to ascertain $f_{\rm e}$ for a MEM beam.

1.3 Electrostatically actuated micromembranes

In this Section we study pull-instability in micromembranes due to the Coulomb force. Recall that the membrane approximation is valid for $L/h \geq 400$ (see e.g. Mansfield (1989)), where L is a typical in-plane dimension and h is the membrane thickness. We also analyze the effect of the Casimir force on the pull-in parameters. We show that beyond a certain size, the pull-in instability occurs at zero voltage. This means that the system collapses during the manufacturing process. We also analyze symmetry breaking in annular membranes due to the combined effects of the Coulomb and the Casimir forces. Research efforts in this area may be found in Serry, Walliser & Maclay (1998),Lin & Zhao (2005), and Bárcenas, Reyes & Esquivel-Sirvent (2005). In Serry et al. (1998) the effect of the Casimir force is considered for 1-D membranes but that of the Coulomb force is discarded. In Lin & Zhao (2005) a reduced one degree-of-freedom model for analyzing the effect of both the Casimir and the Coulomb forces on beam-like bodies is presented, while Bárcenas et al. (2005) have studied the pull-in instability under the action of the Casimir force using a one degree-of-freedom model.

1.3.1 The Casimir effect

With the decrease in device dimensions from the micro to the nanoscale an additional force on nanoelectromechanical systems (NEMS), such as the Casimir force (Casimir (1948), also see e.g. Lamoreaux (2005), and Borgag, Mohideen & Mostepanenko (2001)), should be considered.

The Casimir force represents the attraction between two uncharged material bodies due to

modification of the zero-point energy associated with the electromagnetic modes in the space between them. An important feature of the Casimir effect is that even though its nature is quantistic, it predicts a force between macroscopic bodies.

Consider a hollow box with perfectly conducting uncharged walls of length g. Maxwell's equations for vanishing sources lead to the following wave equation for the electric field $\mathbf{E}$ inside the box:

$$\triangle \mathbf{E}(\mathbf{x}, t) = \frac{\partial^2 \mathbf{E}}{\partial t^2}(\mathbf{x}, t). \tag{1.20}$$

Boundary conditions are that components of the electric field parallel to the walls are zero at the walls. That is

$$\mathbf{E} - (\mathbf{E} \cdot \mathbf{n})\, \mathbf{n} = \mathbf{0} \quad \text{on the walls.} \tag{1.21}$$

The eigenvalue problem defined by Eqs. (1.20) and (1.21) can be solved without using initial conditions, and by separating the variables as

$$\mathbf{E}(\mathbf{x}, t) = \mathbf{\Xi}(\mathbf{x})\tau(t). \tag{1.22}$$

The spatial part of the solution is given by

$$\Xi^1(\mathbf{x}) = \cos\left(k_1 x^1\right) \sin\left(k_2 x^2\right) \sin\left(k_3 x^3\right), \tag{1.23a}$$

$$\Xi^2(\mathbf{x}) = \sin\left(k_1 x^1\right) \cos\left(k_2 x^2\right) \sin\left(k_3 x^3\right), \tag{1.23b}$$

$$\Xi^3(\mathbf{x}) = \sin\left(k_1 x^1\right) \sin\left(k_2 x^2\right) \cos\left(k_3 x^3\right), \tag{1.23c}$$

where $\mathbf{k} = (k_1, k_2, k_3)$ is the wave vector. Imposing boundary conditions (1.21) at the walls leads to the following relation

$$k_i = \frac{\pi \nu_i}{g}, \tag{1.24}$$

with ν_i being an integer.

Eqs. (1.22) and (1.23) imply that the time dependent part of the solution satisfies the harmonic oscillator equation

$$\frac{\partial^2 \tau}{\partial t^2} + \omega_{\mathbf{k}}^2 \tau = 0, \tag{1.25}$$

where $\omega_{\mathbf{k}} = c|\mathbf{k}|$ is the angular frequency of the normal modes, and c is the speed of light.

In quantum mechanics, each mode is treated as a quantum harmonic oscillator with associated energies (see e.g. Borgag et al. (2001))

$$\mathcal{E}_n^{\mathbf{k}} = \hbar \omega_{\mathbf{k}} \left(\frac{1}{2} + n \right), \tag{1.26}$$

where the integer n represents the number of photons in the mode and $\hbar$ is the Plank constant. The energy corresponding to $n = 0$ (vacuum) is the zero point energy

$$\mathcal{E}_0^{\mathbf{k}} = \frac{1}{2} \hbar \omega_{\mathbf{k}}. \tag{1.27}$$

The sum over all modes gives the zero point energy inside the box as

$$\mathcal{E}_0 = 2 \sum_{k_1,k_2,k_3} \mathcal{E}_0^{\mathbf{k}} = \sum_{k_1,k_2,k_3} \hbar c \sqrt{(k_1^2 + k_2^2 + k_3^2)}, \tag{1.28}$$

where the factor 2 is due to the two possible polarizations for $\mathbf{k}$ (see Lamoreaux (2005)). Since there are an infinite number of normal modes with increasingly high frequencies, the energy $\mathcal{E}_0$ is infinite.

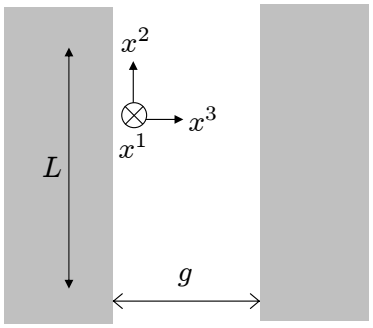

Figure 1.5: Coordinate system for calculating the Casimir force.

Consider the capacitor with perfectly conducting plates of area L^2 at a distance g in vacuum (Fig. 1.5). If $L \gg g$, the sum over k_1 and k_2 in Eq. (1.28) is replaced by an integral, $\sum_{k_i} \to (L/\pi) \int_0^\infty \mathrm{d}k_i$, $i = 1, 2$ (see Lamoreaux (2005)). If g is made arbitrarily large, then the sum over k_3 can be replaced by the corresponding integral.

The Casimir force is determined by the change in the zero point energy between the state corresponding to the two plates at a finite distance g, and the state corresponding to $g \to \infty$. This determines the potential energy

$$\begin{aligned} \mathcal{U}(g) &= \mathcal{E}_0(g) - \mathcal{E}_0(\infty) \\ &= \hbar c \frac{L^2}{\pi^2} \int_0^\infty \int_0^\infty \left(\sum_{\nu_3} \sqrt{k_1^2 + k_2^2 + \frac{\nu_3^2 \pi^2}{g^2}} - \frac{g}{\pi} \int_0^\infty \sqrt{k_1^2 + k_2^2 + k_3^2}\, \mathrm{d}k_3 \right) \mathrm{d}k_1 \mathrm{d}k_2 \end{aligned} \tag{1.29}$$

The resulting Casimir pressure is given by

$$f_\mathrm{c}(g) = -\frac{1}{L^2} \nabla \mathcal{U}(g) = -\frac{\pi^2 \hbar c}{240 g^4} \tag{1.30}$$

The detailed calculation is done in Lamoreaux (2005) employing the Euler-Maclaurin summation formula (see Whittaker & Watson (1963)). In order to truncate the infinite summation and integration at a certain wave vector $\mathbf{k}_\mathrm{max}$, a cutoff function is introduced.

The existence of the Casimir force poses a severe constraint on the miniaturization of electrostatically actuated devices. At the nanoscale, the Casimir force may overcome elastic restoring actions in the device and lead to the plates' sticking together during the fabrication process.

An important characteristic of the Casimir force is its strong dependence on the shape, and switching from attractive to repulsive depending on the geometry. In Boyer (1968), the zero point energy of a conducting spherical shell has been computed. While parallel plates are attracted to each other because of the zero point energy, a conducting sphere tends to expand.

Typical experimental measurements of Casimir forces involve gold (Au)-coated surfaces that are modeled by a Drude-type dielectric function (see e.g. Lamoreaux (1997), Sukenik, Boshier, Cho, Sandoghdar & Hinds (1993), and Harris, Chen & Mohideen (2000)).

1.3.2 Mathematical model of a microelectromechanical system

Some of the material in this and the following subsections is taken from Batra, Porfiri & Spinello (2006*a*).

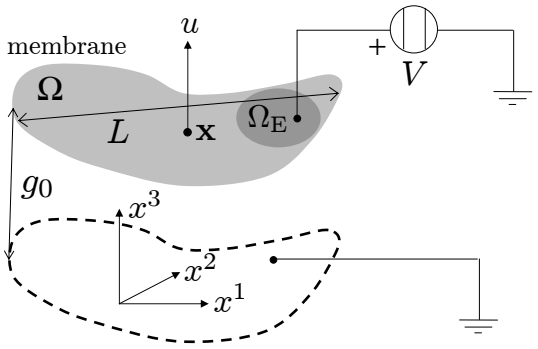

Figure 1.6: Geometry of the microelectromechanical system.

A schematic sketch of the problem studied is shown in Fig. 1.6. We assume that (i) both plates are perfect conductors, and are separated by a dielectric layer of permittivity ϵ, (ii) the bottom plate is rigid, and the top one is deformable, and can be modeled as an elastic membrane, (iii) the membrane is either clamped or free on the boundary, (iv) the membrane undergoes static infinitesimal deformations, (v) a potential difference V exists between the two plates, (vi) electric fringing fields are negligible (see e.g. Pelesko & Bernstein (2002)), (vii) the uniform initial gap, g_0, between the two plates is much smaller than a typical linear dimension of the membrane, (viii) electric flux lines between the conductors are uniformly

distributed over the surface area of the membrane or the plate, and (ix) the effect of the change in the direction of the Casimir and the Coulomb forces as the membrane deforms is negligible. Under these assumptions the governing equation for the deflection u of the membrane becomes (Pelesko & Bernstein (2002)):

$$\sigma_0 h \triangle u\,(\mathbf{x}) + f_{\mathrm{e}}(u(\mathbf{x}), \mathbf{x}) + f_{\mathrm{c}}(u(\mathbf{x})) = 0, \quad \mathbf{x} \in \Omega. \tag{1.31}$$

Here, Ω is the membrane domain, $\mathbf{x}$ a generic point, and $\triangle$ the Laplacian operator. σ_0 is the tensile stress in the membrane, and h is the thickness. f_{e} is the electrostatic pressure on the bottom surface of the membrane, and f_{c} is the Casimir pressure (see Eq. (1.30)).

We nondimensionalize the vertical coordinate x^3 with respect to the initial gap g_0, and the in-plane coordinates x^1 and x^2 with respect to the characteristic length L (see Fig. 1.6). The governing equation (1.18d) for the potential ϕ becomes

$$\frac{g_0^2}{L^2}\left(\frac{\partial^2\phi}{(\partial\hat{x}^1)^2} + \frac{\partial^2\phi}{(\partial\hat{x}^2)^2}\right) + \frac{\partial^2\phi}{(\partial\hat{x}^3)^2} = 0, \tag{1.32}$$

where a superimposed hat refers to nondimensional coordinates. By virtue of assumption (vii) Eq. (1.32) reduces to

$$\frac{\partial^2\phi}{(\partial\hat{x}^3)^2} = 0. \tag{1.33}$$

Because of assumption (viii) the potential ϕ is a function of $\hat{x}^3$ only. Imposing the boundary conditions $\phi(0) = 0$, and $\phi(g_0 + u) = V\delta\,(\mathbf{x})$ on the bottom and the top plates respectively and omitting the superimposed hat, the solution is

$$\phi = \frac{V}{g_0}\frac{\delta(\mathbf{x})}{(1 + u/g_0)}x^3, \tag{1.34}$$

where

$$\delta\,(\mathbf{x}) = \begin{cases} 1, & \mathbf{x} \in \Omega_{\mathrm{E}} \\ 0, & \mathbf{x} \notin \Omega_{\mathrm{E}} \end{cases}, \tag{1.35}$$

and Ω_{E} is the part of the membrane that is electroded and where the electric potential is effective. Substitution of Eq. (1.34) into Eq. (1.18c) gives the electrostatic pressure in the form

$$f_{\mathrm{e}}(u(\mathbf{x}), \mathbf{x}) = -\frac{\epsilon V^2}{2g_0^2}\frac{\delta(\mathbf{x})}{(1 + u(\mathbf{x})/g_0)^2}, \tag{1.36}$$

where terms depending on the spatial derivatives of u have been discarded consistently with assumption (ix).

The reduction of the right-hand side of Eq. (1.1a) to the left-hand side of Eq. (1.31) for small deflections u of a membrane is given, e.g., in Antman (2004).

We nondimensionalize the deflection by the initial gap g_0, and obtain

$$\triangle u\left(\mathbf{x}\right)=\lambda\frac{\delta\left(\mathbf{x}\right)}{\left(1+u\left(\mathbf{x}\right)\right)^{2}}+\frac{\mu}{\left(1+u\left(\mathbf{x}\right)\right)^{4}}, \tag{1.37}$$

where we have used the same symbols to indicate nondimensional quantities as were used earlier for the dimensional ones. Parameters λ and μ are defined by

$$\lambda=\frac{\epsilon_0 V^2 L^2}{2\sigma_0 h g_0^3}, \qquad \mu=\frac{\pi^2\hbar c L^2}{240\sigma_0 h g_0^5}. \tag{1.38}$$

As the voltage V increases, the parameter λ increases while μ stays constant. Scaling down the device dimensions (h, g_0 and L) by a factor F

$$h\rightarrow h/F, \quad g_0\rightarrow g_0/F, \quad L\rightarrow L/F \tag{1.39}$$

increases λ by a factor of F^2 and μ by a factor of F^4, that is

$$\lambda\rightarrow F^2\lambda, \quad \mu\rightarrow F^4\mu. \tag{1.40}$$

Thus, for $F>1$, μ increases much faster than λ with a decrease in the device dimensions.

The boundary of the domain Ω is partitioned into two disjoint parts:

$$\partial\Omega=\Gamma_u\cup\Gamma_{\mathbf{n}}, \qquad \mathring{\Gamma}_u\cap\mathring{\Gamma}_{\mathbf{n}}=\varnothing, \tag{1.41}$$

where $\mathring{\Gamma}_u$ is comprised of the interior points of Γ_u. On Γ_u essential homogeneous boundary conditions are prescribed, that is

$$u\left(\mathbf{x}\right)=0, \qquad \mathbf{x}\in\Gamma_u, \tag{1.42}$$

while on $\Gamma_{\mathbf{n}}$ natural homogeneous boundary conditions are imposed, that is

$$\nabla u\left(\mathbf{x}\right)\cdot\mathbf{n}\left(\mathbf{x}\right)=0, \qquad \mathbf{x}\in\Gamma_{\mathbf{n}}. \tag{1.43}$$

1.3.3 Local weak formulation of the problem

We rewrite the nonlinear Poisson Eq. (1.37) as

$$\triangle u\left(\mathbf{x}\right)=G\left(\lambda,\mu,u,\mathbf{x}\right) \tag{1.44}$$

where

$$G\left(\lambda,\mu,u,\mathbf{x}\right)=\lambda\frac{\delta\left(\mathbf{x}\right)}{\left(1+u\right)^{2}}+\frac{\mu}{\left(1+u\right)^{4}}. \tag{1.45}$$

We partition the boundary Γ_u into n_{L} connected parts, say $\Gamma_u^{(1)},\ldots,\Gamma_u^{(n_{\mathrm{L}})}$. In order to enforce the essential boundary conditions we introduce n_{L} Lagrange multipliers $\gamma^{(1)},\ldots,\gamma^{(n_{\mathrm{L}})}$, each of them being defined on the corresponding part of Γ_u.

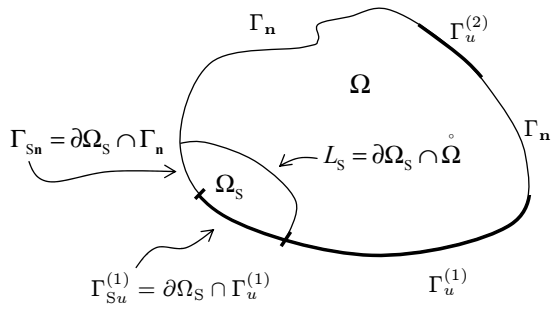

Figure 1.7: Subdomain of the global domain.

We introduce a local symmetric augmented weak formulation (LSAWF) of the boundary-value problem defined by Eqs. (1.44), (1.42) and (1.43) on a subdomain Ω_{S} of the domain Ω:

$$
\begin{aligned}
-\int_{\Omega_{\mathrm{S}}} \nabla u \cdot \nabla \tilde{u}\, \mathrm{d}\Omega \;\; - \;\; & \int_{\Omega_{\mathrm{S}}} G\left(\lambda, \mu, u, \mathbf{x}\right)\, \tilde{u}\, \mathrm{d}\Omega + \int_{L_{\mathrm{S}}} \nabla u \cdot \mathbf{n}\, \tilde{u}\, \mathrm{d}\Gamma \\
+ \;\; & \sum_{\alpha=1}^{n_{\mathrm{L}}} \left(\int_{\Gamma_{\mathrm{S}u}^{(\alpha)}} u\, \tilde{\gamma}^{(\alpha)} \mathrm{d}\Gamma + \int_{\Gamma_{\mathrm{S}u}^{(\alpha)}} \tilde{u}\, \gamma^{(\alpha)} \mathrm{d}\Gamma \right) = 0. \qquad (1.46)
\end{aligned}
$$

Here, as illustrated in Fig. 1.7, $\Gamma_{\mathrm{S}u}^{(\alpha)}$ is the intersection of $\partial\Omega_{\mathrm{S}}$ with $\Gamma_u^{(\alpha)}$, L_{S} is the part of $\partial\Omega_{\mathrm{S}}$ enclosed in the domain Ω, $\tilde{u}$ and $\tilde{\gamma}^{(\alpha)}$ are smooth test functions defined, respectively, in Ω_{S} and $\Gamma_{\mathrm{S}u}^{(\alpha)}$. The homogeneous natural boundary conditions (1.43) have been embedded in the weak formulation of the problem.

In the MLPG method test functions and trial solutions are chosen from different spaces, and the test functions need not vanish where essential boundary conditions are specified. In order to simplify the algebraic work, we select test functions $\tilde{u}$ which vanish on the inner boundary L_{S}; therefore the LSAWF (1.46) reduces to

$$
\begin{aligned}
-\int_{\Omega_{\mathrm{S}}} \nabla u \cdot \nabla \tilde{u}\, \mathrm{d}\Omega \;\; - \;\; & \int_{\Omega_{\mathrm{S}}} G(\lambda, \mu, u, \mathbf{x})\, \tilde{u}\, \mathrm{d}\Omega \\
+ \;\; & \sum_{\alpha=1}^{n_{\mathrm{L}}} \left(\int_{\Gamma_{\mathrm{S}u}^{(\alpha)}} u\, \tilde{\gamma}^{(\alpha)} \mathrm{d}\Gamma + \int_{\Gamma_{\mathrm{S}u}^{(\alpha)}} \tilde{u}\, \gamma^{(\alpha)} \mathrm{d}\Gamma \right) = 0. \qquad (1.47)
\end{aligned}
$$

Subdomains Ω_{S} are taken to be circles in order to facilitate the evaluation of integrals.

1.3.4 Discrete nonlinear formulation

In order to seek an approximate solution of the nonlinear problem, we use 2-D MLS basis functions† (see Appendix A.1) to express the trial solution in terms of nodal unknowns, $\hat{u}_1, ..., \hat{u}_N$. Note that the MLS basis functions do not have the Kronecker delta property. Therefore nodal unknowns, $\hat{u}_1, ..., \hat{u}_N$, do not equal values of the trial solution at the nodes. The Lagrange multiplier field $\gamma^{(\alpha)}$ is approximated by 1-D MLS basis functions constructed from nodes lying only on the curve $\Gamma_u^{(\alpha)}$. Therefore

$$\left(\gamma^{(\alpha)}\right)^h = \sum_{\beta=1}^{\nu^{(\alpha)}} \hat{\gamma}_\beta^{(\alpha)} \chi_\beta^{(\alpha)}, \tag{1.48}$$

where $\nu^{(\alpha)}$ is the number of nodes belonging to $\Gamma_u^{(\alpha)}$, $\chi_\beta^{(\alpha)}$'s are 1-D MLS basis functions, and $\hat{\gamma}_\beta^{(\alpha)}$'s are fictitious nodal values. We collect $\hat{\gamma}_\beta^{(\alpha)}$'s into n_{L} distinct vectors $\hat{\boldsymbol{\gamma}}^{(1)}, \ldots, \hat{\boldsymbol{\gamma}}^{(n_{\mathrm{L}})}$, and denote the total number of Lagrange multiplier nodes by $N_{\mathrm{L}} := \sum_{\alpha=1}^{n_{\mathrm{L}}} \nu^{(\alpha)}$.

In order to derive $N + N_{\mathrm{L}}$ equations for nodal unknowns $\hat{\mathbf{u}}$ and $\hat{\boldsymbol{\gamma}}^{(1)}, \ldots, \hat{\boldsymbol{\gamma}}^{(n_{\mathrm{L}})}$, we consider in Eq. (1.47) N subdomains $\Omega_{\mathrm{S}1}, \ldots, \Omega_{\mathrm{S}N}$, and $N + N_{\mathrm{L}}$ independent test functions:

$$\tilde{u}_1, \ldots, \tilde{u}_N, \qquad \tilde{\gamma}_1^{(\alpha)}, \ldots, \tilde{\gamma}_{\nu^{(\alpha)}}^{(\alpha)}, \quad \alpha = 1, \ldots, n_{\mathrm{L}}. \tag{1.49}$$

The discrete nonlinear equations obtained from Eq. (1.47) are

$$\mathbf{K}\,\hat{\mathbf{u}} + \mathbf{G}\left(\lambda, \mu, \hat{\mathbf{u}}\right) + \sum_{\alpha=1}^{n_{\mathrm{L}}} \mathbf{R}^{(\alpha)} \hat{\boldsymbol{\gamma}}^{(\alpha)} = \mathbf{0}, \tag{1.50}$$

$$\mathbf{V}^{(\alpha)}\,\hat{\mathbf{u}} = \mathbf{0}, \qquad \alpha = 1, \ldots, n_{\mathrm{L}}, \tag{1.51}$$

where

$$[\mathbf{K}]_{ij} = -\int_{\Omega_{\mathrm{S}}^i} \nabla\varphi_j \cdot \nabla\tilde{u}_i \,\mathrm{d}\Omega, \qquad i, j = 1, \ldots, N; \tag{1.52a}$$

$$\left[\mathbf{G}\left(\lambda, \mu, \hat{\mathbf{u}}\right)\right]_i = -\int_{\Omega_{\mathrm{S}}^i} G\left(\lambda, \mu, u^h\right)\, \tilde{u}_i \,\mathrm{d}\Omega, \qquad i = 1, \ldots, N; \tag{1.52b}$$

$$\left[\mathbf{R}^{(\alpha)}\right]_{i\beta} = \int_{\Gamma_{\mathrm{S}u}^{i\,(\alpha)}} \chi_\beta^{(\alpha)}\, \tilde{u}_i \mathrm{d}\Gamma, \qquad i = 1, \ldots, N, \quad \beta = 1, \ldots, \nu^{(\alpha)}; \tag{1.52c}$$

$$\left[\mathbf{V}^{(\alpha)}\right]_{\beta j} = \int_{\Gamma_{\mathrm{S}u}^{\beta\,(\alpha)}} \varphi_j\, \tilde{\gamma}_\beta^{(\alpha)} \mathrm{d}\Gamma, \qquad \beta = 1, \ldots, \nu^{(\alpha)}, \quad j = 1, \ldots, N. \tag{1.52d}$$

For subdomains having the shape of a sector of a circle, integrals in Eqs. (1.52) can be computed by the Gauss quadrature rule.

†The boundary $\partial\Omega$ of the 2-D domain Ω is approximated by piecewise straight lines connecting adjacent nodes on it.

In the MLPG1 method the test function $\tilde{u}_i$ for the i-th node is chosen to be the weight function W_i used in the MLS approximation, but of a different support. That is,

$$\tilde{u}_i(\mathbf{x}) = W_i(\eta_i \mathbf{x}), \tag{1.53}$$

where η_i is a positive number representing the ratio of the supports of the test, and the weight functions for the i-th node. Test functions for a Lagrange multiplier are chosen to be the test functions $\tilde{u}_i$'s restricted to the boundary $\Gamma_{Su}^{(\alpha)}$ of the domain.

Let rows of the $(N - N_L) \times N$ matrix $\mathbf{Y}$ be comprised of $(N - N_L)$ linearly independent null vectors of the $N_L \times N$ matrix $\mathbf{V}$ obtained by appending rows of matrices $\mathbf{V}^{(\alpha)}$'s, and set

$$\hat{\mathbf{u}} = \mathbf{Y}^T \mathbf{u}. \tag{1.54}$$

Substituting for $\hat{\mathbf{u}}$ from Eq. (1.54) into Eq. (1.51) gives

$$\mathbf{V}^{(\alpha)} \mathbf{Y}^T \mathbf{u} = 0, \qquad \alpha = 1, \ldots, n_L, \tag{1.55}$$

which are identically satisfied for every $(N - N_L)$-vector $\mathbf{u}$. Similarly, let rows of the $(N - N_L) \times N$ matrix $\mathbf{X}$ equal $(N - N_L)$ linearly independent null vectors of the $N_L \times N$ matrix $\mathbf{R}^T$ obtained by appending columns of matrices $\mathbf{R}^{(\alpha)}$'s, and transposing the entire matrix. Then

$$\mathbf{X}\mathbf{R}^{(\alpha)} = \mathbf{0}, \qquad \alpha = 1, ..., n_L. \tag{1.56}$$

Premultiplying both sides of Eq. (1.50) by $\mathbf{X}$ and substituting for $\hat{\mathbf{u}}$ from Eq. (1.54) we obtain the following reduced system of $(N - N_L)$ nonlinear equations for $\mathbf{u}$:

$$\bar{\mathbf{K}}\,\mathbf{u} + \bar{\mathbf{G}}(\lambda, \mu, \mathbf{u}) = \mathbf{0}, \tag{1.57}$$

where

$$\bar{\mathbf{K}} = \mathbf{X}\mathbf{K}\mathbf{Y}^T, \qquad \bar{\mathbf{G}}(\lambda, \mu, \mathbf{u}) = \mathbf{X}\,\mathbf{G}\left(\lambda, \mu, \mathbf{Y}^T\mathbf{u}\right). \tag{1.58}$$

Having found $\mathbf{u}$ from Eq. (1.57), $\hat{\mathbf{u}}$ is computed from Eq. (1.54).

1.3.5 Pseudoarclength continuation method

The system of nonlinear Eqs. (1.57) may not admit a unique solution $\mathbf{u}$ for an arbitrary value of the parameter λ and a given value of μ. We use the pseudoarclength continuation method (see e.g. Doedel et al. (1991*a*), Doedel et al. (1991*b*)) to solve Eqs. (1.57). It enables one to find the complete bifurcation path and the symmetry breaking bifurcation. The method is explained for the case of variable λ and fixed μ. When studying the behavior of the system under the effect of the Casimir force only, i.e., for $\lambda = 0$ with varying μ, exactly the same procedure applies except that the role of the two parameters is exchanged.

A new parameter s is added so that λ and $\mathbf{u}$ are considered functions of s. If the solution $(\mathbf{u}_{k-1}, \lambda_{k-1})$ of Eqs. (1.57) is known at $s = s_{k-1}$, the solution

$$(\mathbf{u}_k, \lambda_k) = (\mathbf{u}_{k-1} + \Delta\mathbf{u}_k, \lambda_{k-1} + \Delta\lambda_k) \tag{1.59}$$

at the abscissa $s_k = s_{k-1} + \Delta s_k$ is found by solving the system of equations:

$$\bar{\mathbf{K}}\,\mathbf{u}_k + \bar{\mathbf{G}}\,(\lambda_k, \mu, \mathbf{u}_k) = \mathbf{0}, \tag{1.60a}$$

$$(\mathbf{u}_k - \mathbf{u}_{k-1})^{\mathrm{T}}\,\mathbf{U}\,\partial_s\mathbf{u}_{k-1} + (\lambda_k - \lambda_{k-1})\,\partial_s\lambda_{k-1} - \Delta s_k = 0, \tag{1.60b}$$

where $\mathbf{U}$ is a symmetric positive definite matrix, and ∂_s indicates derivative with respect to s. In many cases (see e.g. Doedel et al. (1991*a*)), $\mathbf{U}$ is chosen to be the identity matrix, but for the present problem, numerical experiments showed that more stable solutions are obtained by choosing

$$\mathbf{U} = \mathbf{\Phi}^{\mathrm{T}}\mathbf{\Phi}, \tag{1.61}$$

where $\mathbf{\Phi}$ is defined by Eq. (A.19) in Appendix A.1. This implies that the arc length is computed by using the actual nodal values, rather than the fictitious ones.

Geometrically interpreted, within this method we find a solution $(\mathbf{u}_k, \lambda_k)$ to the system (1.57) in an hyperplane that is at a distance Δs_k from $(\mathbf{u}_k, \lambda_k)$ and that is perpendicular to the direction vector $(\partial_s\mathbf{u}_{k-1}, \partial_s\lambda_{k-1})$ (see Doedel et al. (1991*a*)).

The solution of the set (1.60) of nonlinear equations, for the unknowns $\Delta\mathbf{u}_k$ and $\Delta\lambda_k$, is found by using Newton's iterations. Hence the generic ν-th iteration is

$$\begin{bmatrix} \bar{\mathbf{T}}_k^{(\nu)}\left(\lambda_k^{(\nu)}, \mathbf{u}_k^{(\nu)}\right) & \bar{\mathbf{H}}_k^{(\nu)}\left(\lambda_k^{(\nu)}, \mathbf{u}_k^{(\nu)}\right) \\ (\partial_s\mathbf{u}_{k-1})^{\mathrm{T}}\,\mathbf{U} & \partial_s\lambda_{k-1} \end{bmatrix} \begin{bmatrix} \Delta\mathbf{u}_k^{(\nu)} \\ \Delta\lambda_k^{(\nu)} \end{bmatrix} = \\ - \begin{bmatrix} \bar{\mathbf{K}}\,\mathbf{u}_k^{(\nu)} + \bar{\mathbf{G}}\left(\lambda_k^{(\nu)}, \mu, \mathbf{u}_k^{(\nu)}\right) \\ \left(\mathbf{u}_k^{(\nu)} - \mathbf{u}_{k-1}\right)^{\mathrm{T}}\,\mathbf{U}\,\partial_s\mathbf{u}_{k-1} + \left(\lambda_k^{(\nu)} - \lambda_{k-1}\right)\partial_s\lambda_{k-1} - \Delta s_k \end{bmatrix}, \tag{1.62}$$

where $\left(\Delta\mathbf{u}_k^{(\nu)}, \Delta\lambda_k^{(\nu)}\right)$ indicates the ν-th solution increment; $\left(\mathbf{u}_k^{(\nu)}, \lambda_k^{(\nu)}\right)$ is the updated solution at the $(\nu-1)$-th iteration, i.e.,

$$\mathbf{u}_k^{(\nu)} = \mathbf{u}_{k-1} + \sum_{h=1}^{\nu-1}\Delta\mathbf{u}_k^{(h)}, \qquad \lambda_k^{(\nu)} = \lambda_{k-1} + \sum_{h=1}^{\nu-1}\Delta\lambda_k^{(h)}; \tag{1.63}$$

$\bar{\mathbf{T}}_k^{(\nu)}\left(\lambda_k^{(\nu)}, \mathbf{u}_k^{(\nu)}\right)$ is the tangent stiffness at the $(\nu-1)$-th iteration, i.e.,

$$\bar{\mathbf{T}}_k^{(\nu)}\left(\lambda_k^{(\nu)}, \mathbf{u}_k^{(\nu)}\right) = \bar{\mathbf{K}} + \mathbf{X}\left[\mathbf{D}_k^{(\nu)}\left(\lambda_k^{(\nu)}, \mathbf{u}_k^{(\nu)}\right)\right]\mathbf{Y}^{\mathrm{T}}, \tag{1.64}$$

with

$$\left[\mathbf{D}_k^{(\nu)}\left(\lambda_k^{(\nu)}, \mathbf{u}_k^{(\nu)}\right)\right]_{ij} = -\int_{\Omega_{\mathrm{S}}^i}\frac{\partial G}{\partial u^h}\left(\lambda_k^{(\nu)}, \mu, \boldsymbol{\varphi}^{\mathrm{T}}\mathbf{Y}^{\mathrm{T}}\mathbf{u}_k^{(\nu)}\right)\tilde{u}_i\varphi_j\mathrm{d}\Omega, \tag{1.65}$$

and

$$\left[\bar{\mathbf{H}}_k^{(\nu)}\left(\lambda_k^{(\nu)},\mathbf{u}_k^{(\nu)}\right)\right]_i = -\int_{\Omega_{\mathrm{S}}^i}\frac{\partial G}{\partial\lambda}\left(\lambda_k^{(\nu)},\mu,\boldsymbol{\varphi}^{\mathrm{T}}\mathbf{Y}^{\mathrm{T}}\mathbf{u}_k^{(\nu)}\right)\tilde{u}_i\mathrm{d}\Omega. \tag{1.66}$$

Iterations are performed till

$$\max\left\{\sup_{\mathbf{x}\in\Omega}\left[\boldsymbol{\varphi}\left(\mathbf{x}\right)^{\mathrm{T}}\mathbf{Y}^{\mathrm{T}}\Delta\mathbf{u}_k^{(\nu)}\right],\Delta\lambda_k^{(\nu)}\right\}<\varepsilon_{\mathrm{T}}, \tag{1.67}$$

where ε_{T} is a prescribed tolerance.

Once the solution $(\mathbf{u}_k,\lambda_k)$ has been found, the direction vector $(\partial_s\mathbf{u}_k,\partial_s\lambda_k)$, needed for the subsequent iteration is determined by solving

$$\left[\begin{array}{cc}\bar{\mathbf{T}}_k^{(\bar{\nu}_k)}\left(\lambda_k,\mathbf{u}_k\right) & \bar{\mathbf{H}}_k^{(\bar{\nu}_k)}\left(\lambda_k,\mathbf{u}_k\right)\\ \left(\partial_s\mathbf{u}_{k-1}\right)^{\mathrm{T}}\mathbf{U} & \partial_s\lambda_{k-1}\end{array}\right]\left[\begin{array}{c}\partial_s\mathbf{u}_k\\ \partial_s\lambda_k\end{array}\right]=\left[\begin{array}{c}\mathbf{0}\\ 1\end{array}\right], \tag{1.68}$$

where $\bar{\nu}_k$ is the number of iterations required for the solution to converge. The direction vector is then rescaled according to

$$\left(\partial_s\mathbf{u}_k\right)^{\mathrm{T}}\mathbf{U}\,\partial_s\mathbf{u}_k+\left(\partial_s\lambda_k\right)^2=1. \tag{1.69}$$

The length Δs_{k+1} for the next step is determined from the knowledge of the length Δs_k and the iteration number $\bar{\nu}_k$ using the following simple adaptive scheme

$$\Delta s_{k+1}=\Delta s_k\sqrt{\frac{\tau}{\bar{\nu}_k}}, \tag{1.70}$$

where τ represents the desired number of iterations for the convergence of Newton's method. The parameter τ is chosen in such a way that if Newton's method converges rapidly the step size is increased, while if Newton's method converges slowly the step size is decreased (Doedel et al. (1991*a*)).

The pseudoarclength algorithm is started by assuming that for $s_0=0$ the solution is the pair $(\mathbf{u}_0,\lambda_0)=(\mathbf{0},0)$, and computing the solution $\mathbf{u}_1$ for a given small λ_1 with the standard Euler method resulting from linearizing Eq. (1.57) about $(\mathbf{u}_0,\lambda_0)$. Once the solution corresponding to this small electrostatic force is computed, the direction vector $(\partial_s\mathbf{u}_1,\partial_s\lambda_1)$ is estimated by the linear approximation

$$\partial_s\mathbf{u}_1=\frac{1}{\Delta s_1}\left(\mathbf{u}_1-\mathbf{u}_0\right),\qquad \partial_s\lambda_1=\frac{1}{\Delta s_1}\left(\lambda_1-\lambda_0\right), \tag{1.71}$$

where the initial arc length is

$$\Delta s_1=\sqrt{\left(\mathbf{u}_1\right)^{\mathrm{T}}\mathbf{U}\mathbf{u}_1+\left(\lambda_1\right)^2}. \tag{1.72}$$

When the tangent stiffness matrix, $\bar{\mathbf{T}}_k$ in Eq. (1.62), becomes singular the entire matrix on the left-hand side of Eq. (1.62) is generally nonsingular unless a bifurcation occurs (Doedel

et al. (1991*a*)). This means that the pull-in instability may be detected, and the MEMS behavior analyzed after reaching the instability.

When a bifurcation occurs the entire matrix on the left-hand side of Eq. (1.62) becomes singular, and crossing the bifurcation point implies a change in the sign of the determinant of this matrix. In this case, the bifurcation point is determined by using the secant method, and the bifurcation path is followed by using the normal vector to the original path as an initial estimate of the direction vector (Doedel et al. (1991*a*)).

1.3.6 Pull-in instability

Pull-in is detected by solving the nondimensional nonlinear Poisson Eq. (1.44) with $\mu = 0$. The pseudoarclength algorithm explained in Sec. 1.3.5 is employed.

We compare results for a rectangular, a circular, and an elliptic MEMS from the MLPG method with those obtained using either the shooting method or the finite-difference method. For the elliptic MEMS, we investigate the effect on the pull-in instability of the ratio of the major to the minor axes of the ellipse.

Parameters compared are $\lambda_{\rm PI}$ and $\|u_{\rm PI}\|_\infty$. $\lambda_{\rm PI}$ and $\|u_{\rm PI}\|_\infty$ indicate, respectively, the value of the parameter λ for which the pull-in instability occurs, and the corresponding infinity norm of the deflection field.

For a specific MEMS, the dimensional value of the pull-in voltage is obtained by substituting for $\lambda_{\rm PI}$ into Eq. (1.38), while the dimensional value of the membrane deflection at the pull-in instability is obtained by multiplying $\|u_{\rm PI}\|_\infty$ by the initial gap g_0.

The MLS approximation (see Appendix A.1) uses linear monomial basis as given in Eq. (A.4). The size r_i of the support of a weight function varies with the problem, and other constants defining weight functions are $k = 1$, $c_i = r_i/4$. The integration is performed by using 9 quadrature points for each line integral, and 9×9 quadrature points for each 2-D subdomain. The pseudoarclength continuation is started with $\lambda_1 = 0.1$, $\tau = 3$, and the tolerance $\varepsilon_{\rm T}$ is set equal to 10^{-6}. If the convergence is not achieved in 10 Newton's iterations the incremental arc length Δs is reduced by a factor of 2, and the algorithm is restarted from that point. In the neighborhood of the pull-in instability, more steps are needed to accurately estimate the pull-in parameters.

1.3.6.1 Rectangular MEMS

We consider a rectangular MEMS of unit length, width equal to 1/8, clamped on edges $x^1 = 0, 1$, and free on edges $x^2 = 0, 1/8$. We assume that the electrostatic pressure is

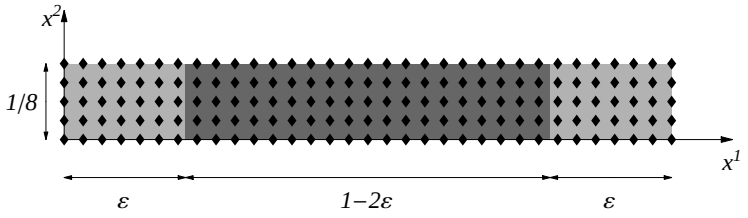

Figure 1.8: Geometry of the rectangular MEMS with the uniform grid of 33×5 nodes used to solve the 2-D boundary-value problem with the MLPG method. The electrostatic force is effective in the shaded region.

uniformly exerted only for $x^1 \in (\varepsilon, 1-\varepsilon)$ (see Fig. 1.8). That is, the central portion of length 2ε is electroded.

1.3.6.1.1 Reduction to a 1-D boundary-value problem Because of the boundary conditions and the load distribution, we assume that the solution is a function of x^1 only, and is symmetric with respect to the line $x^1 = 1/2$ (see Pelesko (2002)), yielding the following 1-D nonlinear boundary-value problem:

$$u_1''\left(x^1\right) = 0, \qquad x^1 \in (0, \varepsilon), \tag{1.73}$$

$$u_2''\left(x^1\right) = \frac{\lambda}{\left(1 + u_2\left(x^1\right)\right)^2}, \qquad x^1 \in (\varepsilon, 1/2), \tag{1.74}$$

$$u_1(0) = 0, \qquad u_2'(1/2) = 0, \tag{1.75}$$

$$u_1(\varepsilon) = u_2(\varepsilon), \qquad u_1'(\varepsilon) = u_2'(\varepsilon), \tag{1.76}$$

where a superimposed prime indicates derivative with respect to x^1.

The solution of the homogeneous Eq. (1.73) for $x^1 \in (0, \varepsilon)$ is

$$u_1\left(x^1\right) = c_1 x^1 + c_2, \qquad c_1, c_2 \in \mathbb{R}. \tag{1.77}$$

By imposing the first boundary condition (1.75), we obtain

$$c_2 = 0. \tag{1.78}$$

The interface conditions (1.76) give:

$$u_2(\varepsilon) = c_1 \varepsilon, \quad u_2'(\varepsilon) = c_1. \tag{1.79}$$

Hence the constant c_1 may be eliminated. The deflection field for $x^1 \in (\varepsilon, 1/2)$ is determined by solving the boundary-value problem

$$u_2''\left(x^1\right) = \frac{\lambda}{\left(1 + u_2\left(x^1\right)\right)^2}, \quad u_2(\varepsilon) = u_2'(\varepsilon)\,\varepsilon, \quad u_2'(1/2) = 0. \tag{1.80}$$

The constant c_1 is subsequently determined by either one of two conditions in Eq. (1.79).

1.3.6.1.2 Reduction of the boundary-value problem to an initial-value problem By generalizing the approach of Pelesko (2002) to partially electroded plates we transform the boundary-value problem (1.80) to the following initial-value problem

$$\frac{\mathrm{d}^2 w}{\mathrm{d}\eta^2} = \frac{1}{w^2}, \qquad \frac{\mathrm{d}w}{\mathrm{d}\eta}(0) = 0, \qquad w(0) = 1. \tag{1.81}$$

The above conversion is achieved by applying the change of variables:

$$\eta = b\left(\left(\frac{1}{2} - \varepsilon\right) - x^1\right), \tag{1.82a}$$

$$u^2\left(x^1\right) = aw(\eta) - 1, \tag{1.82b}$$

$$a = \frac{1}{w\left(b\left(\frac{1}{2} - \varepsilon\right)\right) + \varepsilon b w'\left(b\left(\frac{1}{2} - \varepsilon\right)\right)}, \tag{1.82c}$$

$$\lambda = \frac{b^2}{\left(w\left(b\left(\frac{1}{2} - \varepsilon\right)\right) + \varepsilon b w'\left(b\left(\frac{1}{2} - \varepsilon\right)\right)\right)^3}. \tag{1.82d}$$

We numerically solve the initial-value problem (1.81) with Mathematica using the built-in function NDSolve, obtain $w(\eta)$, and for every pair (w, b) we determine the corresponding pair $\left(u^2\left(x^1\right), \lambda\right)$, and the constant c_1. Once the deflection field is known on the entire strip we compute its infinity norm, which equals the mid-span deflection.

1.3.6.1.3 Numerical results and comparisons For the solution of the 2-D boundary-value problem defined by Eqs. (1.37), (1.42) and (1.43) with $\mu = 0$ by the MLPG method, we use a uniform grid of 33×5 nodes on the MEMS domain as shown in Fig. 1.8. The radius r_i of the support of each weight function (Eq. (A.23)) is set equal to 1/8. The subdomains of integration are determined by supports of test functions, and their radii are chosen equal to 1/32.

Fig. 1.9 exhibits the bifurcation diagram showing the infinity norm of the deflection versus the load parameter λ. We note that plots of $\|u\|_\infty$ vs. λ are qualitatively similar for all four values of ε, and the pull-in voltage decreases rapidly with a decrease of ε from 0.4 to 0. This is reasonable because the surface area on which the Coulomb force acts increases with a decrease in ε. For each value of ε the maximum deflection of the MEMS increases with an increase in λ and hence an increase in the applied voltage. This branch of the curve prior to the fold corresponds to stable equilibrium states, while the upper branch to unstable equilibrium states. If a given rectangular MEMS is pushed by forces other than the Coulomb force into a configuration corresponding to a point on the upper branch of the curves, equilibrium equation (1.37) and boundary conditions (1.42) and (1.43) are satisfied. The MEMS can theoretically stay in the unstable equilibrium configuration indefinitely if the external force is removed, the system is not perturbed, and the appropriate voltage is applied to the MEMS; see e.g. Serry et al. (1998).

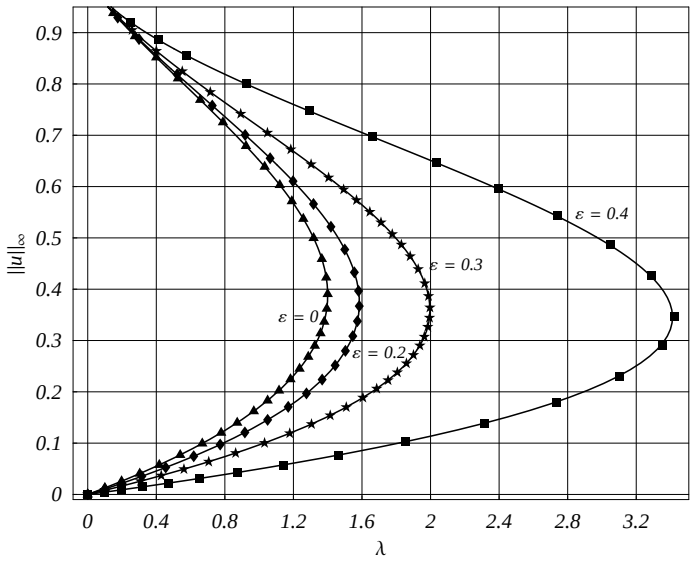

Figure 1.9: For different values of ε, comparison of the bifurcation diagrams obtained by solving the initial-value problem (solid line) and the MLPG method (polygons) for the rectangular MEMS.

For different values of the parameter ε, we compare in Table 1.1 the MLPG solution with that obtained by solving the initial-value problem (1.81); the latter is often referred to as the shooting method (Pelesko (2002)). It is clear that values of $\lambda_{\rm PI}$ predicted by the MLPG method are very close to those obtained from the shooting method; the maximum difference between the two for $\varepsilon = 0.4$ equals 0.3%. The maximum deviation between the two values of $\|u_{\rm PI}\|_\infty$ equals 1.28%, and occurs for $\varepsilon = 0.3$. The MLPG solution is independent of the x^2-coordinate, and validates the approximation that u is a function of x^1 only.

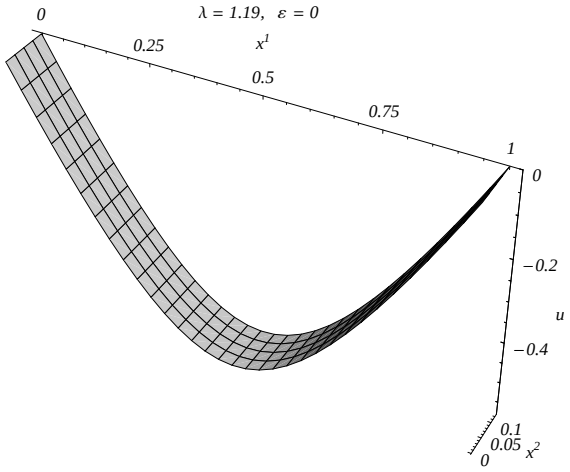

Figure 1.10: Deformed shape of the rectangular MEMS with $\varepsilon = 0$ and $\lambda = 1.19$.

For $\varepsilon = 0$ and $\lambda = 1.19$, Fig. 1.10 gives the deflected shape of the MEMS for a configura-

Table 1.1: For the rectangular MEMS, comparison of the MLPG results with those obtained with the shooting method.

	Shooting Metod		MLPG	
ε	λ_{PI}	$\|u_{\mathrm{PI}}\|_\infty$	λ_{PI}	$\|u_{\mathrm{PI}}\|_\infty$
0	1.400	0.3927	1.400	0.3885
0.2	1.584	0.3671	1.584	0.3671
0.3	1.996	0.3662	1.997	0.3615
0.4	3.412	0.3470	3.421	0.3475

tion beyond the pull-in instability. The maximum deflection of the MEMS exceeds $\|u_{\mathrm{PI}}\|_\infty$ because no constraint is imposed on the maximum deflection of a point. As stated above, deformed shapes of the membrane beyond the pull-in deflection correspond to unstable equilibrium states of the system.

1.3.6.2 Circular disk

We consider a disk of unit radius clamped along its periphery.

1.3.6.2.1 Reduction to a 1-D boundary-value problem Following Pelesko & Chen (2003) we assume that the solution is a function of the radial coordinate r only, and deformations of the disk are axisymmetric. Thus the problem defined by Eq. (1.37) reduces to the following 1-D nonlinear boundary-value problem:

$$u''(r) + \frac{1}{r}u'(r) = \frac{\lambda}{(1+u(r))^2}, \quad u(1) = 0, \quad u'(0) = 0, \tag{1.83}$$

where a superimposed prime indicates derivative with respect to r.

1.3.6.2.2 Reduction of the boundary-value problem to an initial-value problem We reduce the boundary-value problem (1.83) to the initial-value problem

$$\frac{\mathrm{d}^2 w}{\mathrm{d}\eta^2} + \frac{1}{\eta}\frac{\mathrm{d}w}{\mathrm{d}\eta} = \frac{1}{w^2}, \quad \frac{\mathrm{d}w}{\mathrm{d}\eta}(0) = 0, \quad w(0) = 1, \tag{1.84}$$

by applying the following change of variables:

$$\eta = br, \quad u(r) = aw(\eta) - 1, \quad a = \frac{1}{w(b)}, \quad \lambda = \frac{b^2}{w(b)^3}. \tag{1.85}$$

As for the rectangular MEMS, we numerically solve the initial-value problem (1.84) with Mathematica using the built-in function NDSolve, and for every pair (w, b) determine the corresponding pair $(u(r), \lambda)$. Once the deflection field is known on the entire disk we compute its infinity norm, which equals the deflection of the disk center.

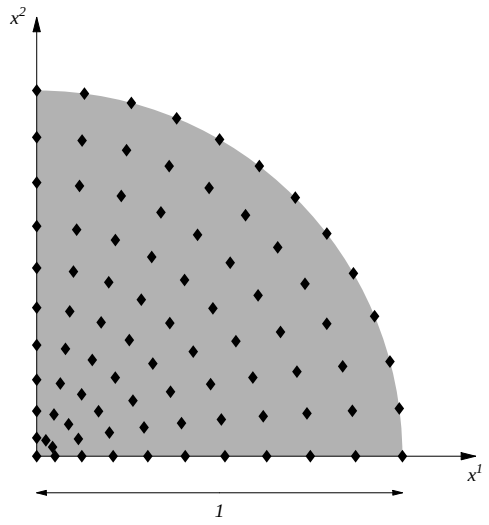

Figure 1.11: Grid of 86 nodes on the quarter of disk.

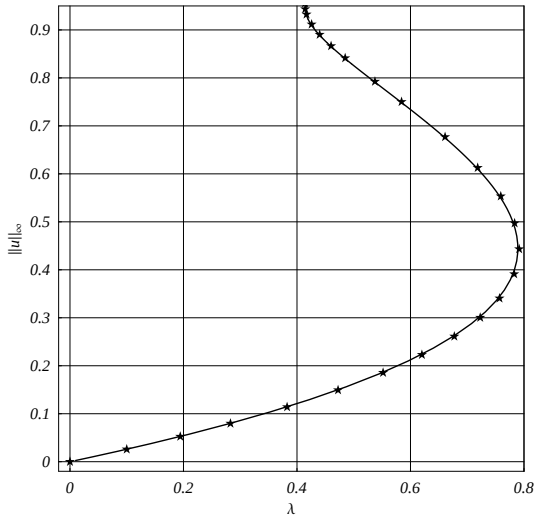

Figure 1.12: Comparison of the bifurcation diagrams obtained with the shooting method (solid line) and the MLPG method (polygons) for the circular MEMS.

1.3.6.2.3 Numerical results and comparisons Instead of considering the entire disk we analyze deformations of a quarter of the disk by using the grid of 86 nodes shown in Fig. 1.11. Here we do not assume that the deflection is independent of the angular position θ. On straight boundaries we impose homogeneous natural boundary conditions arising from the symmetry of the problem. The size r_i of the support of each weight function is taken to be 2/3. Subdomains of integration are determined by supports of test functions, and their radii are set equal to the distance between the chosen node and the one closest to it.

Fig. 1.12 shows the infinity norm of the deflection, which corresponds to the deflection of the disk center, versus the load parameter λ. Results from the MLPG method and those from the shooting method are compared in Table 1.2; the difference between the two values of $\lambda_{\rm PI}$, and of $\|u_{\rm PI}\|_\infty$ equals 0.32% and 1.6% respectively.

Table 1.2: For the circular MEMS, comparison of the MLPG results with those from the shooting method.

Shooting method		MLPG	
$\lambda_{\rm PI}$	$\|u_{\rm PI}\|_\infty$	$\lambda_{\rm PI}$	$\|u_{\rm PI}\|_\infty$
0.7890	0.4365	0.7915	0.4433

Fig. 1.13 depicts the deformed shape of a quarter of the disk for a voltage less than the pull-in voltage. The computed deflection is found to be independent of the circumferential coordinate, and supports the assumption made to find the solution with the shooting method.

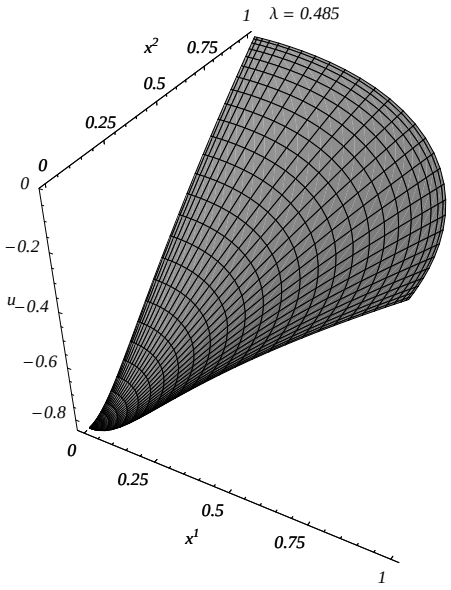

Figure 1.13: Deformed shape of a quarter of the circular MEMS for $\lambda = 0.485$.

By analyzing deformations of a quarter of the disk we may have missed solutions that do not exhibit the presumed symmetry.

1.3.6.3 Elliptic disk

We consider an ellipse of semi-major axis $a = 1$, semi-minor axis b, and clamped along its periphery. We analyze one quarter of the ellipse, impose homogeneous natural boundary

conditions on the straight edges, and investigate the effect of the aspect ratio b/a on the pull-in instability of the system.

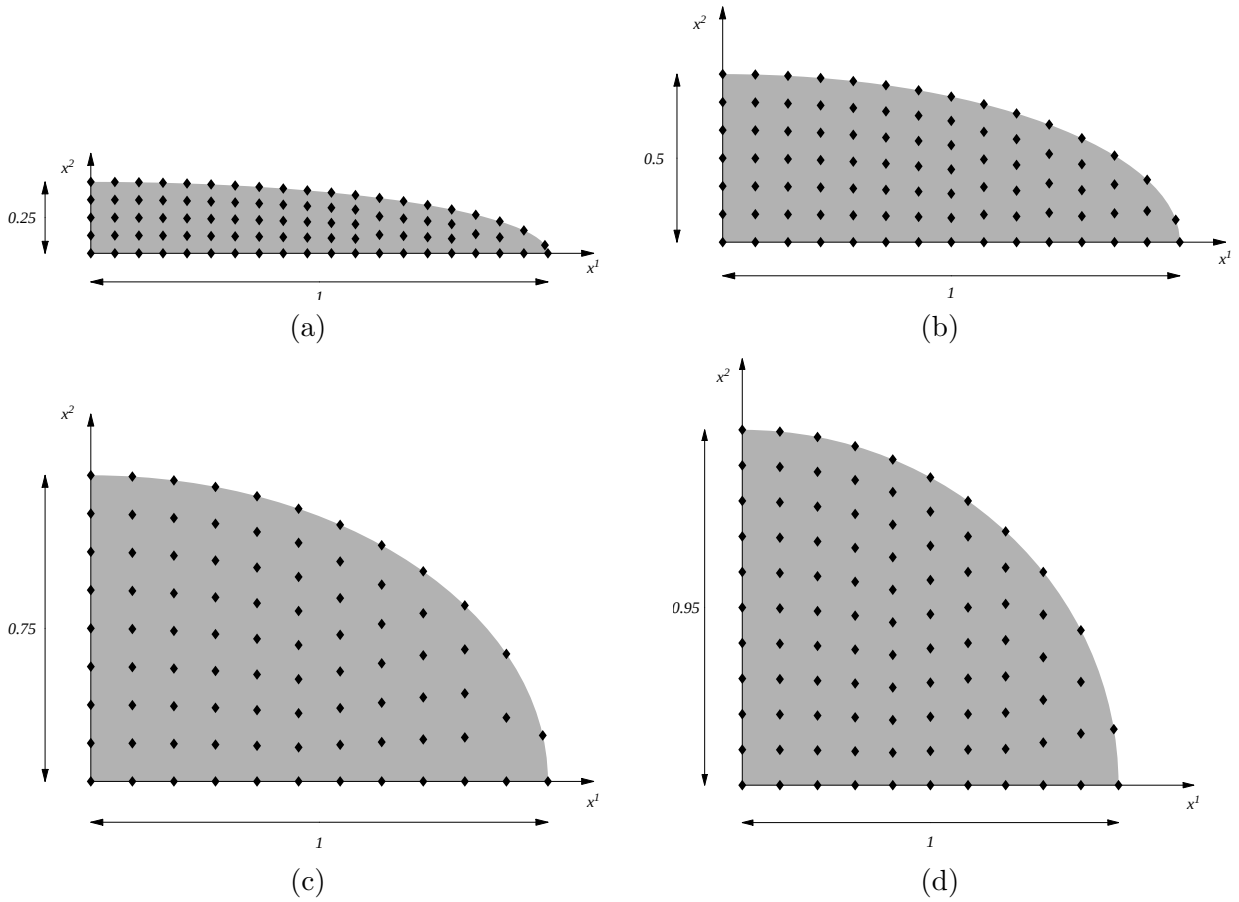

Figure 1.14: Locations of (a) 86 nodes, (b) 87 nodes, (c) 85 nodes, and (d) 94 nodes on the quarter of an elliptic disk with (a) $b/a = 0.25$, (b) $b/a = 0.5$, (c) $b/a = 0.75$, and (d) $b/a = 0.95$.

We study four aspect ratios, namely 0.25, 0.5, 0.75, and 0.95, and adopt, respectively, the grids of 86, 87, 85, and 94 nodes shown in Fig. 1.14(a)-(d). For a uniformly loaded elliptic membrane clamped on its edges, these nodal placements give an error of less than 0.7% in the maximum deflection with respect to the analytical solution

$$u^a\left(x^1, x^2\right) = \kappa\left(\left(\frac{x^1}{a}\right)^2 + \left(\frac{x^2}{b}\right)^2 - 1\right), \quad \kappa = \left(\frac{2}{a^2} + \frac{2}{b^2}\right)^{-1}. \tag{1.86}$$

Here, x^1 and x^2 are coordinates of a point with respect to rectangular Cartesian coordinate axes aligned with the major and the minor axes of the ellipse. Values of weight function parameters in the MLPG method are the same as those for the circular disk problem.

Fig. 1.15 shows pull-in bifurcation diagrams for the four elliptic MEMS. Due to an increase in the stiffness of the system with a decrease in the aspect ratio, the nondimensional pull-

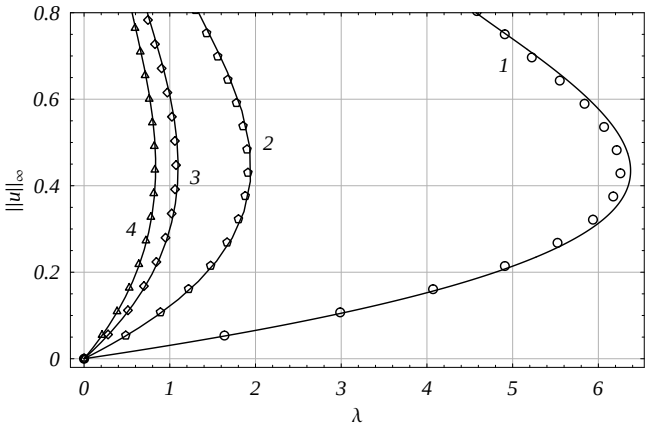

Figure 1.15: Bifurcation diagram for four elliptic MEMS with $b/a = 0.25$ (curve 1), $b/a = 0.5$ (curve 2), $b/a = 0.75$ (curve 3), and $b/a = 0.95$ (curve 4). Solid lines: MLPG solutions with ~ 90 nodes; empty polygons: finite difference solutions with 3500 points.

in voltage increases significantly with a decrease in b/a. Results are compared with finite difference solutions obtained by mapping the elliptic domain into a strip via the change of coordinates given in Appendix B. In confocal elliptic coordinates ξ^1 and ξ^2, homogeneous essential boundary conditions are imposed on the edge $\xi^1 = \text{arctanh}\,(b/a)$, and homogeneous natural boundary conditions are imposed on the remaining edges. A grid of 50×70 points located, respectively, along the ξ^1 and the ξ^2 directions is used. With a considerably reduced number of nodes ($\sim$ 90 versus 3500), the MLPG method is able to reproduce the finite difference results within 2% error for the nondimensional pull-in voltage, and less that 4% error for the nondimensional pull-in displacement.

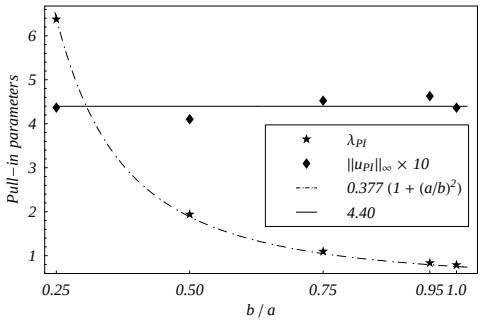

Figure 1.16: Variation of pull-in parameters, λ_{PI} and $\|u_{\text{PI}}\|_\infty$, with the aspect ratio b/a for the elliptic MEMS.

Fig. 1.16 depicts the variation of the pull-in parameters, λ_{PI} and $\|u_{\text{PI}}\|_\infty$, with the aspect ratio b/a. The nondimensional pull-in voltage data are fitted with a quadratic polynomial in a/b (dashed line), and the corresponding nondimensional pull-in maximum deflection data

with a straight line (solid line). Expressions for the aforementioned polynomials are

$$\lambda_{\mathrm{PI}} = 0.377\left(1+\left(\frac{a}{b}\right)^2\right) \tag{1.87a}$$

$$\|u_{\mathrm{PI}}\|_\infty = 0.440. \tag{1.87b}$$

Note that $\|u_{\mathrm{PI}}\|_\infty$ for all four elliptic membranes is the same as that for the circular membrane studied above, cf. Table 1.2. As the aspect ratio approaches 1, λ_{PI} for the elliptical geometry approach that for the circular MEMS. For $a = b$, Eq. (1.87a) gives $\lambda_{\mathrm{PI}} = 0.754$ as opposed to 0.79 in Table 1.2. It shows that λ_{PI} found from Eq. (1.87a) may be 5% off.

1.3.7 Pull-in instability and symmetry breaking in an annular disk

We consider an annular disk of inner radius 0.1, and outer radius 1 clamped along its inner and outer boundaries. Parameters compared are λ_{PI} and $\|u_{\mathrm{PI}}\|_\infty$, and, when a symmetry breaking bifurcation occurs, λ_{SB} and $\|u_{\mathrm{SB}}\|_\infty$. λ_{SB} and $\|u_{\mathrm{SB}}\|_\infty$ represent, respectively, the highest λ for which a symmetry breaking bifurcation occurs, and the corresponding infinity norm of the deflection field.

Following Pelesko, Bernstein & McCuan (2003) we study only one-half of the annular domain. The symmetry breaks after the pull-in instability, and the bifurcated solution does not inherit the symmetry of the domain. We impose homogeneous natural boundary conditions on the straight edges. This condition is restrictive: indeed, there may be nonaxially symmetric solutions that do not satisfy it, see e.g. Pelesko et al. (2003). We compare our results with those obtained in Pelesko et al. (2003) by the finite-difference method with 1600 points.

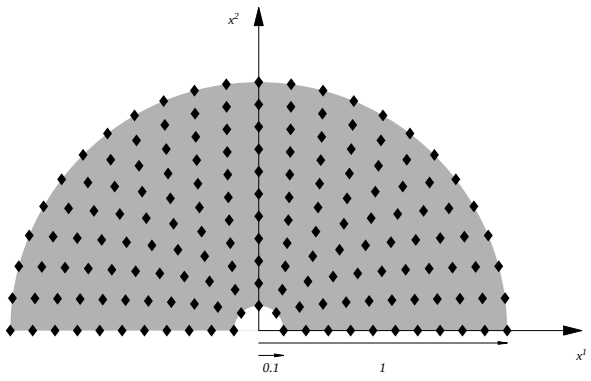

Figure 1.17: Grid of 165 nodes on one-half of an annular disk.

In the MLPG implementation, we use the grid of 165 nodes shown in Fig. 1.17. Values of weight function parameters are the same as those for the circular disk problem studied in Section 1.3.6.2.

Table 1.3: Comparison of the MLPG results with the finite-difference solution for the annular MEMS with inner radius equal to one-tenth of the outer radius.

Finite-difference			MLPG		
$\lambda_{\rm PI}$	$\|u_{\rm PI}\|_\infty$	$\lambda_{\rm SB}$	$\lambda_{\rm PI}$	$\|u_{\rm PI}\|_\infty$	$\lambda_{\rm SB}$
1.544	0.393	1.486	1.548	0.399	1.485

Fig. 1.18 exhibits the infinity norm of the deflection versus the load parameter λ. Numerical solutions from the MLPG and the finite-difference methods are compared in Table 1.3. The symmetry breaking voltage, $\lambda_{\rm SB}$, is less than the pull-in voltage $\lambda_{\rm PI}$, and the maximum difference between the corresponding values of $\lambda_{\rm PI}$, $\|u_{\rm PI}\|_\infty$ and $\lambda_{\rm SB}$ is 1.53%. Since the symmetry breaking point is on the upper portion of the curve, i.e., $\|u_{\rm SB}\|_\infty > \|u_{\rm PI}\|_\infty$, the axisymmetric and the non-axisymmetric configurations are unstable.

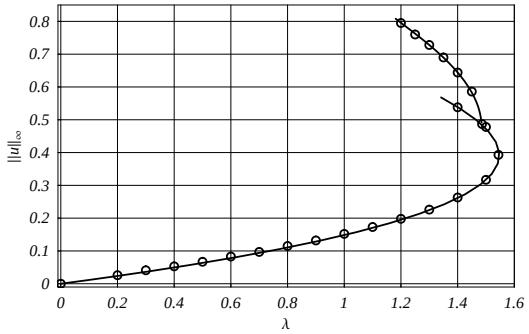

Figure 1.18: Bifurcation diagram for the annular disk MEMS: the finite difference-solution (empty circles) and the MLPG solution (solid line).

Figs. 1.19(a) and 1.19(b) report the symmetric, and the asymmetric deformed shapes of the annular disk after the pull-in, for $\lambda = 1.37$, and $\lambda = 1.18$ respectively.

Fig. 1.20(a) depicts the variation of the pull-in parameters, $\lambda_{\rm PI}$ and $\|u_{\rm PI}\|_\infty$, with the ratio (inner radius)/(outer radius), keeping the outer radius at the constant value 1. The MLPG results are computed using a grid of ~ 165 nodes. The nondimensional pull-in voltage data are fitted with a quadratic polynomial (dashed line), and the corresponding nondimensional pull-in maximum deflections with a polynomial of degree zero (solid line). Expressions for these polynomials are

$$\lambda_{\rm PI} = 1.33 + 16.3\,\rho^2, \tag{1.88a}$$

$$\|u_{\rm PI}\|_\infty = 0.390, \tag{1.88b}$$

where ρ =(inner radius)/(outer radius). Whereas the maximum pull-in deflection is nearly independent of the ratio ρ, the pull-in voltage increases essentially quadratically with this

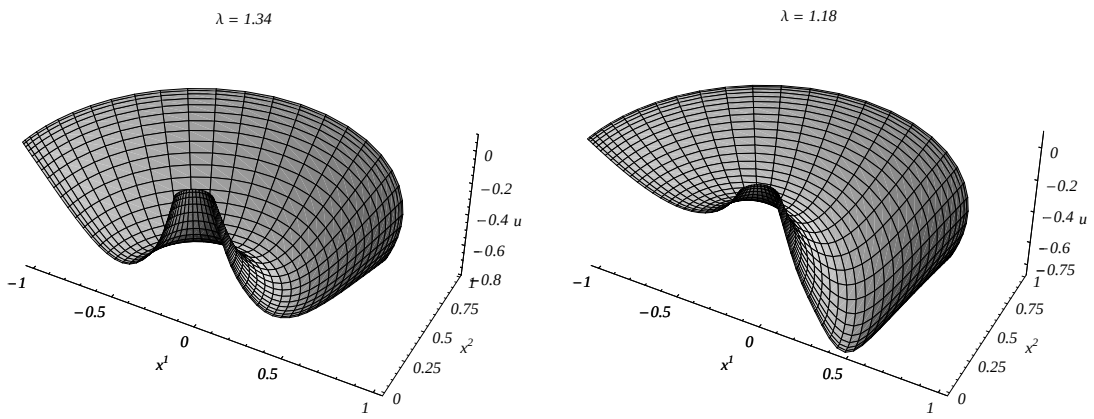

(a) (b)

Figure 1.19: (a) Symmetric, and (b) asymmetric solutions for the annular disk MEMS with $\lambda = 1.34$ and $\lambda = 1.18$, respectively.

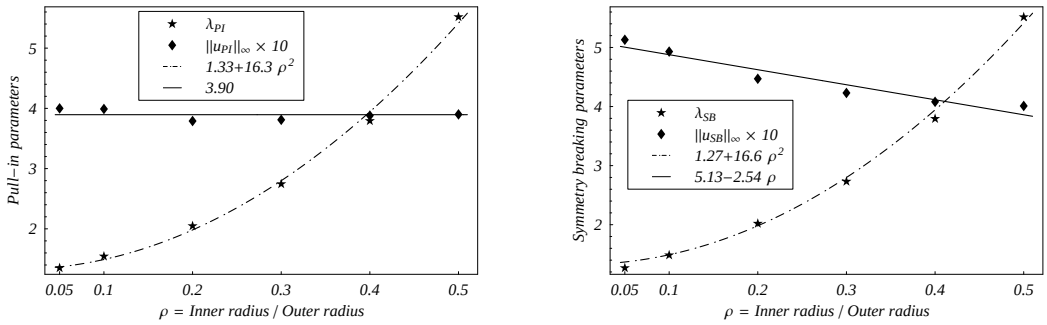

(a) (b)

Figure 1.20: Variation with the ratio (inner radius)/(outer radius) for the annular MEMS of (a) pull-in parameters $\lambda_{\rm PI}$ and $\|u_{\rm PI}\|_\infty$, and (b) symmetry breaking parameters $\lambda_{\rm SB}$ and $\|u_{\rm SB}\|_\infty$.

ratio. The pull-in deflection for an annular circular membrane is smaller than that for a circular and an elliptic membrane. Since $\|u_{\rm PI}\|_\infty$ for an annular membrane is smaller than that for a circular membrane, a tiny hole at the center of a circular membrane can decrease $\|u_{\rm PI}\|_\infty$ by 12% if the membrane is clamped around both peripheries, and increase the pull-in voltage by 68%. Note that in the limit as $\rho \to 0$, $\|u_{\rm PI}\|_\infty$ and $\lambda_{\rm PI}$ for the annular membrane do not approach their corresponding values for the circular membrane because of different boundary conditions. Whereas for the circular membrane $\|u_{\rm PI}\|_\infty$ occurs at the center, for the limiting case of the annular membrane $u_{\rm PI}$ will vanish at the center.

Fig. 1.20(b) exhibits the dependence of the symmetry breaking parameters, $\lambda_{\rm SB}$ and $\|u_{\rm SB}\|_\infty$, upon ρ. With increasing inner radius, the nondimensional pull-in voltage $\lambda_{\rm PI}$ significantly increases due to increased stiffness of the system, and the same holds for the nondimensional lowest symmetry breaking voltage, $\lambda_{\rm SB}$. Whereas the nondimensional pull-in maximum de-

flection, $\|u_{\rm PI}\|_\infty$, is virtually independent of the inner radius of the disk, the nondimensional symmetry breaking maximum deflection, $\|u_{\rm SB}\|_\infty$, decreases with increasing inner radius. Expressions for the best fit polynomials in Fig. 1.20(b) are

$$\lambda_{\rm SB} = 1.27 + 16.6\,\rho^2, \tag{1.89a}$$

$$\|u_{\rm SB}\|_\infty = 0.513 - 0.254\,\rho. \tag{1.89b}$$

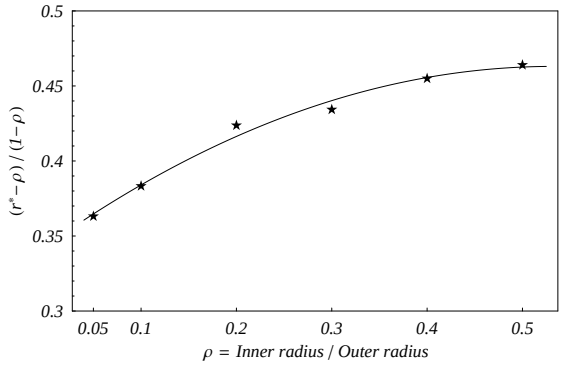

Figure 1.21: Variation of the radial location of the nondimensional pull-in maximum deflection, with the ratio (inner radius)/(outer radius) for the annular MEMS.

Fig. 1.21 shows the variation with the ratio ρ, of the quantity $(r^* - \rho)\,/\,(1 - \rho)$, where r^* is the ratio between the radial location of the nondimensional pull-in maximum displacement $\|u_{\rm PI}\|_\infty$, and the outer radius of the ring. The MLPG data are fitted with a quadratic polynomial (solid line) whose expression is

$$\frac{r^* - \rho}{1 - \rho} = 0.343 + 0.450\,\rho - 0.423\,\rho^2. \tag{1.90}$$

1.3.8 From micro to nano: effect of the scale on pull-in and symmetry breaking parameters of micromembranes

1.3.8.1 Effect on pull-in parameters

We consider the fully electroded rectangular strip, the circular disk, and the annular disk with $\rho = 0.1$. For each of these geometries, we adopt the same distribution of nodes as considered in Sec. 1.3.6.

The nonlinear Poisson equation (1.44) is solved by using the MLPG method in conjunction with the pseudoarclength continuation algorithm described in Sec. 1.3.5. The problem is solved for $\lambda = 0$ in order to determine the critical value, $\mu_{\rm cr}$, of the Casimir force parameter. When $\mu = \mu_{\rm cr}$ the system collapses spontaneously with zero applied voltage. The effect of

the scale on pull-in parameters $\lambda_{\rm PI}$ and $\|u_{\rm PI}\|_\infty$ is investigated by solving Eq. (1.44) with variable λ for different values of μ in the range $[0, \mu_{\rm cr}]$.

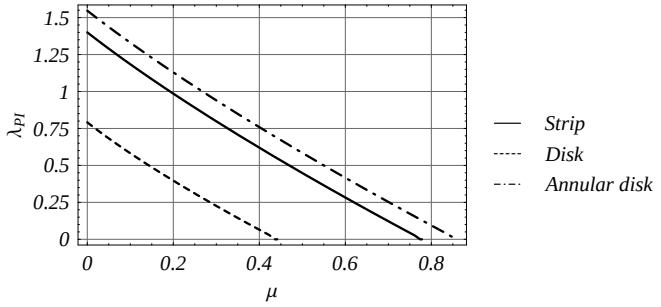

Figure 1.22: Pull-in parameter $\lambda_{\rm PI}$ vs. the Casimir force parameter μ.

In Fig. 1.22 we report the pull-in parameter $\lambda_{\rm PI}$ versus μ for the three cases. As μ increases the pull-in parameter $\lambda_{\rm PI}$ decreases monotonically from its maximum value $\lambda_{\rm PI}^{\rm max}$ corresponding to $\mu = 0$. $\mu = \mu_{\rm cr}$ represents intersection of the curves with the horizontal axis. The curves may be reasonably approximated by straight lines. Using this approximation, the knowledge of the pull-in parameter $\lambda_{\rm PI}^{\rm max}$ and of the critical Casimir parameter $\mu_{\rm cr}$ are sufficient to completely characterize the Casimir effect on the pull-in parameter $\lambda_{\rm PI}$. The slopes of the three fitting straight lines are strikingly similar and they approximately equal -1.8. Thus $\lambda_{\rm PI}$ for the three MEMS geometries can be computed from the following equations:

$$\lambda_{\rm PI} \simeq \begin{cases} 1.40 - 1.8\mu, & \text{strip} \\ 0.791 - 1.8\mu, & \text{disk} \\ 1.55 - 1.8\mu, & \text{annular disk} \end{cases} . \tag{1.91}$$

Whether or not the relationship between $\lambda_{\rm PI}$ and μ can be approximated with a straight line for all values of ρ in the annular disk remains to be investigated.

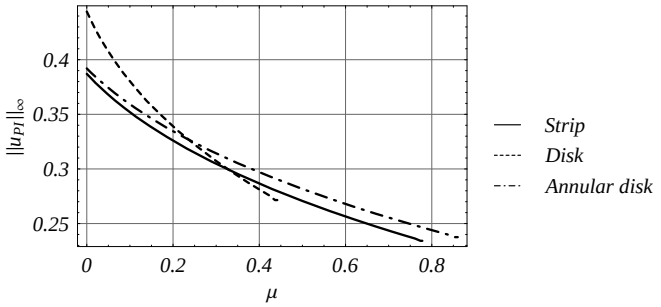

Figure 1.23: Pull-in parameter $\|u_{\rm PI}\|_\infty$ vs. Casimir force parameter μ.

In Fig. 1.23 we show the nondimensional pull-in maximum displacement versus μ. We notice that as μ increases, the nondimensional maximum displacement decreases from its maximum

Table 1.4: Characteristic parameters describing the influence of the Casimir force on pull-in instability.

Geometry	$\lambda_{\mathrm{PI}}^{\max}$	$\|u_{\mathrm{PI}}\|_{\infty}^{\max}$	μ_{cr}	$\|u_{\mathrm{PI}}\|_{\infty}^{\min}$
Strip	1.40	0.387	0.778	0.234
Disk	0.791	0.444	0.442	0.271
Annular disk	1.55	0.392	0.860	0.238

value $\|u_{\mathrm{PI}}\|_{\infty}^{\max}$. This means that reduced deflection ranges are allowable for small devices. The minimum pull-in displacement $\|u_{\mathrm{PI}}\|_{\infty}^{\min}$ is attained when $\mu = \mu_{\mathrm{cr}}$ and refers to the spontaneous collapse of the system without applied voltage.

Numerical values of $\lambda_{\mathrm{PI}}^{\max}$, $\|u_{\mathrm{PI}}\|_{\infty}^{\max}$, μ_{cr}, and $\|u_{\mathrm{PI}}\|_{\infty}^{\min}$ are summarized in Table 1.4. These reveal that the disk experiences the largest nondimensional pull-in maximum displacement as the device size changes: however, the maximum pull-in voltage is for the annular disk.

1.3.8.2 Analysis through a lumped model

A qualitative analysis of the device may be conducted by using the simple lumped model depicted in Fig. 1.1. The device is modeled as a parallel plate capacitor, where both plates are rigid. The upper plate is suspended by a linear spring, and the bottom plate is held fixed. $\bar{u}$ is the displacement of the upper conductor, and it represents the maximum value of the displacement u of the distributed system. The reduced order model is

$$-\kappa\bar{u} = \frac{\lambda}{(1+\bar{u})^2} + \frac{\mu}{(1+\bar{u})^4}, \tag{1.92}$$

where κ is the nondimensional spring stiffness. The constant κ may be computed by solving a sample static problem on the distributed system without Coulomb and Casimir forces. Typically a uniformly distributed load on the movable conductor is considered, see e.g. Lin & Zhao (2005) and Pamidighantam et al. (2002). In this case, the stiffness κ is equal to $1/\|u^*\|_{\infty}$, where u^* is the solution of

$$\triangle u^* \left(x^1, x^2\right) = 1 \tag{1.93}$$

with the proper boundary conditions. The pull-in instability is determined by imposing the force equilibrium (1.92) along with a subsidiary condition expressing that the restoring force is no longer capable of balancing the nonlinear attractive forces. This implies that a nonzero incremental gap results without increasing the applied voltage. Mathematically this condition means that the derivative of both sides of (1.92) with respect to $\bar{u}$ are equal

$$\kappa = \frac{2\lambda}{(1+\bar{u})^3} + \frac{4\mu}{(1+\bar{u})^5}. \tag{1.94}$$

The solution of Eqs. (1.92) and (1.94) can be written as

$$\frac{\lambda_{\rm PI}}{\kappa} = \Lambda\left(\frac{\mu}{\kappa}\right), \qquad \bar{u}_{\rm PI} = -U\left(\frac{\mu}{\kappa}\right), \tag{1.95}$$

where Λ and U are nonlinear functions independent of κ. Fig. 1.24 shows the functions Λ and U for μ/κ in the range $[0, 256/3125)$. We note that $\Lambda(0) = 4/27$ and $\Lambda(256/3125) = 0$. The function Λ can be reasonably approximated by the straight line

$$\Lambda\left(\frac{\mu}{\kappa}\right) \simeq -1.8\frac{\mu}{\kappa} + 0.15. \tag{1.96}$$

The function U is monotonically decreasing. At $\mu = 0$ U equals $1/3$, while at $256/3125$ it equals $1/5$.

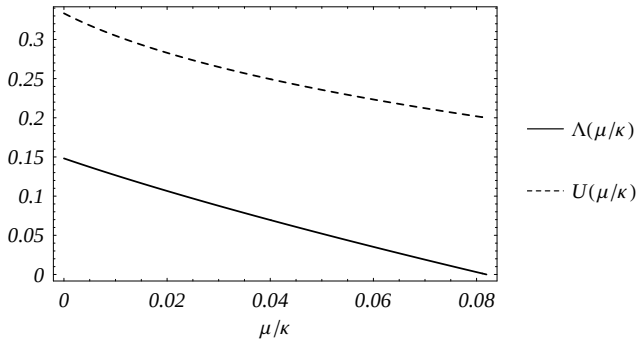

Figure 1.24: Plots of functions Λ and U.

Pull-in displacements predicted by the distributed model significantly differ from those of the lumped model reported as Eq. (1.95). In fact, the maximum pull-in deflection depends on the system geometry and boundary conditions, which are not represented by (1.95). The deflection travel range $[1/3, 1/5]$ predicted by the lumped model is generally inaccurate.

Table 1.5: Characteristic parameters describing the influence of the Casimir force parameter on the pull-in instability as predicted by the lumped model.

Geometry	Lumped model			% deviations	
	κ	$\lambda_{\rm PI}^{\rm max}$	$\mu_{\rm cr}$	$\lambda_{\rm PI}^{\rm max}$	$\mu_{\rm cr}$
Strip	8.00	1.18	0.655	15.7	15.8
Disk	4.00	0.593	0.328	25.0	25.7
Annular disk	8.80	1.30	0.721	16.1	16.1

Even if the influence of the Casimir parameter μ on the pull-in nondimensional voltage $\lambda_{\rm PI}$ is qualitatively described by the lumped model, predictions from it are not accurate, as shown by comparison between results in Table 1.5 with those in Table 1.4. For each geometry, the percentage deviations in $\lambda_{\rm PI}^{\rm max}$ and $\mu_{\rm cr}$ computed from the distributed and the lumped

models are the same with the maximum deviation of 25.7% occurring for the circular disk. Thus the lumped model can be used to compare several preliminary (or prototype) designs of MEMS and the final few analyzed by the high fidelity distributed models.

1.3.8.3 Effect on symmetry breaking

We analyzed the post-instability behavior of the annular ring under the effects of the Coulomb and the Casimir forces by solving the nonlinear Eq. (1.44) for different values of μ in the range $[0, \mu_{\rm cr}]$. We numerically studied one-half of the annular membrane with $\rho = 0.1$, and imposed symmetry conditions on sides contiguous to the removed domain.

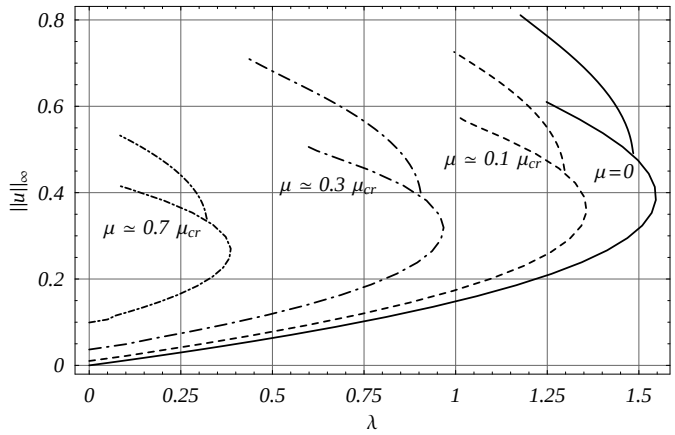

Figure 1.25: Bifurcation diagrams of the annular membrane with $\rho = 0.1$, for four different values of μ.

In Fig. 1.25 we show the maximum deflection $\|u\|_\infty$ versus the voltage parameter λ for four different values of μ. As the Casimir parameter μ varies, the bifurcation point $(\lambda_{\rm SB}, \|u_{\rm SB}\|_\infty)$ moves on the symmetric path, as listed in Table 1.6. As μ increases the ratio $\lambda_{\rm SB}/\lambda_{\rm PI}$ decreases, meaning that the difference in the nondimensional voltage corresponding to symmetry breaking and pull-in instability points increases; the relationship between $\mu/\mu_{\rm cr}$ and $\lambda_{\rm SB}/\lambda_{\rm PI}$ is nonlinear and most likely varies with ρ even though that has not been investigated. In addition, as μ increases the travel range of the device from the pull-in instability to the symmetry breaking point decreases eventually approaching a constant value.

In Fig. 1.26 we report deformed shapes of one half of the annular disk with $\rho = 0.1$ after pull-in instability. In particular, in Fig. 1.26(a) we show the deformed shape associated with a point in the symmetric post-instability path, while in Fig. 1.26(b) the deformed shape corresponds to a point in the asymmetric path. As in Sec. 1.3.7 by considering one-half of the annular disk, we may have missed non-axially symmetric deformation modes.

Table 1.6: Characteristic parameters describing symmetry breaking of the annular disk with $\rho = 0.1$ after pull-in instability.

$\mu/\mu_{\rm cr}$	$\lambda_{\rm SB}/\lambda_{\rm PI}$	$\|u_{\rm SB}\|_\infty/\|u_{\rm PI}\|_\infty - 1$
0	0.960	0.282
0.101	0.956	0.270
0.332	0.935	0.254
0.718	0.831	0.255

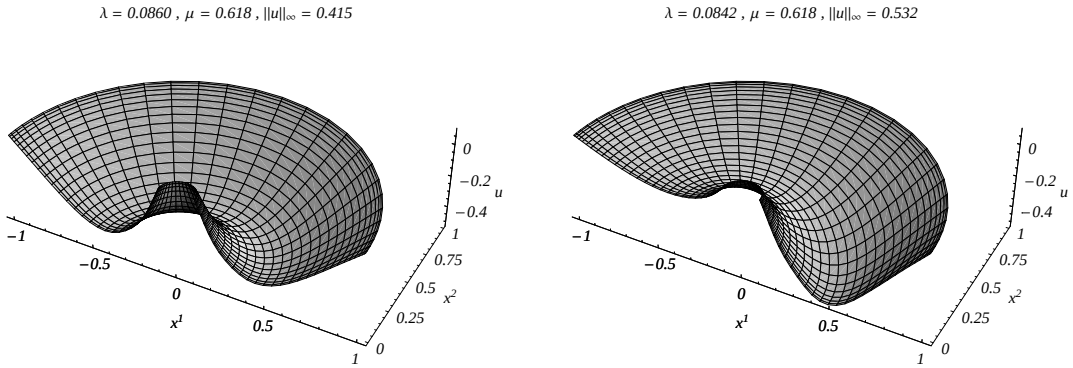

(a) (b)

Figure 1.26: Deformed shapes of the annular disk for $\mu \simeq 0.7\mu_{\rm cr}$: (a) symmetric deformation; (b) asymmetric deformation.

1.3.8.4 Remarks

We conclude with some additional remarks on the importance of the Casimir force in the miniaturization of electrostatically actuated micromembranes, and on the validity of the present analysis. As the device size is reduced, the effect of the Casimir force becomes more important. In the miniaturization process there is a minimum size for the device below which the system spontaneously collapses with zero applied voltage. For example, consider a circular membrane with parameters $L = 100\mu$m, $g_0 = 1\mu$m, $h = 0.1\mu$m, $\sigma_0 = 10$MPa. Substituting these values into Eq. (1.38) gives $\mu = 8.17 \times 10^{-5}$ and the effect of the Casimir force is negligible, see Fig. 1.22. Scaling down the device size by a factor $F = 10$, we have $\mu = 0.817$, which is larger than the critical Casimir parameter $\mu_{\rm cr}$ in Table 1.4. This means that the miniaturized device spontaneously collapses under zero applied voltage. Serry et al. (1998) have studied a rectangular membrane using the distributed model and considering nonlinear stretching effects, and Bárcenas et al. (2005) have used a lumped model to analyze the stiction phenomenon between two conductors made of different materials. These two investigations did not consider the combined effects of the Coulomb and the Casimir forces.

A lumped model seems capable of capturing the qualitative relationship between the pull-

in voltage and the device size. We have given a simple closed form relation (1.96) that seems suitable for MEMS design. The description of the relationship between the device travel range and the device scale, and the symmetry breaking after the pull-in instability necessitate the use of distributed models. The validity of the present work is limited to a class of MEMS for which electrostatic fringing fields and surface roughness (see e.g Ding, Wen & Meng (2001), and Palasantzas & De Hosson (2005)) are negligible, the two bodies are perfect conductors, and for which it is possible to discard bending stiffness and nonlinear stretching effects in the mechanical model of the deformable electrode.

1.4 Electrostatically actuated microbeams

Some of the material in this Section is borrowed from Batra, Porfiri & Spinello (2006*b*).

1.4.1 Electromechanical model

We consider a narrow microbeam of length ℓ, width b, and thickness h either clamped-clamped or clamped-free, as depicted in Fig. 1.27. A beam is considered narrow, when b is less than five times h, see e.g. Osterberg & Senturia (1997). The microbeam is suspended above an infinite ground plane with an initial gap g_0. Both bodies are perfect conductors and are separated by a dielectric medium of permittivity $\epsilon_0\epsilon_\mathrm{r}$, where ϵ_0 is the vacuum permittivity, and ϵ_r is the relative permittivity. A positive potential difference V between the two conductors causes the microbeam to electrostatically deflect downwards. We neglect the effect of Casimir pressure.

1.4.1.1 Non-linear equation for beam's large deflections

We model the microbeam as a von Karman plate undergoing cylindrical bending deformations. Within this theory large deflections, large rotations and small strains of the beam are considered, see, e.g., Landau & Lifshitz (1986). The deflection u (see Fig. 1.27) in the z-direction is governed by, see, e.g., Abdel-Rahman et al. (2002)

$$\varrho bh\ddot{u} + EIu^{IV} - \mathfrak{N}(u)\,u'' = \tilde{F}_\mathrm{e}(u)\,, \tag{1.97}$$

where ϱ is the mass density per unit volume, E is Young's modulus, I the moment of inertia of the cross section about the y-axis, $\mathfrak{N}$ the axial force which is constant along the beam axis, (as required by the equilibrium equation thereby tacitly neglecting inertia forces in the axial direction), $\tilde{F}_\mathrm{e}$ the deflection dependent electrostatic force per unit length. A prime means partial derivative with respect to the axial coordinate x, and a superimposed dot partial

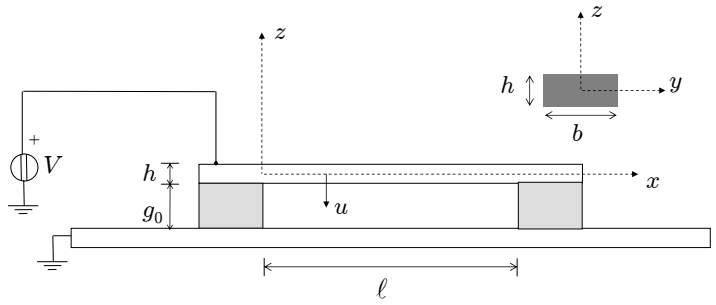

(a)

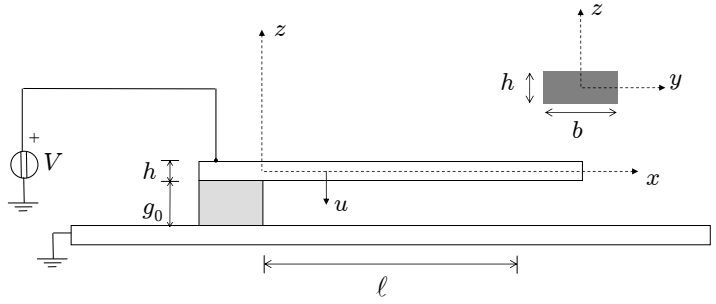

(b)

Figure 1.27: Sketch of the electrostatically actuated microbeams. (a) fixed-fixed; (b) cantilever.

time derivative with respect to the time t. Effects of transverse shear stresses are neglected since for a typical microbeam $\ell/h > 20$, where ℓ is the beam length. For a wide beam the mechanical stiffness, EI, should be modified as given in Osterberg & Senturia (1997).

Even though Eq. (1.97) accounts for the stretching of the mid-surface of the beam, it ignores the effects of the change in the direction of $\tilde{F}_{\mathrm{e}}$ as the beam deforms, consistently with the assumption of small lateral deflections in the mechanical model. Recall that under the assumption that the bodies are perfect conductors, the Coulomb force acts along the normal to their bounding surfaces.

For a cantilever beam the axial force vanishes, while for a clamped-clamped beam it is given by

$$\mathfrak{N}(u) = \frac{Ebh}{2\ell} \int_0^\ell (u')^2 \, \mathrm{d}x + \mathfrak{N}_0, \tag{1.98}$$

where $\mathfrak{N}_0$ is the residual axial load in the undeformed or the undeflected beam. For a narrow beam, the residual axial load is $\mathfrak{N}_0 = \tilde{\sigma} bh$, where $\tilde{\sigma}$ is the effective residual axial stress. The residual axial stress is equal to $\sigma_0 (1 - \nu)$, where σ_0 is the initial uniform biaxial stress in the material, see e.g. Osterberg & Senturia (1997) and ν is Poisson's ratio for the material of the beam.

For a fixed-fixed beam, the deflection is subjected to the following four kinematic boundary conditions:

$$u(0,t) = 0, \quad u'(0,t) = 0, \quad u(\ell,t) = 0, \quad u'(\ell,t) = 0, \tag{1.99}$$

while for a cantilever beam the deflection should satisfy the two kinematic boundary conditions at the clamped end and the two kinetic boundary conditions at the free end $x = \ell$:

$$u(0,t) = 0, \quad u'(0,t) = 0, \quad u''(\ell,t) = 0, \quad u'''(\ell,t) = 0. \tag{1.100}$$

Thus the deflection and the slope of the beam vanish at a clamped edge, and the shear force and the bending moment vanish at a free edge.

1.4.2 Distributed force due to electric field

The distributed force, $\tilde{F}_{\mathrm{e}}(u)$, on the deformable microbeam due to the electric field depends on the potential difference between the two conductors and on their geometries. Since only small deformations of the beam are considered, it is reasonable to assume that at every point x the electrostatic force per unit length, $\tilde{F}_{\mathrm{e}}$, depends only on the local deflection $u(x,t)$ and equals the force per unit length acting on an infinitely long straight beam separated by the distance $g(x,t) = g_0 - u(x,t)$ from a ground plane as shown in Fig. 1.28. The force $\tilde{F}_{\mathrm{e}}$ may be computed by differentiating the energy per unit length stored in the capacitor with respect to the gap g, i.e.,

$$\tilde{F}_{\mathrm{e}} = -\frac{1}{2} V^2 \frac{\partial C_{\mathrm{g}}}{\partial g}. \tag{1.101}$$

Here C_{g} is the capacitance per unit length of the 2-D conductor system and V is the voltage difference between the two plates. The capacitance C_{g} is comprised of the parallel-plate capacitance, and the fringing field capacitance due to the finite width and the finite thickness of the beam.

1.4.2.1 Dimensionless governing equations

For convenience we introduce the nondimensional deflection $\hat{u} = u/g_0$, the nondimensional abscissa $\hat{x} = x/\ell$, and the nondimensional time $\hat{t} = t/T$, where

$$T = \left(\frac{\varrho bh\ell^4}{EI} \right)^{\frac{1}{2}}. \tag{1.102}$$

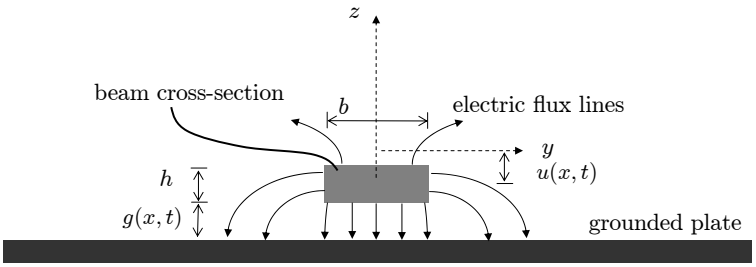

Figure 1.28: Schematic view of the electric flux lines on the beam cross section with grounded electrode.

In terms of non-dimensional variables Eq. (1.97) becomes

$$\ddot{\hat{u}}\left(\hat{x},\hat{t}\right)+\hat{u}^{IV}\left(\hat{x},\hat{t}\right)-\left[\mathfrak{N}_1\int_0^1\left(\hat{u}'\right)^2\mathrm{d}\hat{x}+\hat{\mathfrak{N}}_0\right]\hat{u}''\left(\hat{x},\hat{t}\right)=\hat{F}_{\mathrm{e}}\left(\hat{u}\left(\hat{x},\hat{t}\right)\right), \tag{1.103}$$

where for a clamped-clamped beam

$$\mathfrak{N}_1=6\frac{g_0^2}{h^2},\qquad \hat{\mathfrak{N}}_0=\frac{\mathfrak{N}_0\ell^2}{EI}=12\frac{\tilde{\sigma}\ell^2}{Eh^2},\qquad \hat{F}_{\mathrm{e}}(\hat{u}(\hat{x}))=\frac{12\ell^4}{Eg_0bh^3}\tilde{F}_{\mathrm{e}}(u(x)), \tag{1.104}$$

and for a cantilever beam

$$\mathfrak{N}_1=\hat{\mathfrak{N}}_0=0. \tag{1.105}$$

The capacitance per unit length C_{g} can be expressed as

$$C_{\mathrm{g}}=C_{\mathrm{g}}^0\mathcal{F}\left(\beta,\eta\right), \tag{1.106}$$

where $\mathcal{F}$ represents the fringing field correction function,

$$C_{\mathrm{g}}^0=\epsilon_0\epsilon_{\mathrm{r}}\frac{b}{g} \tag{1.107}$$

is the capacitance per unit length when all fringing effects are neglected, and

$$\beta=\frac{h}{b},\qquad \eta=\frac{h}{g}. \tag{1.108}$$

Therefore, the dimensionless electrostatic force is

$$\hat{F}_{\mathrm{e}}=\frac{\lambda}{\left(1-\hat{u}\right)^2}\left(\mathcal{F}+\eta\frac{\partial\mathcal{F}}{\partial\eta}\right), \tag{1.109}$$

where the electrostatic load parameter λ is given by

$$\lambda=\frac{6\ell^4\epsilon_0\epsilon_{\mathrm{r}}V^2}{Eh^3g_0^3}. \tag{1.110}$$

In Sec. 1.4.3 we will derive an expression for $\hat{F}_{\mathrm{e}}$ applicable to a narrow microbeam.

Henceforth we drop the superimposed hat on the dimensionless variables. Therefore the governing Eq. (1.97) in terms of nondimensional variables is

$$\ddot{u}(x,t) + u^{IV}(x,t) - \mathfrak{N}(u)\, u''(x) = F_{\mathrm{e}}(u(x,t)), \tag{1.111}$$

where for a clamped-clamped beam

$$\mathfrak{N}(u) = \mathfrak{N}_1 \int_0^1 (u')^2 \,\mathrm{d}x + \mathfrak{N}_0, \tag{1.112}$$

and for a cantilever beam

$$\mathfrak{N}(u) = 0. \tag{1.113}$$

1.4.2.2 Weak formulation of the problem

For a clamped-clamped microbeam, we introduce the following weak formulation (see e.g. Mura & Koya (1992)), of the problem described by the governing Eq. (1.111), and the nondimensional version of the boundary conditions (1.99):

$$\begin{aligned} \int_0^1 \ddot{u}\tilde{u}\mathrm{d}x \;&+\; \int_0^1 u''\tilde{u}''\,\mathrm{d}x + \mathfrak{N}(u)\int_0^1 u'\tilde{u}'\mathrm{d}x - \int_0^1 F_{\mathrm{e}}\tilde{u}\mathrm{d}x \\ &+\; \gamma_1\tilde{u}(0) + \gamma_2\tilde{u}'(0) + \gamma_3\tilde{u}(1) + \gamma_4\tilde{u}'(1) \\ &+\; \tilde{\gamma}_1 u(0) + \tilde{\gamma}_2 u'(0) + \tilde{\gamma}_3 u(1) + \tilde{\gamma}_4 u'(1) = 0. \end{aligned} \tag{1.114}$$

Here, γ_1, γ_2, γ_3, and γ_4 are Lagrange multipliers used to impose the four kinematic boundary conditions (1.99), $\tilde{u}$ is a smooth test function which need not satisfy the kinematic boundary conditions, and $\tilde{\gamma}_1$, $\tilde{\gamma}_2$, $\tilde{\gamma}_3$, and $\tilde{\gamma}_4$ are arbitrary scalar numbers.

For a cantilever microbeam Eq. (1.114) becomes

$$\begin{aligned} \int_0^1 \ddot{u}\tilde{u}\mathrm{d}x \;&+\; \int_0^1 u''\tilde{u}''\,\mathrm{d}x - \int_0^1 F_{\mathrm{e}}\tilde{u}\mathrm{d}x \\ &+\; (\gamma_1\tilde{u}(0) + \gamma_2\tilde{w}'(0)) + (\tilde{\gamma}_1 w(0) + \tilde{\gamma}_2 w'(0)) = 0, \end{aligned} \tag{1.115}$$

where only two Lagrange multipliers are employed since only two kinematic boundary conditions are prescribed.

The consideration of the Lagrange multipliers allows for the simultaneous application of the MLPG and the FE methods. Note that the GMLS basis functions (see Appendix A.2) used in the MLPG method do not have the Kronecker delta property, see e.g. Atluri & Zhu (1998), and special techniques, such as the method of Lagrange multipliers, are needed to enforce kinematic boundary conditions.

1.4.3 Computation of the electrical force field

The problem of computing the capacitance per unit length of the present system of conductors has been addressed in the literature on semiconductor-integrated circuits (Barke (1988)), and microwave striplines (Collins (1992)). Several empirical and analytical expressions have been proposed but none of them seem to be applicable to a narrow microbeam The approach followed here differs from that of Sec. 1.3.2 where Eqs. (1.10) were first solved in the medium exterior to the conductors.

We derive here an empirical formula for the capacitance per unit length of the line to ground system, shown in Fig. 1.28 for a narrow microbeam. The empirical formula is based on a least square fitting of numerical values obtained by using the well-known method of moments (MoM) (see e.g. Harrington (1993)), outlined in Appendix C for piecewise constant basis functions and the collocation method.

1.4.3.1 Empirical formula for the capacitance

The capacitance $C_{\rm g}$ of the line to ground system of Fig. 1.28 equals twice the capacitance $\bar{C}_{\rm g}$ of two identical rectangular conductors depicted in Fig. 1.29. Therefore, we consider this auxiliary system involving finite size conductors and exploit symmetry conditions about the plane $z = 0$.

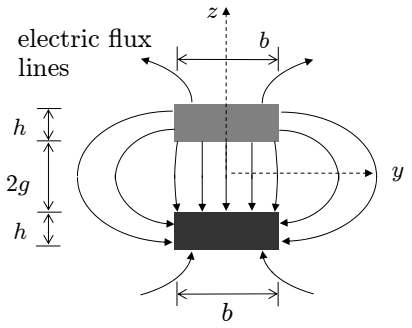

Figure 1.29: A system of auxiliary conductors for computing the electrostatic capacitance.

By using the MoM, we numerically compute the capacitance per unit length $C_{\rm g}$ for different values of the dimensionless parameters β and η defined in (1.108) ranging from 0.2 to 2 and 0.4 to 5 respectively. The resulting data are then least-squares fitted by the following function:

$$\frac{C_{\rm g}}{\epsilon_0 \epsilon_{\rm r}} = \frac{\eta}{\beta} + c_0 + c_1 \left(\frac{\eta}{\beta}\right)^{c_2} + c_3 \eta^{c_4} + c_5 \beta^{c_6} + c_7 \left(\eta\beta\right)^{c_8}, \tag{1.116}$$

where $c_0, c_1, \ldots, c_8$ are constants. The first term on the right-hand side of Eq. (1.116) de-

scribes the parallel-plate capacitance, the third term accounts for the fringing field capacitance due to the finite width b (i.e., flux lines emanating from the top surface), the fourth term models the fringing field capacitance due to the finite thickness h (i.e., flux lines originated form the side surfaces of the beam), the fifth term accounts for the aspect ratio of beam's cross-section, and the last term accounts for the combined effect of the aspect ratio and the finite thickness of the beam. Numerical values of the optimized constants are listed in Table 1.7.

Table 1.7: Numerical values of constants in Eq. (1.116).

c_0	c_1	c_2	c_3	c_4	c_5	c_6	c_7	c_8
-5.40	4.60	0.325	0.126	-0.554	-0.0388	0.891	3.47	0.118

In the chosen range of variation for β and η, the maximum deviation in the capacitance between the empirical estimate obtained by substituting values from Table 1.7 into Eq. (1.116) and the fully converged numerical solution achieved by using the MoM is less than 0.2%. Therefore, the fringing field correction in Eq. (1.106) is

$$\mathcal{F}(\beta,\eta) = 1 - 0.18\frac{\beta}{\eta^{1.55}} + 0.579\left(\frac{\beta}{\eta}\right)^{0.874} + 0.408\frac{\beta^{1.12}}{\eta^{0.882}}. \tag{1.117}$$

1.4.3.2 Validation of the capacitance estimate

In Table 1.8 we compare capacitance values computed from Eq. (1.106) by substituting in it the expression (1.117) for the fringing field correction $\mathcal{F}(\beta,\eta)$, and from relations available in the literature, i.e. Palmer's (1937) formula

$$\mathcal{F}_{\mathrm{P}}(\beta,\eta) = 1 + \frac{2}{\pi}\frac{\beta}{\eta}\left(1 + \ln\left(\pi\frac{\eta}{\beta}\right)\right), \tag{1.118}$$

the parallel-plate approximation $\mathcal{F}_{\mathrm{PP}}(\beta,\eta) = 1$, and the Meijs-Fokkema relation (Meijs & Fokkema (1984))

$$\mathcal{F}_{\mathrm{MF}}(\beta,\eta) = 1 + 0.77\frac{\beta}{\eta} + 1.06\left(\frac{\beta}{\eta}\right)^{0.75} + 1.06\frac{\beta}{\eta^{0.5}}. \tag{1.119}$$

We use a fully converged solution obtained with the MoM as the reference for comparing the accuracies of different formulas. It is clear that, for narrow microbeams with $0.5 \le b/h \le 5$, $0.2 \le g/h \le 2$, the Palmer formula and the parallel plate approximation give erroneous values of the capacitance per unit line. As stated in Meijs & Fokkema (1984), values from the Meijs-Fokkema formula have a maximum deviation of 2% for $\eta/\beta = b/g \ge 1,\ 0.1 \le \eta = h/g \le 4$ and of 6% for $\eta/\beta \ge 0.3$ and $\eta < 10$. The estimate is worst when the gap size is larger than

Table 1.8: Comparison between the capacitance per unit length computed with Eq. (1.106) by substituting in it the expression (1.117) for the fringing field corrections and from three available formulas, with that obtained by the method of moments.

Geometry		MoM	% Deviations			
β	η	$C_g/(\epsilon_0\epsilon_r)$	Eq. (1.117)	Meijs-Fokkema (Eq. (1.119))	Palmer (Eq. (1.118))	Parallel-Plate
0.2	0.5	5.37	0.121	−0.4	−17.2	−53.5
0.2	1	8.42	< 0.1	−0.1	−12.3	−40.7
0.2	2.5	16.80	< 0.1	0.8	−8.0	−25.6
0.2	5	30.06	< 0.1	1.5	−5.6	−16.9
0.5	0.5	3.61	< 0.1	−0.8	−34.5	−72.3
0.5	1	5.12	< 0.1	−0.6	−25.7	−61.0
0.5	2.5	8.97	< 0.1	−0.7	−17.7	−44.3
0.5	5	14.71	< 0.1	2.1	−12.9	−32.1
1	0.5	2.96	−0.102	−1.7	−51.9	−83.1
1	1	3.96	< 0.1	−1.8	−40.3	−74.8
1	2.5	6.29	< 0.1	−0.1	−29.3	−60.2
1	5	9.52	< 0.1	2.2	−22.4	−47.5
2	0.5	2.59	< 0.1	−2.9	−71.8	−90.4
2	1	3.34	< 0.1	−3.5	−57.3	−85.0
2	2.5	4.90	< 0.1	−1.7	−43.8	−74.5
2	5	6.88	< 0.1	1.4	−53.3	−63.7

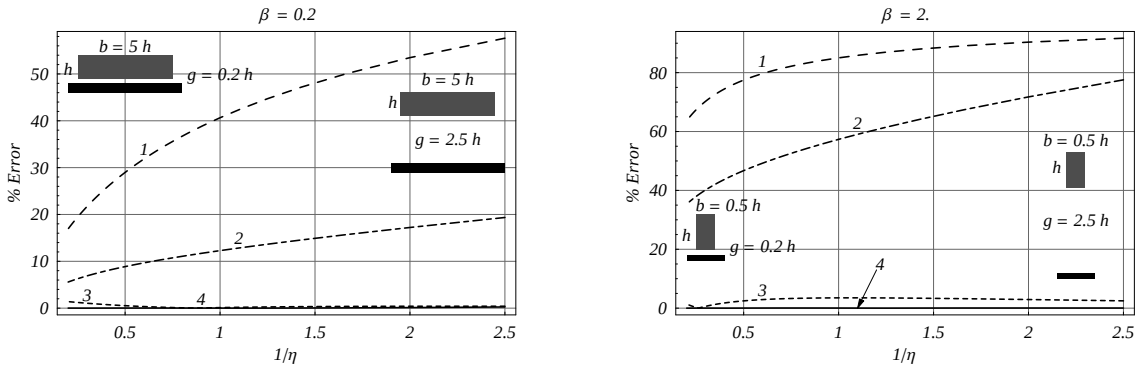

Figure 1.30: Taking the capacitance computed with the method of moments as reference, comparison of the error in the capacitance per unit length for a narrow microbeam estimated with different methods. Curves 1, 2, 3, and 4 refer to the parallel plate approximation, the Palmer formula (Eq. (1.118)), the Meijs-Fokkema (Eq. (1.119)) formula, and the present work (Eq. (1.117)).

the beam width, i.e. $g/b > 1$. In this case, the error in the capacitance values from the Meijs-Fokkema formula is $\sim 6\%$ which is usually unacceptable.

In Fig. 1.30 we have plotted the percentage error in the capacitance versus the gap/thickness for $\beta = h/b = 0.2$ (narrow beam), and $\beta = 2$ (significantly narrow beam) computed with the different formulas, and taking as reference the numerical values obtained with the MoM. As expected the present interpolation formula (1.117) provides accurate results for both values of β. The Mejis-Fokkema relation (1.119) gives precise results for a narrow beam but has moderate discrepancies for a significantly narrow beam. The Palmer expression (1.118) and the parallel plate approximation which totally neglect the effect of the finite thickness of the beam provide poor estimates of the electric capacitance for narrow and significantly narrow micro-beams yielding large errors. The electrostatic force estimated from these two relations is acceptable only for small gaps.

1.4.4 One degree-of-freedom (d.o.f.) model

A closed-form solution of Eq. (1.111) cannot be found. Here we give an approximate solution based on a one d.o.f. model of the MEMS. The proposed one d.o.f. model should not be confused with the lumped model used in Sec. 1.3.8.The approximate solution is constructed by expressing the dimensionless deflection field as the product of an unknown time-dependent deflection parameter $\zeta(t)$ and a given trial function $\bar{u}(x)$ satisfying the kinematic boundary conditions:

$$u(x,t) = \zeta(t)\bar{u}(x). \tag{1.120}$$

The governing equation for ζ is derived by multiplying both sides of Eq. (1.111) by $\bar{u}$, integrating over the beam span, and substituting the approximate solution (1.120) into the

resulting equation. After integrating by parts the governing equation for $\zeta(t)$ becomes

$$m\ddot{\zeta} + (k_0 + k_1)\zeta + k_2\zeta^3 = \lambda f_{\mathrm{e}}(\zeta), \tag{1.121}$$

where

$$\begin{aligned} m &= \int_0^1 (\bar{u}(x))^2 \mathrm{d}x, && (1.122a)\\ k_0 &= \int_0^1 (\bar{u}''(x))^2 \mathrm{d}x, && (1.122b)\\ k_1 &= \mathfrak{N}_0 \int_0^1 (\bar{u}'(x))^2 \mathrm{d}x, && (1.122c)\\ k_2 &= \mathfrak{N}_1 \left(\int_0^1 (\bar{u}'(x))^2 \mathrm{d}x \right)^2, && (1.122d)\\ f_{\mathrm{e}}(\zeta) &= \frac{1}{\lambda} \int_0^1 F_{\mathrm{e}}(\zeta \bar{u}(x)) \bar{u}(x) \mathrm{d}x. && (1.122e) \end{aligned}$$

Note that F_{e} is linear in λ, therefore f_{e} is independent of λ. The left-hand side of Eq. (1.121) is comprised of the inertia and the restoring elastic forces, while the right-hand side represents the electrostatic force. Furthermore, the term multiplying ζ represents the stiffness of a linear elastic beam and that multiplying ζ^3 the strain-stiffening effect. The lumped electrostatic force depends on the adopted fringing field correction and cannot, in general, be expressed analytically.

The pull-in parameters are determined by discarding the inertia term in Eq. (1.121):

$$(k_0 + k_1)\zeta + k_2\zeta^3 = \lambda f_{\mathrm{e}}(\zeta), \tag{1.123}$$

Note that Eq. (1.123) gives the admissible equilibrium states of the system. As the parameter λ increases from zero the overall stiffness of the system decreases and it vanishes at the pull-in instability. Therefore, pull-in occurs in an equilibrium state for which the first derivative of the equilibrium equation with respect to the deflection parameter ζ vanishes.

This implies that the pull-in deflection and the pull-in voltage should satisfy simultaneously Eq. (1.123) and its derivative with respect to ζ, i.e.,

$$(k_0 + k_1) + 3k_2\zeta^2 = \lambda \frac{\mathrm{d}f_{\mathrm{e}}(\zeta)}{\mathrm{d}\zeta}. \tag{1.124}$$

By eliminating λ from Eqs. (1.123) and (1.124), we obtain

$$f_{\mathrm{e}}(\zeta)((k_0 + k_1) + 3k_2\zeta^2) - \frac{\mathrm{d}f_{\mathrm{e}}(\zeta)}{\mathrm{d}\zeta}((k_0 + k_1)\zeta + k_2\zeta^3) = 0. \tag{1.125}$$

By solving Eq. (1.125) for ζ, and by substituting the value of ζ into Eq. (1.123) we determine the pull-in instability parameters, i.e., the deflection and the voltage. We emphasize that

once the trial function $\bar{u}(x)$ has been chosen, Eq. (1.125) reduces to a nonlinear algebraic equation for ζ, where the derivative $\mathrm{d}f_{\mathrm{e}}(\zeta)/\mathrm{d}\zeta$ can be computed for any ζ by numerical integration. In general, Eq. (1.123) cannot be solved analytically and standard root finding techniques such as the bisection algorithm, see e.g. Press, Teukolsky, Vetterling & Flannery (1992), may be applied.

When k_2 is different from zero, fringing fields are taken into account. By using arbitrary trial functions, multiple solutions may be found. We determine the pull-in parameters by considering the lowest root of Eq. (1.125). In our numerical simulations, we found that Eq. (1.125) has one solution only.

The fundamental frequency of the deflected beam at a given $0 \leq \bar{\lambda} < \lambda_{\mathrm{PI}}$ is computed by linearizing Eq. (1.121) about the deflected shape obtained as a solution of the static problem, and by solving the corresponding eigenvalue problem. Note that, once the pull-in parameters are determined, for any $0 \leq \bar{\lambda} \leq \lambda_{\mathrm{PI}}$, the corresponding deflection parameter $0 \leq \zeta(\bar{\lambda}) \leq \zeta_{\mathrm{PI}}$ is given directly by Eq. (1.123). Therefore, for every nondimensional dc voltage $\bar{\lambda}$ the nondimensional fundamental frequency[‡] of the deflected beam is given by

$$\omega(\bar{\lambda}) = \left(\frac{1}{m} \left(k_0 + k_1 + 3k_2 \zeta(\bar{\lambda})^2 - \bar{\lambda} \frac{\mathrm{d}f_{\mathrm{e}}}{\mathrm{d}\zeta}(\zeta(\bar{\lambda})) \right) \right)^{\frac{1}{2}}; \tag{1.126}$$

$\omega(0)$ is the fundamental frequency of the prestressed undeflected beam. When $\bar{\lambda}$ approaches λ_{PI}, the frequency $\omega(\bar{\lambda})$ drops rapidly to zero, see e.g., Abdel-Rahman et al. (2002).

As discussed by Abdel-Rahman et al. (2002), the electrostatic force provides a softening effect on the overall mechanical stiffness, while the membrane stretching introduces strain hardening. The resonance frequency $\omega(\bar{\lambda})$ is determined by a combination of these two opposite effects which balances out at the null frequency.

We choose as trial function $\bar{u}(x)$ the normalized linear static deflection of the microbeam due to a uniformly distributed applied load. Therefore, for a clamped-clamped microbeam we take

$$\bar{u}(x) = 16x^2(1-x)^2, \tag{1.127}$$

and consequently

$$m = \frac{128}{315}, \quad k_0 = \frac{1024}{5}, \quad k_1 = N_0 \frac{512}{105}, \quad k_2 = N_1 \left(\frac{512}{105} \right)^2. \tag{1.128}$$

For a cantilever microbeam we choose

$$\bar{u}(x) = \frac{1}{3} x^2 (6 - 4x + x^2), \tag{1.129}$$

[‡]The corresponding dimensional quantity is obtained by dividing the nondimensional one by the time T given in Eq. (1.102).

thus

$$m = \frac{2}{5}, \quad k_0 = \frac{16}{5}, \quad k_1 = 0, \quad k_2 = 0. \tag{1.130}$$

In beam's undeformed configuration, the electrostatic force acts as a uniformly distributed load, and the nonlinear mechanical stiffness vanishes. Therefore the chosen trial function represents the actual microbeam deflection when small voltages are involved. Moreover, from the analysis of the static problem with the MLPG and the FE methods it appears that the form of the deflection field does not qualitatively change as the voltage is increased. These allude to the effectiveness of the present choice, which is validated by numerical results presented in Sec. 1.4.6.

1.4.5 Numerical methods

1.4.5.1 Semidiscrete nonlinear formulation

In order to seek an approximate solution of the nonlinear problem, we find the deflection by using the GMLS basis functions (Atluri, Cho & Kim (1999)) outlined in Appendix A.2, or the Hermite polynomial basis functions for the FE work (Bathe (1996)). In both cases, indicating by N the number of nodes on the beam, the trial solution is expressed as

$$u^h(x,t) = \boldsymbol{\psi}(x)^{\mathrm{T}} \hat{\mathbf{u}}(t), \tag{1.131}$$

where $\boldsymbol{\psi}(x)$ is a $2N$ vector comprised of the basis functions, and $\hat{\mathbf{u}}(t)$ is the $2N$ vector of time-dependent nodal unknowns. For the GMLS approximation, $\hat{\mathbf{u}}$ does not represent the actual nodal values but the so called fictitious nodal values (Atluri et al. (1999)). The number of unknowns in the problem is $2N + N_{\mathrm{L}}$, where N_{L} is the number of Lagrange multipliers, which equals 4 for a clamped-clamped beam, see Eq. (1.114), and 2 for a cantilever beam, see Eq. (1.115). By substituting the approximation (1.131) in either Eq. (1.114) or Eq. (1.115), by considering displacement test functions of the form

$$\tilde{u}(x) = \boldsymbol{\upsilon}\, \boldsymbol{\psi}(x) \tag{1.132}$$

where $\boldsymbol{\upsilon}$ is a $2N$ row vector of arbitrary constants, and by introducing a N_{L} vector $\tilde{\boldsymbol{\gamma}}$ of arbitrary constants, we get the following set of nonlinear ordinary differential equations

$$\mathbf{M}\, \ddot{\hat{\mathbf{u}}} + \mathbf{K}(\hat{\mathbf{u}})\, \hat{\mathbf{u}} + \mathbf{G}(\lambda, \hat{\mathbf{u}}) + \mathbf{V}^{\mathrm{T}} \boldsymbol{\gamma} = \mathbf{0}, \tag{1.133a}$$

$$\mathbf{V}\, \hat{\mathbf{u}} = \mathbf{0}, \tag{1.133b}$$

where

$$\mathbf{M} = \int_0^1 \boldsymbol{\psi}(x) \boldsymbol{\psi}(x)^{\mathrm{T}} \mathrm{d}x, \tag{1.134a}$$

$$\mathbf{K}\left(\hat{\mathbf{u}}\right) = \int_0^1 \boldsymbol{\psi}''(x)\boldsymbol{\psi}''(x)^{\mathrm{T}}\mathrm{d}x + \mathfrak{N}(\boldsymbol{\psi}(x)^{\mathrm{T}}\hat{\mathbf{u}}) \int_0^1 \boldsymbol{\psi}'(x)\boldsymbol{\psi}'(x)^{\mathrm{T}}\mathrm{d}x, \tag{1.134b}$$

$$\mathbf{G}\left(\lambda, \hat{\mathbf{u}}\right) = -\int_0^1 F_{\mathrm{e}}\left(\lambda, \boldsymbol{\psi}(x)^{\mathrm{T}}\mathbf{u}\right)\boldsymbol{\psi}(x)\mathrm{d}x, \tag{1.134c}$$

clamped-clamped:

$$V_{1i} = \psi_i(0), \quad V_{2i} = \psi_i'(0),$$

$$V_{3i} = \psi_i(1), \quad V_{4i} = \psi_i'(1), \tag{1.134d}$$

$$\boldsymbol{\gamma} = \left[\gamma_1 \;\; \gamma_2 \;\; \gamma_3 \;\; \gamma_4\right]^{\mathrm{T}}, \tag{1.134e}$$

cantilever:

$$V_{1i} = \psi_i(0), \quad V_{2i} = \psi_i'(0), \tag{1.134f}$$

$$\boldsymbol{\gamma} = \left[\gamma_1 \;\; \gamma_2\right]^{\mathrm{T}}, \tag{1.134g}$$

and $i = 1, \ldots, 2N$.

Let rows of the $(2N - N_{\mathrm{L}}) \times 2N$ matrix $\mathbf{Y}$ be comprised of $(2N - N_{\mathrm{L}})$ linearly independent null vectors of the $N_{\mathrm{L}} \times 2N$ matrix $\mathbf{V}$, and set

$$\hat{\mathbf{u}} = \mathbf{Y}^{\mathrm{T}}\mathbf{u}. \tag{1.135}$$

Substitution for $\hat{\mathbf{u}}$ from Eq. (1.135) into Eq. (1.133b) gives

$$\mathbf{V}\,\mathbf{Y}^{\mathrm{T}}\mathbf{u} = \mathbf{0}, \tag{1.136}$$

which is identically satisfied for every $(2N - N_{\mathrm{L}})$-vector $\mathbf{u}$. Premultiplying both sides of Eq. (1.133a) by $\mathbf{Y}$, and substituting from Eq. (1.135) we obtain the following reduced system of $(2N - N_{\mathrm{L}})$ nonlinear ordinary differential equations for $\mathbf{u}$:

$$\bar{\mathbf{M}}\,\ddot{\mathbf{u}} + \bar{\mathbf{K}}\left(\mathbf{u}\right)\,\mathbf{u} + \bar{\mathbf{G}}\left(\lambda, \mathbf{u}\right) = \mathbf{0}, \tag{1.137}$$

where

$$\bar{\mathbf{M}} = \mathbf{Y}\mathbf{M}\mathbf{Y}^{\mathrm{T}}, \quad \bar{\mathbf{K}}\left(\mathbf{u}\right) = \mathbf{Y}\mathbf{K}\left(\mathbf{Y}^{\mathrm{T}}\mathbf{u}\right)\mathbf{Y}^{\mathrm{T}}, \quad \bar{\mathbf{G}}\left(\lambda, \mathbf{u}\right) = \mathbf{Y}\,\mathbf{G}\left(\lambda, \mathbf{Y}^{\mathrm{T}}\mathbf{u}\right). \tag{1.138}$$

Having found $\mathbf{u}$ from Eq. (1.137), $\hat{\mathbf{u}}$ is computed from Eq. (1.135).

1.4.5.2 DIPIE algorithm

We use the Displacement Pull-In Extraction (DIPIE) algorithm proposed by Bochobza-Degani et al. (2002) to solve Eq. (1.137) with the inertia term neglected, and find the complete bifurcation path. The applied voltage is treated as an additional unknown, and the deflection of a pre-chosen point $\bar{x}$ along the beam axis is used as the driving parameter s for the iteration scheme, so that both $\mathbf{u}$ and λ are regarded as functions of s. In this

way, the original problem, which has both stable and unstable equilibrium states, is replaced by a sequence of equivalent problems for which the equilibrium solution is always stable (Bochobza-Degani et al. (2002)).

If the solution $(\mathbf{u}_{k-1}, \lambda_{k-1})$ corresponding to $u_k^h(\bar{x}) = s_k$ is known, the solution $(\mathbf{u}_k, \lambda_k) = (\mathbf{u}_{k-1} + \Delta\mathbf{u}_k, \lambda_{k-1} + \Delta\lambda_k)$ at $s_k = s_{k-1} + \Delta s_k$ is found by solving the system of equations:

$$\begin{aligned} \bar{\mathbf{K}}(\mathbf{u}_k)\mathbf{u}_k + \bar{\mathbf{G}}(\lambda_k, \mathbf{u}_k) &= \mathbf{0}, && (1.139a) \\ \boldsymbol{\psi}(\bar{x})^{\mathrm{T}}\mathbf{Y}^{\mathrm{T}}\mathbf{u}_k &= \boldsymbol{\psi}(\bar{x})^{\mathrm{T}}\mathbf{Y}^{\mathrm{T}}\mathbf{u}_{k-1} + \Delta s_k. && (1.139b) \end{aligned}$$

The solution of the set of nonlinear Eqs. (1.139), in terms of the unknowns $\Delta\mathbf{u}_k$ and $\Delta\lambda_k$, is found by using Newton's iterations. Hence at the generic ν-th iteration

$$\begin{bmatrix} \bar{\mathbf{T}}_k^{(\nu)}\left(\lambda_k^{(\nu)}, \mathbf{u}_k^{(\nu)}\right) & \bar{\mathbf{H}}\left(\lambda_k^{(\nu)}, \mathbf{u}_k^{(\nu)}\right) \\ \boldsymbol{\psi}(\bar{x})^{\mathrm{T}}\mathbf{Y}^{\mathrm{T}} & 0 \end{bmatrix} \begin{bmatrix} \Delta\mathbf{u}_k^{(\nu)} \\ \Delta\lambda_k^{(\nu)} \end{bmatrix} = - \begin{bmatrix} \bar{\mathbf{K}}\left(\mathbf{u}_k^{(\nu)}\right)\mathbf{u}_k^{(\nu)} + \bar{\mathbf{G}}\left(\lambda_k^{(\nu)}, \mathbf{u}_k^{(\nu)}\right) \\ \boldsymbol{\psi}(\bar{x})^{\mathrm{T}}\mathbf{Y}^{\mathrm{T}}\mathbf{u}_k^{(\nu)} - \Delta s_k \end{bmatrix}, \tag{1.140}$$

where $\left(\Delta\mathbf{u}_k^{(\nu)}, \Delta\lambda_k^{(\nu)}\right)$ indicates the ν-th solution increment; $\left(\mathbf{u}_k^{(\nu)}, \lambda_k^{(\nu)}\right)$ is the updated solution at the $(\nu-1)$-th iteration, i.e.,

$$\mathbf{u}_k^{(\nu)} = \mathbf{u}_{k-1} + \sum_{h=1}^{\nu-1} \Delta\mathbf{u}_k^{(h)}, \quad \lambda_k^{(\nu)} = \lambda_{k-1} + \sum_{h=1}^{\nu-1} \Delta\lambda_k^{(h)}, \tag{1.141}$$

$\mathbf{T}_k^{(\nu)}\left(\lambda_k^{(\nu)}, \mathbf{u}_k^{(\nu)}\right)$ is the tangent stiffness at the $(\nu-1)$-th iteration, i.e.,

$$\begin{aligned} \mathbf{T}_k^{(\nu)}\left(\lambda_k^{(\nu)}, \mathbf{u}_k^{(\nu)}\right) &= \int_0^1 \boldsymbol{\psi}''(x)\boldsymbol{\psi}''(x)^{\mathrm{T}}\mathrm{d}x \\ &\quad + 2\mathfrak{N}_1 \int_0^1 \left(\boldsymbol{\psi}'(x)^{\mathrm{T}}\mathbf{Y}^{\mathrm{T}}\mathbf{u}_k^{(\nu)}\right)\boldsymbol{\psi}'(x)\mathrm{d}x \int_0^1 \boldsymbol{\psi}'(x)^{\mathrm{T}}\left(\boldsymbol{\psi}'(x)^{\mathrm{T}}\mathbf{Y}^{\mathrm{T}}\mathbf{u}_k^{(\nu)}\right)\mathrm{d}x \\ &\quad + \mathbf{Y}\left[\mathbf{D}_k^{(\nu)}\left(\lambda_k^{(\nu)}, \mathbf{u}_k^{(\nu)}\right)\right]\mathbf{Y}^{\mathrm{T}}, \end{aligned} \tag{1.142}$$

with

$$\mathbf{D}_k^{(\nu)}\left(\lambda_k^{(\nu)}, \mathbf{u}_k^{(\nu)}\right) = -\int_0^1 \frac{\partial F_{\mathrm{e}}}{\partial u^h}\left(\lambda_k^{(\nu)}, \boldsymbol{\psi}(x)^{\mathrm{T}}\mathbf{Y}^{\mathrm{T}}\mathbf{u}_k^{(\nu)}\right)\boldsymbol{\psi}(x)\boldsymbol{\psi}(x)^{\mathrm{T}}\mathrm{d}x, \tag{1.143}$$

and

$$\bar{\mathbf{H}}\left(\lambda_k^{(\nu)}, \mathbf{u}_k^{(\nu)}\right) = -\int_0^1 \frac{\partial F_{\mathrm{e}}}{\partial \lambda}\left(\lambda_k^{(\nu)}, \boldsymbol{\psi}(x)^{\mathrm{T}}\mathbf{Y}^{\mathrm{T}}\mathbf{u}_k^{(\nu)}\right)\boldsymbol{\psi}(x)\mathrm{d}x. \tag{1.144}$$

The iterations are performed until the infinity norm of the incremental solution, i.e., its maximum value over the beam span satisfies

$$\sup_{x\in(0,1)}\left[\boldsymbol{\psi}(x)^{\mathrm{T}}\mathbf{Y}^{\mathrm{T}}\Delta\mathbf{u}_k^{(\nu)}\right] \leq \varepsilon_{\mathrm{T}}, \tag{1.145}$$

where

$$\varepsilon_{\mathrm{T}} = \varepsilon_{\mathrm{A}} + \varepsilon_{\mathrm{R}} \sup_{x\in(0,1)} \left[\boldsymbol{\psi}(x)^{\mathrm{T}}\mathbf{Y}^{\mathrm{T}}\Delta\mathbf{u}_k^{(1)}\right], \tag{1.146}$$

ε^{A} and ε^{R} are preassigned small numbers. For a clamped-clamped microbeam we choose $\bar{x}$ equal to the mid-span, and for a cantilever microbeam we take $\bar{x}$ equal to the beam length. In order to extract the pull-in parameters we monitor the electrostatic parameter $\Delta\lambda_k$, since pull-in occurs when this parameter changes sign. We use a constant step Δs for iterating the deflection and if necessary, additional iterations are performed for pull-in parameters.

For every converged solution $(\lambda_k, \mathbf{u}_k)$ up to pull-in, the numerical natural frequencies of the beam are obtained by linearizing the nonlinear semidiscrete system of Eqs. (1.137) around the deformed state $(\lambda_k, \mathbf{u}_k)$, by discarding the applied load, and by seeking a solution of the type

$$\mathbf{u}_k(t) = \underline{\mathbf{u}}\exp(\mathbb{i}\omega t), \tag{1.147}$$

where $\mathbb{i} = \sqrt{-1}$. Therefore, the following eigenvalue problem arises:

$$\left[\bar{\mathbf{T}}_k\left(\lambda_k, \mathbf{u}_k\right) - \omega^2\bar{\mathbf{M}}\right]\underline{\mathbf{u}} = \mathbf{0}, \tag{1.148}$$

where $\bar{\mathbf{T}}_k$ is the tangent stiffness matrix defined in Eq. (1.142), and $\bar{\mathbf{M}}$ is the reduced mass matrix defined in Eq. (1.134a). Since the tangent stiffness matrix becomes singular at pull-in (see, e.g., Doedel et al. (1991*a*)), it follows that corresponding to pull-in at least one natural frequency of the system equals zero. The situation is analogous to that encountered in studying the buckling of a beam. The axial load at buckling can be found by determining natural frequencies of the deformed beam. The buckling load equals the axial load at which the fundamental frequency of the deformed beam vanishes.

1.4.6 Results and comparisons

1.4.6.1 Pull-in extraction

In Osterberg & Senturia (1997) the mid-plane stretching and the fringing field capacitance due to the finite thickness of the beam are neglected, and the Palmer approximate formula (1.118) is used. Therefore, expressions of the dimensionless axial load and of the dimensionless force per unit length are:

$$\mathfrak{N} = \begin{cases} \mathfrak{N}_0, & \text{clamped-clamped} \\ 0, & \text{cantilever} \end{cases}, \tag{1.149}$$

$$F_{\mathrm{e}} = \frac{\lambda}{(1-u)^2}\left(1 + \frac{2}{\pi}\frac{\beta}{\eta}\right). \tag{1.150}$$

In Abdel-Rahman et al. (2002) the mid-plane stretching is considered but all fringing field effects are neglected. Consequently, the electric force per unit length is given by

$$F_{\mathrm{e}} = \frac{\lambda}{(1-u)^2}. \tag{1.151}$$

In Kuang & Chen (2004) the mid-plane stretching is accounted for and the fringing field effects are treated as in Osterberg & Senturia (1997), i.e. by Eq. (1.150). The key features of the different models are summarized in Table 1.9.

Table 1.9: Key features of the considered electromechanical models.

Investigators	Membrane stretching	Capacitance approximation
Abdel-Rahman et al. (2002)	Yes	Parallel Plate
Kuang & Chen (2004)	Yes	Palmer's
Osterberg & Senturia (1997)	No	Palmer's
Present Work	Yes	Eq. (1.116)

Here we compare predictions of the models developed by Osterberg & Senturia (1997), Abdel-Rahman et al. (2002), and Kuang & Chen (2004) with those of the present work for two sample problems: a cantilever and a clamped-clamped microbeam. Both geometries have been analyzed in Pamidighantam et al. (2002) by using the FE software COVENTORWARE. For the problem analyzed in Pamidighantam et al. (2002) the microbeam deflections are relatively small and the nonlinear stiffening effect insignificant. In addition, the numerical findings of Pamidighantam et al. (2002) do not include the pull-in deflection which is a crucial design parameter.

Results from the 1-D distributed model (Eq. (1.137) with $\ddot{\mathbf{u}} = \mathbf{0}$) solved with the FE and the MLPG methods, and from the 1 d.o.f. model described in Sec. 1.4.4 are compared with those from the 3-D FE simulations using ANSYS. Details of the performance of simulating MEMS problems with ANSYS are given in Shapoorabadi & Kirk (2004). Following those guidelines on the accuracy of different simulation options, we used the tool ROM 144. We adapted to a narrow microbeam the "Sample Miniature Clamped-Clamped Beam Analysis", Ex. 6.6 in ANSYS (2003), by extending the surrounding dielectric in order to accurately account for the fringing fields. Geometric nonlinearities are included in the 3-D FE analysis. The region analyzed and its discretization into FEs are shown in Fig. 1.31 for the clamped-clamped microbeam; only one-half of the system is modeled due to symmetry conditions and a refined mesh is employed in the gap region. In particular, the dielectric medium is considered as a block of length 100μm, and thickness 24μm. For the cantilever microbeam problem, the dielectric domain has also been increased along the beam axis by 24μm in order to simulate fringing fields at the microbeam free end. The elements SOLID 45 (8 nodes brick elements) were used to model the microbeam, while SOLID 122 (20 nodes tetrahedral

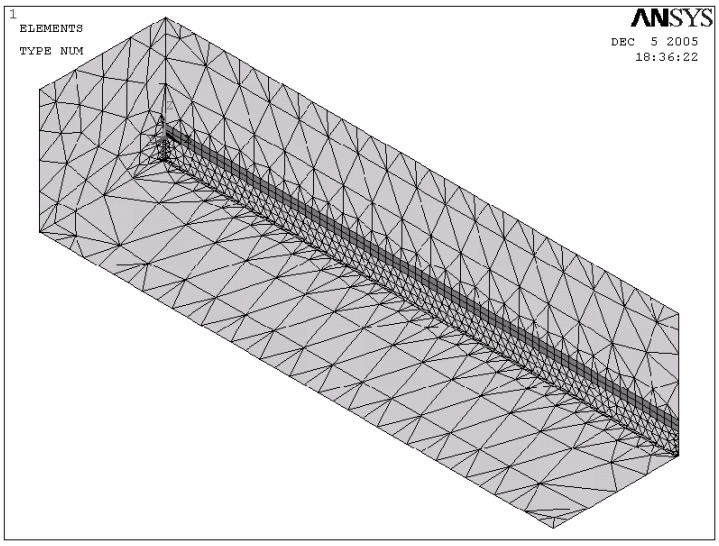

Figure 1.31: Schematics of the 3-D FE mesh used for ANSYS simulations of the clamped-clamped beam. The domain in light grey is the dielectric, and the one in dark grey is the microbeam.

elements) were used to model the dielectric. Table 1.10 lists the geometry and the material properties of the problems studied. The adopted mesh densities and the dielectric region dimensions correspond to the minimum required to obtain a fully converged solution for the pull-in parameters. Indeed, performing numerical experiments by varying both the dielectric region and the mesh density for the beam and the dielectric, we established that the third significant digit of the pull-in voltage and the pull-in deflection does not change either by considering a more refined mesh or a larger dielectric domain than the ones considered here.

A uniform grid of 9 nodes has been used for both the MLPG and the FE methods, and results were found practically indistinguishable from those obtained by considering more

Table 1.10: Geometric and material parameters for the problems studied. For the cantilever beam problem, case (1) refers to the geometry analyzed herein with ANSYS, while case (2) to the problem analyzed in Pamidighantam et al. (2002).

	Clamped-Clamped	Cantilever: case (1)	Cantilever: case (2)
ℓ, [μm]	100	100	300
b, [μm]	1	1	0.5
h, [μm]	2	2	1
g_0, [μm]	4	4	2.5
ϱ, $[\mathrm{kg/m^3}]$	2329	2329	-
E, [GPa]	169	169	77
ν	0.066	0.066	0.33
ϵ_r	1	1	1

refined grids. Numerical integrations have been performed by using 10 Gauss quadrature points located in each element for the FE method and in each subinterval partitioning the entire domain (Atluri et al. (1999)) for the MLPG method. The GMLS basis functions are generated by complete monomials of degree 3 ($m = 4$), see Eq. (A.2) in Appendix A.2. The radius R of the weight functions in Eq. (A.36) for the GMLS approximation is 5 times the distance between two adjacent nodes. The power α in Eq. (A.36) is set equal to 5, see Atluri et al. (1999) for a discussion of the effect of α on the trial function's degree of smoothness. The tuning of parameters for the MLPG analysis stems from the analysis of Andreaus, Batra & Porfiri (2005), where different parameters are analyzed and general guidelines given. As a rule of thumb, increasing any of the parameters α, R and m results in a more accurate solution but with more computational time. In the DIPIE algorithm for the clamped-clamped microbeam, the increment of the driving parameter Δs_k equals 2.5×10^{-3}, while for the cantilever microbeam the increments of the driving parameter are 4.0×10^{-3} for case (1), and 1.0×10^{-2} for case (2) in Table 1.10. These choices are motivated by the need to estimate the third significant digit in the dimensional pull-in maximum deflection. The tolerances in Newton's iterations for the DIPIE algorithm are $\varepsilon^{\mathrm{A}} = 10^{-6}$ and $\varepsilon^{\mathrm{R}} = 10^{-4}$, see Eq. (1.146).

Table 1.11: Comparison of the pull-in voltages, V_{PI}, and of the pull-in deflection's infinity norm, $\|u_{\mathrm{PI}}\|_{\infty}$, for the clamped-clamped microbeam obtained from different models, with different methods, and with the initial stress, (a) $\sigma_0 = 100$MPa, and (b) $\sigma_0 = 0$. The MLPG and the FE refer to solutions of the 1-D boundary-value problem with the MLPG and the FE methods respectively.

(a) $\sigma_0 = 100$MPa

	V_{PI}, [V]			$\|u_{\mathrm{PI}}\|_{\infty}$, [$\mu$m]		
ANSYS	902			2.47		
	1 d.o.f.	MLPG	FE	1 d.o.f	MLPG	FE
Abdel-Rahman et al. (2002)	1513	1510	1510	2.13	2.11	2.11
Kuang & Chen (2004)	1003	999	1000	2.55	2.53	2.53
Osterberg & Senturia (1997)	783	783	783	1.96	1.96	1.96
Present Work	938	934	935	2.47	2.46	2.46

(b) $\sigma_0 = 0$MPa

	V_{PI}, [V]			$\|u_{\mathrm{PI}}\|_{\infty}$, [$\mu$m]		
ANSYS	830			2.57		
	1 d.o.f.	MLPG	FE	1 d.o.f	MLPG	FE
Abdel-Rahman et al. (2002)	1373	1371	1371	2.24	2.23	2.24
Kuang & Chen (2004)	923	920	920	2.63	2.62	2.62
Osterberg & Senturia (1997)	663	660	660	1.96	1.96	1.96
Present Work	861	859	859	2.57	2.56	2.56

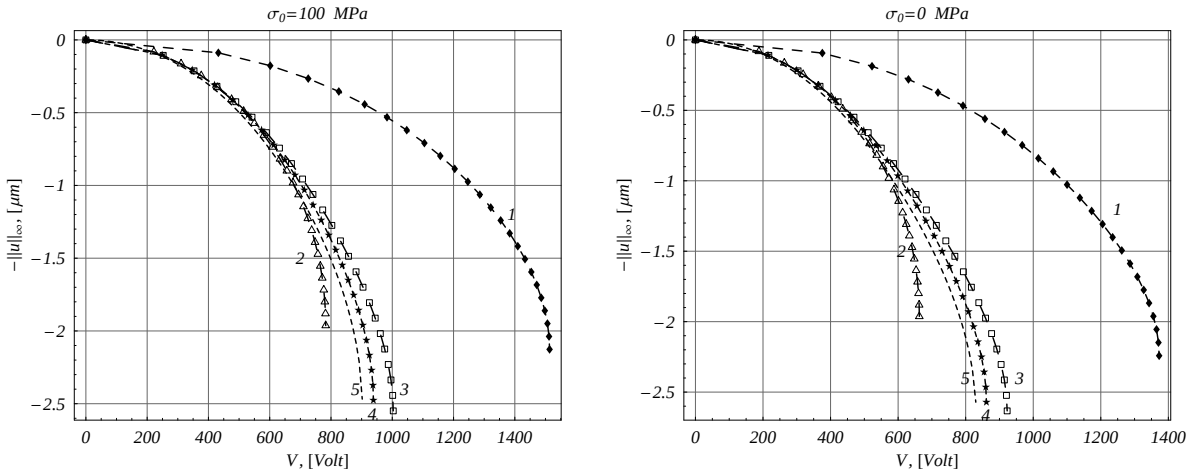

(a) (b)

Figure 1.32: Plots of the maximum displacement versus the applied voltage for the clamped-clamped microbeam problem under different initial states of stress. Results from all models are reported up to their predicted pull-in instability. (a) $\sigma_0 = 100$MPa; (b) $\sigma_0 = 0$MPa. Curves 1, 2, 3, and 4 refer to models in Abdel-Rahman et al. (2002), Osterberg & Senturia (1997), Kuang & Chen (2004), and the present work, respectively. Curve 5 is from 3-D FE simulations with ANSYS.

Results of different computations on the clamped-clamped microbeam are given in Table 1.11; results of ANSYS FE simulations are considered to be most reliable since they do not involve a-priori assumptions on the mechanical and the electrical behaviors of the system. Two different values of the initial stress σ_0, representative of pretensioned, and stress-free beams, have been examined. The accuracy of the proposed 1 d.o.f. model explained in Sec. 1.4.4 can be ascertained by comparing predictions from it with those from the MLPG and the FE methods. The complete neglect of the fringing field effects leads to significant underestimation of the electrostatic force and consequent overestimation of the pull-in voltage and underestimation of the pull-in deflection as is evident from the results computed by Abdel-Rahman et al. (2002). By introducing into the analysis of Abdel-Rahman et al. (2002) the fringing field correction (1.118), as is done in Kuang & Chen (2004), the pull-in voltage and the pull-in deflection are significantly improved; nevertheless, the pull-in voltage is still overestimated due to the neglect of the finite thickness of the beam in the computation of the electrostatic force. Instead, the pull-in deflection computed by Kuang & Chen (2004) is in good agreement with the ANSYS FE solution. The removal of the mid-plane stretching effect (Osterberg & Senturia (1997)) for the clamped-clamped beam significantly decreases the accuracy of the pull-in deflection, since it completely ignores the nonlinear stiffening which for the present geometry ($g_0/h = 2$) is extremely relevant. The work of Osterberg & Senturia (1997) is based on assuming small deflections of the microbeam, and therefore it is incapable of accurately estimating pull-in parameters for the present geometry. The pull-in voltage is instead underestimated, since by neglecting the membrane stretching, the overall

mechanical compliance is overestimated. As is evident from the results listed in Table 1.11, the present work, by properly accounting for the fringing field effects due to the beam finite thickness, provides a consistent electromechanical theory that gives accurate results for narrow clamped-clamped microbeams undergoing severe displacements.

Fig. 1.32 reports the voltage versus the maximum deflection for the two considered values of the initial stress obtained using the effects considered by the four groups of investigators listed in Table 1.9. The curves are computed by using the simple 1 d.o.f. model explained in Sec. 1.4.4. For increasing voltages, the maximum deflections predicted by these four analyses significantly differ; the response predicted by the present work is closest to that given by ANSYS.

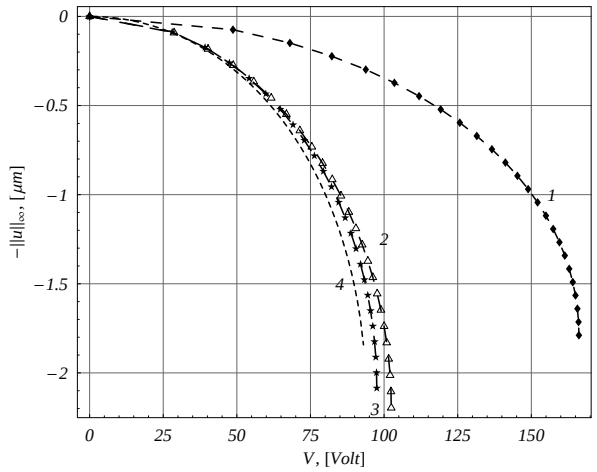

Figure 1.33: Plots of the maximum displacement versus the applied voltage for the cantilever microbeam identified as case (1) in Table 1.10. Curves 1, 2, and 3, refer to models in Abdel-Rahman et al. (2002), Osterberg & Senturia (1997) and Kuang & Chen (2004), and the present work, respectively. Curve 4 is from 3-D FE simulations with ANSYS.

Results of computations on the two sample cantilever microbeams whose parameters are listed in Table 1.10 are given in Table 1.12. The discrepancy between the pull-in voltage predicted by Abdel-Rahman et al. (2002) and the ones resulting from either ANSYS or COVENTORWARE (Pamidighantam et al. 2002) signifies the importance of fringing fields for a reliable understanding of the pull-in instability in a narrow microbeam. When compared to the works of Osterberg & Senturia (1997) and Kuang & Chen (2004) the present investigation improves both the estimates of the pull-in voltage and the pull-in deflection. Indeed, the analyses of Osterberg & Senturia (1997) and Kuang & Chen (2004) underestimate the electrostatic force by neglecting the fringing field effects due to the beam finite thickness and therefore overestimate the pull-in voltage, and lead to less accurate estimates of the pull-in deflection. For assumptions made by the four groups of researchers, and the 3-D FE analysis Fig. 1.33 reports the voltage versus the maximum deflection for the geome-

Table 1.12: Comparison of pull-in voltages and pull-in maximum deflections of the cantilever microbeam obtained from different models, and with different methods. The MLPG and the FE refer to solutions of the 1-D boundary-value problem with the MLPG and the FE methods respectively.

(a) Beam (1) of Table 1.10

	V_{PI}, [V]			$\|u_{\mathrm{PI}}\|_{\infty}$, [$\mu$m]		
ANSYS	93			1.84		
	1 d.o.f.	MLPG	FE	1 d.o.f	MLPG	FE
Abdel-Rahman et al. (2002)	166	165	165	1.79	1.79	1.79
Osterberg & Senturia (1997), Kuang & Chen (2004)	102	102	102	2.20	2.19	2.20
Present Work	98	97	97	2.08	2.08	2.08

(b) Beam (2) of Table 1.10

	V_{PI}, [V]			$\|u_{\mathrm{PI}}\|_{\infty}$, [$\mu$m]		
COVENTORWARE	1.2			(not available)		
	1 d.o.f.	MLPG	FE	1 d.o.f	MLPG	FE
Abdel-Rahman et al. (2002)	2.18	2.17	2.17	1.12	1.12	1.12
Osterberg & Senturia (1997), Kuang & Chen (2004)	1.25	1.25	1.25	1.40	1.40	1.40
Present Work	1.21	1.21	1.21	1.30	1.30	1.30

try identified as case (1) in Table 1.10. The curves are computed by using the 1 d.o.f. model presented in Sec. 1.4.4. As for the clamped-clamped microbeam, the complete neglect of fringing fields yields severely erroneous predictions. Accounting for fringing fields in narrow cantilever microbeams dramatically increases the accuracy and a detailed accounting of fringing field effects, as has been done in the present work, gives results with relatively low errors.

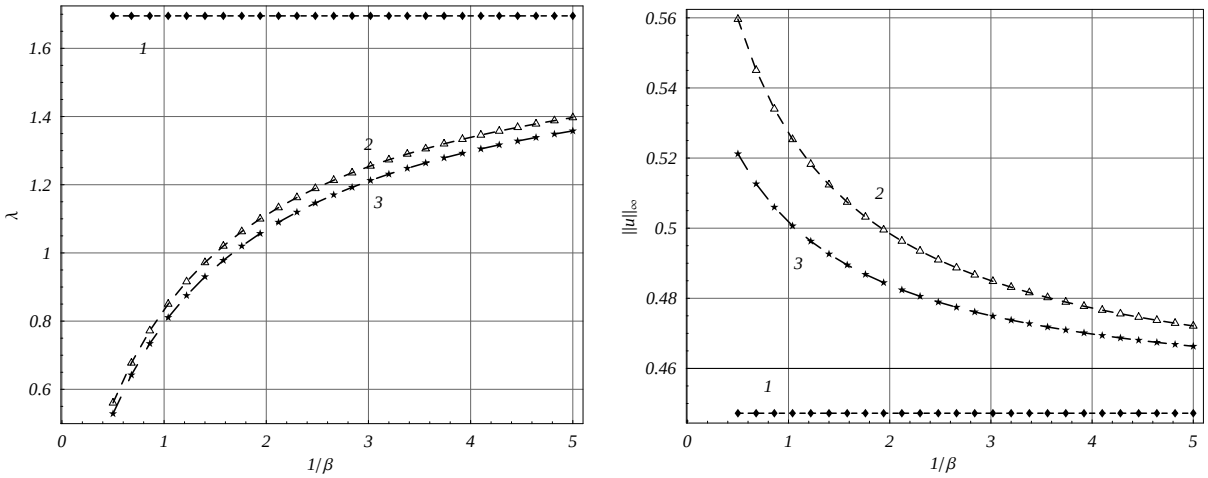

(a) (b)

Figure 1.34: For the cantilever beam identified as case (2) in Table 1.10, comparison of (a) the nondimensional pull-in voltage λ vs. $1/\beta$, and (b) the maximum pull-in non-dimensional deflection $\|u\|_\infty$ vs. $1/\beta$, computed from the present 1 d.o.f. model (curve 3) with those from Osterberg & Senturia (1997) and Kuang & Chen (2004) (curve 2), and Abdel-Rahman et al. (2002) (curve 1).

The nondimensional pull-in parameter λ for different values of the beam width b and with values of other parameters listed in Table 1.10, computed with different MEMS models, is given in Figs. 1.34(a) and 1.35(a) for a cantilever and a clamped-clamped beam respectively; the corresponding results for the maximum pull-in deflections are exhibited in Figs. 1.34(b) and 1.35(b). The curves are computed by using the present 1 d.o.f. model. For each beam the nondimensional pull-in parameter λ increases monotonically with a decrease in the value of β from 2.0 to 0.2. From Figs. 1.34(b) and 1.35(b), it is clear that the nondimensional pull-in maximum deflection significantly changes with the width of the beam, and consistently differs from the values used in Pamidighantam et al. (2002) for deriving empirical estimates of the pull-in voltage (0.45 for the cantilever, and 0.40 for the clamped-clamped microbeams). Indeed, for the narrow microbeam with $\beta = 2$, the nondimensional pull-in maximum deflections are 0.56 and 0.66 for the cantilever and the clamped-clamped configurations, respectively.

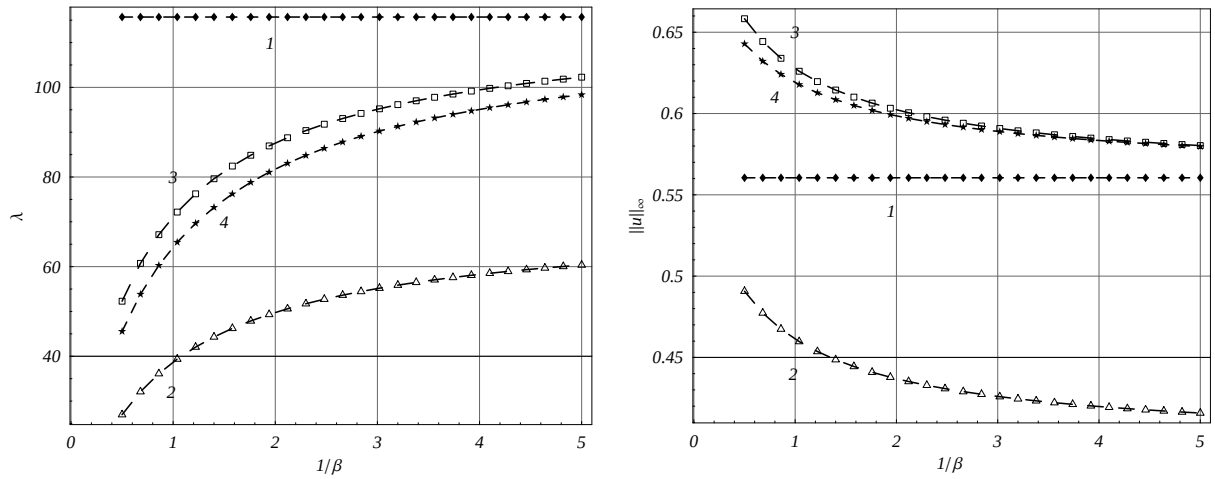

Figure 1.35: For the fixed-fixed beam with $\sigma_0 = 0$MPa, comparison of (a) the nondimensional pull-in voltage λ vs. $1/\beta$, and (b) the maximum pull-in non-dimensional deflection $\|u\|_\infty$ vs. $1/\beta$, computed from the present 1 d.o.f. model (curve 4) with those from Abdel-Rahman et al. (2002) (curve 1), Osterberg & Senturia (1997) (curve 2), and Kuang & Chen (2004) (curve 3).

1.4.6.2 Modal analysis of the fixed-fixed microbeam predeformed by an electric field

We consider the clamped-clamped microbeam with material parameters listed in Table 1.10. The fundamental frequency of the predeformed system with applied voltage V spanning the range $[0, V_{\rm PI})$ has been computed by using the 1 d.o.f. model explained in Sec. 1.4.4, and by solving the continuous 1-D electromechanical model defined by Eq. (1.111) with both the FE and the MLPG methods as explained in Sec. 1.4.5.2. Values of parameters for MLPG and FE methods are the same as those used for pull-in extraction problem studied in Sec. 1.4.6.1. Comparisons are made with results obtained with ANSYS. For 3-D FE simulations, the fundamental natural frequency of the system is obtained by first solving a static problem to determine the deformed shape of the clamped-clamped narrow microbeam under a given applied voltage. Subsequently, harmonic analysis is performed by exciting the deflected/prestressed beam via a small harmonic voltage, and computing the amplitude of oscillations at the beam mid span for different excitation frequencies. Applied frequencies are incremented by 5KHz. Geometric nonlinearities are included in the 3-D FE analysis.

As before, results from the proposed electromechanical model for narrow microbeams are compared with those presented in Abdel-Rahman et al. (2002), Kuang & Chen (2004), and Osterberg & Senturia (1997). The key assumptions in these analyses are summarized in Table 1.9.

In Tables 1.13 and 1.14 we compare results for two values of the initial stress σ_0 with the

Table 1.13: Comparison of the fundamental frequency of the microbeam with no voltage applied computed from the 1 d.o.f. model (Eq. (1.126)), and the FE and the MLPG methods, with that computed using ANSYS.

σ_0, [MPa]	$\omega(0)/2\pi$, [MHz]			
	ANSYS	1 d.o.f.	MLPG	FE
100	2.075	2.075	2.075	2.075
0	1.750	1.757	1.751	1.751

3-D FE findings. Comparison parameters in Table 1.14 are the maximum frequency $\omega_{\max}$ attained for V spanning the interval $[0, V_{\rm PI})$, and the voltage $V_{\omega_{\max}}$ corresponding to $\omega_{\max}$.

Table 1.14: Comparison of representative parameters found using different electromechanical models and different solution techniques, and the 3-D FE simulations.

(a) $\sigma_0 = 100$MPa

	$\omega_{\max}/2\pi$, [MHz]			$V_{\omega_{\max}}$, [V]		
ANSYS	2.075			0		
	1 d.o.f.	MLPG	FE	1 d.o.f	MLPG	FE
Abdel-Rahman et al. (2002)	2.075	2.075	2.075	0	0	0
Kuang & Chen (2004)	2.139	2.121	2.121	874	862	862
Osterberg & Senturia (1997)	2.075	2.075	2.075	0	0	0
Present Work	2.075	2.075	2.075	0	0	0

(b) $\sigma_0 = 0$MPa

	$\omega_{\max}/2\pi$, [MHz]			$V_{\omega_{\max}}$, [V]		
ANSYS	1.920			725		
	1 d.o.f.	MLPG	FE	1 d.o.f	MLPG	FE
Abdel-Rahman et al. (2002)	1.757	1.751	1.751	0	0	0
Kuang & Chen (2004)	2.061	2.046	2.044	817	816	816
Osterberg & Senturia (1997)	1.757	1.751	1.751	0	0	0
Present Work	1.946	1.935	1.936	772	761	761

It is clear from the results reported in Table 1.13 that the fundamental frequency of the microbeam computed from Eq. (1.126) with $\bar{\lambda} = 0$, and from the FE and the MLPG methods agrees very well with that computed by using ANSYS. In Fig. 1.36 we plot the variation of the fundamental frequency $\omega(V)$ normalized with respect to the fundamental frequency $\omega(0)$ of the undeflected microbeam, versus the applied voltage V in the range $[0, V_{\rm PI})$, normalized with respect to the pull-in voltage $V_{\rm PI}$. Each curve is normalized with respect to the corresponding parameters listed in Tables 1.11 and 1.13. In Fig. 1.36(b), $\omega_{\max}/\omega(0)$ and $V_{\omega_{\max}}/V_{\rm PI}$ for the model of Kuang & Chen (2004) are depicted, where $V_{\rm PI}$ is the pull-in

voltage predicted by the corresponding model, and reported in Table 1.11.

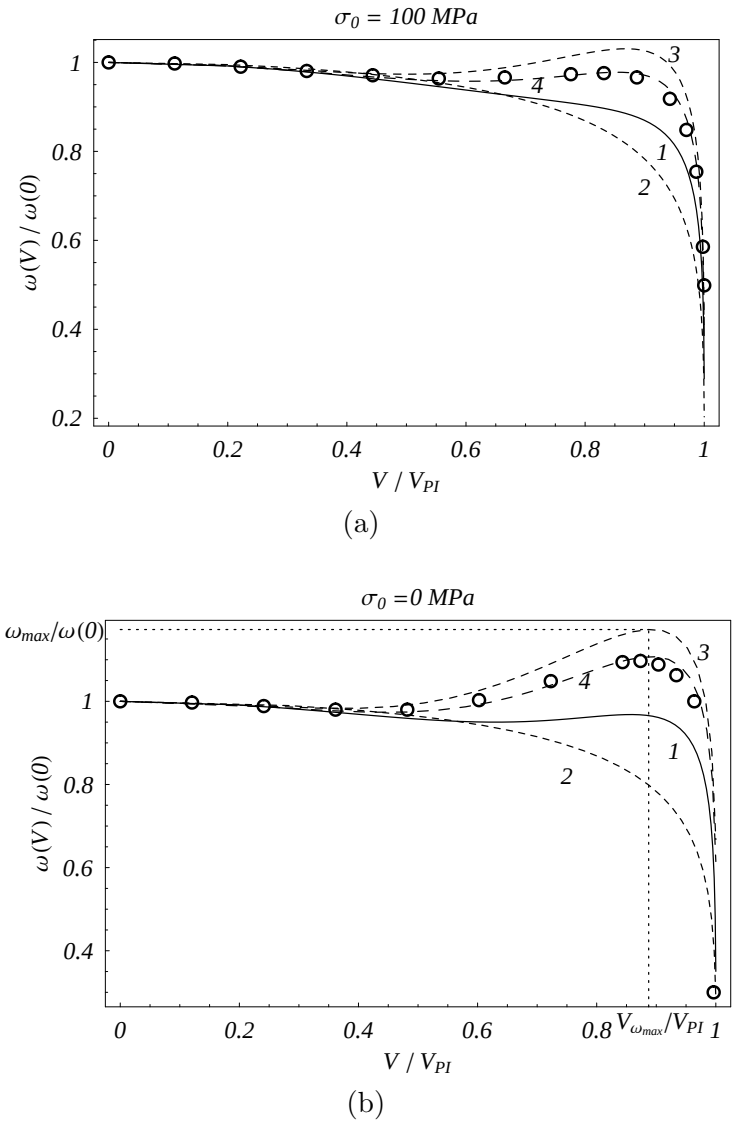

(a)

(b)

Figure 1.36: Variation of the fundamental frequency with applied dc voltage computed with ANSYS (open circles), and the models used in Abdel-Rahman et al.(2002) (curve 1), Osterberg & Senturia (1997) (curve 2), Kuang & Chen (2004) (curve 3), and in the present work (curve 4). (a) $\sigma_0 =$ 100MPa, (b) $\sigma_0 = 0$MPa.

Results listed in Table 1.14 and those plotted in Fig. 1.36 show that for a narrow microbeam undergoing relatively large displacements, there are significant discrepancies between maximum frequencies computed with the assumption made in Abdel-Rahman et al. (2002), Osterberg & Senturia (1997), and Kuang & Chen (2004) and the 3-D FE solution. When completely discarding fringing field effects as in Abdel-Rahman et al. (2002), the electrostatic force is underestimated resulting in overestimation of the pull-in voltage and underestimation of the pull-in displacements as shown in Table 1.11. As a consequence the displacements ex-

perienced by the microbeam are smaller than the actual ones and the strain hardening due to membrane stretching is underestimated. Therefore, the membrane stretching is incapable of dominating the electrostatic softening for pretensioned microbeams as illustrated by results plotted in Fig. 1.36(a) where the frequency versus the voltage curve is monotonically decreasing. When fringing field effects due to the microbeam finite width are also considered as by Kuang & Chen (2004), the pull-in voltage and the pull-in maximum deflection are slightly overestimated, resulting in an overestimation of the strain hardening versus the electrostatic softening. The maximum value of the fundamental frequency is therefore overestimated and the voltage versus the frequency curve shows a relevant overshoot with respect to the FE solution. The model proposed by Osterberg & Senturia (1997) neglects the strain hardening effect and always gives monotonic behavior of the voltage versus the frequency response. The present electromechanical model based on the fringing fields correction (1.117) provides accurate quantitative predictions of the maximum frequency for narrow microbeams and is able to reliably capture the qualitative behavior of the lowest frequency versus the applied dc voltage.

1.5 Conclusions

We have implemented the pseudoarclength continuation method in the MLPG formulation of electrostatically actuated micromembranes. A local symmetric augmented weak formulation of the problem is derived wherein essential boundary conditions are enforced by a set of Lagrange multipliers. The MLS approximation is used to generate basis functions for the trial solution, and the test functions are taken to be the weight functions of the MLS approximation. The resulting set of nonlinear equations is solved by the Newton iteration method. The accuracy and the reliability of the proposed technique is assessed through comparisons of the presently computed results with those from other numerical methods.

It is shown that a reduced number of nodes (~ 160) and a few steps (~ 100) in the pseudoarclength continuation method are sufficient for estimating the pull-in parameters and the symmetry-breaking bifurcations with an error of at most 1.53%. The convergence rate of the pseudoarclength continuation method does not vanish when the pull-in state is approached; moreover, since the applied voltage is treated as unknown, the number of iterations remains bounded.

The effect of the scale on micromembranes has been studied by including the Casimir force in the mathematical model. The effect of the Casimir force on pull-in and symmetry breaking parameters has been investigated. It has been shown that in the miniaturization process there is a minimum scale for the device below which the system spontaneously collapses at zero applied voltage. We have given a closed form relation (Eq. (1.96)) based on a

simple lumped model that seems suitable for MEMS design. However, the description of the relationship between the device travel range and the device scale, and the symmetry breaking after pull-in instability necessitate the use of distributed models.

A consistent electromechanical model for narrow microbeams with width smaller than five times the thickness has been derived. A novel formula for estimating the line to ground capacitance, which takes into account the finite thickness and the aspect ratio of the beam's cross section has been obtained by least square fitting data from a fully converged solution computed with the method of moments. Values obtained from this relation are compared with those from other expressions in the literature, and predictions from its use are shown to be valid for a narrow microbeam.

A one degree-of-freedom model that gives very good values of the pull-in parameters and the fundamental frequency for narrow microbeams has been proposed. It differs from the classical spring-mass model since the nonlinear stiffening due to the axial stress, charge redistribution and fringing fields are taken into account. Moreover, the complete nonlinear behavior of the electrostatic force is retained and the pull-in voltage and deflections are treated as unknowns, i.e., the pull-in deflection is not empirically chosen as was done by Pamidighantam et al. (2002). It is shown that the pull-in deflections noticeably change with the aspect ratio of the beam cross-section, and can not be a-priori determined. The one degree-of-freedom model results have been validated by comparing them with those obtained by solving the nonlinear one-dimensional boundary-value and the corresponding eigenvalue problems with the MLPG, and the FE methods in conjunction with the DIPIE algorithm.

The computed pull-in parameters and the fundamental frequency are found to match well with that obtained from the solution of the 3-dimensional problem with the commercial computer code ANSYS. The 3-dimensional simulations are considerably more expensive than those for the proposed one-dimensional distributed model, and the one degree-of-freedom model.

Chapter 2

Adiabatic Shear Bands in Heat-Conducting Elastothermoviscoplastic Materials

2.1 Introduction

The term adiabatic shear is related to a localization phenomenon that occurs during high strain-rate plastic deformations such as machining, explosive forming, shock impact loading, ballistic penetration, fragmentation, ore crushing, impact tooling failure, and metal shaping and forming processes (see e.g. Batra (1987)). The shear strain localization problems in metals are generally characterized by the formation of a narrow region of intense plastic deformation called an adiabatic shear band (ASB). Even though heat conduction plays a significant role in determining the shear band width, it is called adiabatic since there is not enough time for the heat to be conducted away from the shear band. The shear strain localization has been observed in many materials such as steel, non-ferrous metals, and polymers. The study of the phenomenon is important because progressive shearing within an ASB provides an undesirable mode of material resistance to imposed deformations; moreover, the bands are often precursors of ductile fracture in many metals deformed at high strain rates.

The basic phenomenon of adiabatic shear banding is similar to that of the pull-in instability in MEMS studied in Chapter 1. In shear banding, heat produced within the region of localization softens the material which then deforms more rapidly generating additional heating. This self-feeding mechanism eventually ends when heating produced within an ASB is conducted out of it at the same rate as it is produced resulting in a steady width of the localized region or the ASB. The pull-in instability phenomenon in MEMS is also self-feeding in the sense that an applied voltage across the two conductors generates the

Coulomb between them, the deformable conductor then deflects which increases magnitudes of this force resulting in additional deflections of the conductor and eventual collapse of the MEMS. Whereas in shear banding, thermal softening of the material has to overcome its hardening due to strain and strain rate effects, in MEMS the additional force generated due to the decrease in the gap between the two conductors must be large enough to overcome hardening of the material due to its being stretched and bent.

Recently, considerable research in computational mechanics has been devoted to the development of meshless methods. An objective of a meshless method is to get rid of, or at least alleviate the difficulty of meshing the domain. Meshless methods may also alleviate some other problems associated with the Finite Element Method (FEM), such as locking and element distortion. In many applications, they also provide smooth and accurate approximate solutions with a reduced number of nodes.

During the last two decades, several meshless methods for seeking approximate solutions of partial differential equations have been proposed. These include the element-free Galerkin (EFG) (Belytschko, Lu & Gu (1994)), hp- clouds (Duarte & Oden (1996)), the reproducing kernel particle (RKPM) (Liu, Jun & Zhang (1995)), the diffuse element (Nayroles, Touzot & Villon (1992)), the partition of unity finite element (PUFEM) (Melenk & Babuska (1996)), the natural element (Sukumar, Moran & Belytschko (1998)), meshless Galerkin using radial basis functions (RBFs) (Wendland (1995)), the meshless local Petrov-Galerkin (MLPG) (Atluri & Zhu (1998), Atluri & Shen (2002)), the smoothed particles hydrodynamics (SPH) (Lucy (1977)), the modified smoothed particle hydrodynamics (MSPH) (Zhang & Batra (2004)), the meshless local boundary integral equation (LBIE) (Zhu, Zhang & Atluri (1998)), the collocation method using RBFs (Kansa (1990)). All of these methods, except for the last five use either shadow elements or a background mesh for evaluating integrals in the governing weak formulation of a problem.

The MLPG method has been successfully applied to several problems in mechanics: static linear plane elasticity (Atluri & Zhu (1998)); vibrations of elastic planar bodies (Gu & Liu (2001)); static analysis of beams (Atluri et al. (1999)); static and dynamic analysis of functionally graded materials (Qian, Batra & Chen (2004)); transient heat conduction in a bimaterial body (Batra, Porfiri & Spinello (2004)); wave propagation in bars with material interfaces (Batra, Porfiri & Spinello (2006*c*)) and in cracked beams (Andreaus et al. (2005)); static analysis of nonlinear electromechanical problems (Batra et al. (2006*b*)). To our knowledge it has not been applied to analyze a transient thermoviscoelastoplastic problem involving the localization of deformations into a narrow band.

The MLPG method is based on a local weak formulation of the governing equations and employs meshless interpolations for both the trial and the test functions. Bases for the

trial functions are usually constructed with the Moving Least Squares (MLS) approximation proposed by Lancaster & Salkauskas (1981). In the Petrov-Galerkin formulation, the test functions may be chosen from a different space than the space of trial functions. Thus several variations of the method may be obtained (see e.g. Atluri & Zhu (1998) for discussion). The key ingredients of the MLPG method may be summarized as: local weak formulation, MLS interpolation, Petrov-Galerkin projection, numerical evaluation of domain integrals, and computation of desired quantities at critical points.

Here we analyze simple shearing deformations of a block made of an elasto-thermo-viscoplastic material with the MLPG6 method, i.e. the local Bubnov-Galerkin formulation, and show that it captures well the localization of deformation and the emanation of an elastic unloading wave from the shear banded region. In the constitutive relation for the material, strain and strain-rate hardening, and thermal softening are considered. The problem is studied by introducing a Local Symmetric Nonlinear Augmented Weak Form (LSNAWF) of coupled nonlinear governing equations with the non-homogeneous essential boundary conditions. The prescribed velocity on the top and the bottom surfaces of the block is enforced by a set of Lagrange multipliers. From the LSNAWF a semidiscrete formulation is derived, and the constraint related to the non-homogenous essential boundary conditions is treated by introducing a transformation matrix that eliminates the constrained degrees of freedom. Since nodal variables do not equal values of unknowns at the nodes, standard time integration packages like LSODE (see Radhakrishnan & Hindmarsh (1993)) can not be employed. Therefore, the resulting reduced system of coupled nonlinear ordinary differential equations is integrated in time by a one-step algorithm, which can be regarded both as the first order Adams-Moulton method and the first order backward difference method (see Gear (1971)). The convergence at each time step is reached by Newton's iterations. A good agreement between the computed results and the ones obtained with the FEM by Batra & Kim (1990) and with the MSPH method by Batra & Zhang (2004) is achieved. For materials exhibiting enhanced thermal softening, it has been found that the shear stress drops very rapidly in the localization region, and an elastic unloading shear wave emanates outward from it. The numerically computed wave speed matches well with the analytical one, and the width of the region of localization is close to that observed experimentally by Marchand & Duffy (1988) and to that obtained by the FE and the MSPH methods.

The rest of the Chapter is organized as follows. In Sec. 2.2 we formulate the initial-boundary-value problem to be studied by presenting the governing equations, and initial and boundary conditions. In Sec. 2.3 we present the MLPG formulation of the initial-boundary-value problem by briefly outlining the MLS approximation, introducing the LSNAWF, and obtaining from it the nonlinear semidiscrete formulation. In Sec. 2.4 we discuss the time integration scheme, and compare the numerical solution with those obtained from the FE and the

MSPH methods. Expressions for functions appearing in the domain integrals are reported in Appendix D.

Symbols used to denote various quantities in this Chapter are not necessarily the same as those employed in Chapter 1.

2.2 Formulation of the problem

We analyze simple shearing deformations of a block made of an elasto-thermo-viscoplastic material that lies between the planes $y = \pm H$ as depicted in Fig. 2.1. Only the x-component of velocity is taken to be non-zero. Equations governing deformations of the body are (Batra (1987), Batra & Kim (1990)):

$$\varrho\dot{v}\left(y,t\right) = s'\left(y,t\right), \tag{2.1a}$$

$$\varrho\dot{e}\left(y,t\right) = -q'\left(y,t\right) + s\left(y,t\right)v'\left(y,t\right), \tag{2.1b}$$

$$\dot{\gamma}\left(y,t\right) = v'\left(y,t\right), \tag{2.1c}$$

$$\dot{\gamma}\left(y,t\right) = \dot{\gamma}_{\mathrm{e}}\left(y,t\right) + \dot{\gamma}_{\mathrm{p}}\left(y,t\right), \tag{2.1d}$$

$$q\left(y,t\right) = -\kappa\,\vartheta'\left(y,t\right), \tag{2.1e}$$

$$\dot{s}\left(y,t\right) = \mu\dot{\gamma}_{\mathrm{e}}\left(y,t\right), \tag{2.1f}$$

$$\varrho\dot{e}\left(y,t\right) = \varrho c\dot{\vartheta}\left(y,t\right) + s\left(y,t\right)\dot{\gamma}_{\mathrm{e}}\left(y,t\right), \tag{2.1g}$$

$$\dot{\gamma}_{\mathrm{p}}\left(y,t\right) = \Lambda\left(y,t\right)s\left(y,t\right), \tag{2.1h}$$

$$k\left(y,t\right)\dot{\psi}\left(y,t\right) = s\left(y,t\right)\dot{\gamma}_{\mathrm{p}}\left(y,t\right), \qquad k\left(y,t\right) = k_0\left(1+\frac{\psi\left(y,t\right)}{\psi_0}\right)^n, \tag{2.1i}$$

$$\Lambda = \max\left\{0, \frac{1}{bs}\left(\left(\frac{s}{k_0(1-a\vartheta)\left(1+\frac{\psi}{\psi_0}\right)^n}\right)^{1/m} - 1\right)\right\}. \tag{2.1j}$$

Here, a superimposed dot indicates the material derivative with respect to time t, and the prime means derivative with respect to the space variable y. Furthermore, v is the x-component of velocity, s the shear stress, q the heat flux, γ the shear strain, γ_{e} and γ_{p} the elastic and the plastic parts of the shear strain respectively, e is the specific internal energy, ϑ the temperature rise, ψ an internal variable, ϱ the mass density, κ the thermal conductivity, c the specific heat, and μ the shear modulus. The parameter k describes the work hardening of the material, a is the thermal softening parameter, b and m are the strain-rate hardening parameters, ψ_0 and n are the work hardening parameters, and k_0 is the yield stress in a quasi-static isothermal simple shear test. The plastic multiplier Λ is zero when the deformation is elastic, and is positive for plastic deformations (see Batra (1987)).

Eq. (2.1a) is the balance of linear momentum, Eq. (2.1b) the balance of internal energy,

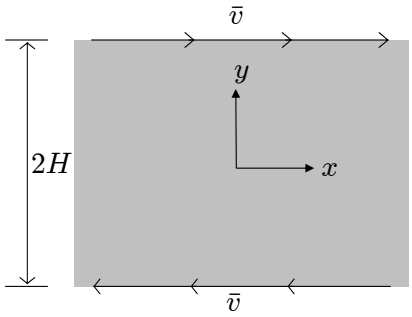

Figure 2.1: Geometry and kinematic boundary conditions of the problem.

Eq. (2.1c) the definition of the shear strain rate, while Eq. (2.1d) gives the additive decomposition of the total shear strain rate into elastic and plastic parts. Eq. (2.1e) is Fourier's law of heat conduction, Eqs. (2.1f) and (2.1g) are constitutive relations, and Eq. (2.1h) is the flow rule with the plastic multiplier Λ given by Eq. (2.1j). Eq. (2.1i) describes the work hardening of the material due to plastic deformations. The yield surface is assumed to be given by

$$s = k_0 \left(1 - a\vartheta\right) \left(1 + \frac{\psi}{\psi_0}\right)^n \left(1 + b\dot{\gamma}_{\mathrm{p}}\right)^m , \tag{2.2}$$

whose radius increases due to strain- and strain-rate hardening, and decreases due to thermal softening.

We introduce the following nondimensional variables:

$$\begin{aligned}
y &= H\bar{y}, \quad \gamma = \bar{\gamma}, \quad \psi = \bar{\psi}, \quad v = H\dot{\gamma}_0\bar{v}, \quad t = \frac{\bar{t}}{\dot{\gamma}_0}, \\
s &= k_0\bar{s}, \quad k = k_0\bar{k}, \quad \Lambda = \frac{\dot{\gamma}_0}{k_0}\bar{\Lambda}, \quad b = \frac{\bar{b}}{\dot{\gamma}_0}, \quad \mu = k_0\bar{\mu}, \\
\vartheta &= \frac{k_0}{\varrho c}\bar{\vartheta}, \quad \varrho = \frac{k_0}{H^2\dot{\gamma}_0^2}\bar{\varrho}, \quad \kappa = \varrho c H^2\dot{\gamma}_0\bar{\kappa}, \quad a = \frac{\varrho c}{k_0}\bar{a},
\end{aligned} \tag{2.3}$$

where quantities with an overbar are nondimensional, and $\dot{\gamma}_0$ is the average shear strain rate. Substituting from Eqs. (2.3) into Eqs. (2.1), and dropping the overbars from nondimensional variables we get the following set of governing equations in nondimensional variables:

$$\varrho\dot{v} = s', \tag{2.4a}$$

$$\dot{\vartheta} = \kappa\vartheta'' + \Lambda s^2, \tag{2.4b}$$

$$\dot{s} = \mu\left(v' - \Lambda s\right), \tag{2.4c}$$

$$\dot{\psi} = \frac{\Lambda s^2}{\left(1+\frac{\psi}{\psi_0}\right)^n}, \tag{2.4d}$$

$$\Lambda = \max\left\{0, \frac{1}{bs}\left(\left(\frac{s}{(1-a\vartheta)\left(1+\frac{\psi}{\psi_0}\right)^n}\right)^{1/m} - 1\right)\right\}. \tag{2.4e}$$

Following Batra & Kim (1990), we assume that a homogeneous solution of Eqs. (2.4) under boundary conditions

$$v(-1,t) = -1, \qquad v(1,t) = 1, \tag{2.5a}$$

$$\vartheta'(\pm 1,t) = 0, \tag{2.5b}$$

and initial conditions

$$v(y,0) = y, \qquad \vartheta(y,0) = s(y,0) = \psi(y,0) = 0, \tag{2.6}$$

is perturbed when $\psi = 0.1$, $\vartheta = 0.1003$, and $\gamma = 0.0692$. We seek a solution of the resulting initial-boundary-value problem with boundary conditions (2.5) and initial conditions

$$v(y,0) = y, \tag{2.7a}$$

$$\vartheta(y,0) = 0.1003 + 0.1\left(1-y^2\right)^9 \exp\left(-5y^2\right), \tag{2.7b}$$

$$s(y,0) = \left(1+\frac{0.1}{\psi_0}\right)^n (1-a\vartheta(y,0))(1+b)^m, \tag{2.7c}$$

$$\psi(y,0) = 0.1. \tag{2.7d}$$

The second term on the right-hand side of Eq. (2.7b) represents a perturbation; its amplitude is chosen large enough to reduce the computational time required for deformations to localize at $y = 0$. The peak in the shear stress-shear strain curve occurs at $\gamma = 0.093$. Boundary condition (2.5b) implies that the surfaces $y = \pm 1$ are thermally insulated. Thus all of the heat generated due to plastic dissipation is used to raise the temperature of the body. The inhomogeneous initial conditions imply that the temperature rise within the body is nonuniform and is quite high within the ASB.

Because of boundary conditions (2.5) and initial conditions (2.7), we assume that the solution exhibits the following symmetries/antisymmetries:

$$v(-y,t) = -v(y,t), \tag{2.8a}$$

$$\vartheta(-y,t) = \vartheta(y,t), \tag{2.8b}$$

$$s(-y,t) = s(y,t), \tag{2.8c}$$

$$\psi(-y,t) = \psi(y,t). \tag{2.8d}$$

Therefore, we solve the problem in the domain $(0,1)$ with initial conditions (2.7) and the following boundary conditions

$$v(0,t) = 0, \qquad v(1,t) = 1, \tag{2.9a}$$

$$\vartheta'(0,t) = 0, \qquad \vartheta'(1,t) = 0. \tag{2.9b}$$

2.3 MLPG formulation

2.3.1 Local symmetric nonlinear augmented weak form (LSNAWF)

Let $\Omega_{\mathrm{S}}^i \subseteq [0,1]$, $i = 1, 2, \ldots, N$ be a family of subdomains of the global domain $[0,1]$ such that $\bigcup_{i=1}^N \Omega_{\mathrm{S}}^i = [0,1]$ and Ω_{S}^i contains the i-th node; note that Ω_{S}^i need not to be disjoint in the MLPG formulation. We introduce the following local symmetric nonlinear augmented weak form (LSNAWF) of the problem on the i-th subdomain Ω_{S}^i. The equation

$$\begin{aligned}
0 = & \int_{\Omega_{\mathrm{S}}^i} \tilde{v}_i \dot{v} \mathrm{d}y - \int_{\Omega_{\mathrm{S}}^i} \varrho^{-1} \tilde{v}_i s' \mathrm{d}y \\
& + \left[\delta_0 \left(\lambda_0 \tilde{v}_i + \tilde{\lambda}_0 v\right)\right]\Big|_{\Gamma_{\mathrm{S}}^{i-}} - \left[\delta_1 \left(\lambda_1 \tilde{v}_i + \tilde{\lambda}_1 (v-1)\right)\right]\Big|_{\Gamma_{\mathrm{S}}^{i+}} \\
+ & \int_{\Omega_{\mathrm{S}}^i} \tilde{\vartheta}_i \dot{\vartheta} \mathrm{d}y + \int_{\Omega_{\mathrm{S}}^i} \kappa \tilde{\vartheta}_i' \vartheta' \mathrm{d}y - \int_{\Omega_{\mathrm{S}}^i} \tilde{\vartheta}_i \Lambda s^2 \mathrm{d}y \\
& + \left[(1-\delta_0)\, \tilde{\vartheta}_i \vartheta'\right]\Big|_{\Gamma_{\mathrm{S}}^{i-}} - \left[(1-\delta_1)\, \tilde{\vartheta}_i \vartheta'\right]\Big|_{\Gamma_{\mathrm{S}}^{i+}} \\
+ & \int_{\Omega_{\mathrm{S}}^i} \tilde{s}_i \dot{s} \mathrm{d}y - \int_{\Omega_{\mathrm{S}}^i} \mu \tilde{s}_i \left(v' - \Lambda s\right) \mathrm{d}y \\
+ & \int_{\Omega_{\mathrm{S}}^i} \tilde{\psi}_i \dot{\psi} \mathrm{d}y - \int_{\Omega_{\mathrm{S}}^i} \tilde{\psi}_i \Lambda s^2 \left(1 + \frac{\psi}{\psi_0}\right)^{-n} \mathrm{d}y,
\end{aligned} \tag{2.10}$$

with Λ given by equation Eq. (2.4e) must hold for all choices of test functions $\tilde{v}_i$, $\tilde{\vartheta}_i$, $\tilde{s}_i$, $\tilde{\psi}_i$, $\tilde{\lambda}_0$, and $\tilde{\lambda}_1$. Here, $\tilde{v}_i \in L^2(0,1)$, $\tilde{\vartheta}_i \in H^1(0,1)$, $\tilde{s}_i \in L^2(0,1)$, $\tilde{\psi}_i \in L^2(0,1)$, and $\tilde{\lambda}_0$, $\tilde{\lambda}_1 \in \mathbb{R}$.

$$\delta_\xi(\zeta) := \begin{cases} 1, & \zeta = \xi \\ 0, & \zeta \neq \xi \end{cases} \tag{2.11}$$

is the characteristic function, and Γ_{S}^{i-}, Γ_{S}^{i+} are the left and the right boundary points of the subdomain Ω_{S}^i. Since the MLS basis function do not possess Kronecker delta property, essential boundary conditions (2.9a) cannot be imposed directly at the boundary nodes. Therefore, Lagrange multipliers λ_0 and λ_1 have been introduced. We emphasize that the homogeneous natural boundary conditions (2.9b) have been incorporated in the LSNAWF. The variational statement expressed by Eq. (2.10) can be derived by following classical arguments, see e.g. Mura & Koya (1992).

Since Eq. (2.10) is required to hold for all choices of $\tilde{v}_i$, $\tilde{s}_i$, $\tilde{\vartheta}_i$, $\tilde{\psi}_i$, $\tilde{\lambda}_0$, and $\tilde{\lambda}_1$, Eqs. (2.4a), (2.4c), and (2.4d) and essential boundary conditions (2.9a) immediately follow from it. An integration by parts of the term involving ϑ' and then exploiting the arbitrariness of $\tilde{\vartheta}_i$ yields Eq. (2.4b) and natural boundary conditions (2.9b).

2.3.2 Semidiscrete formulation

In order to seek an approximate solution of the nonlinear initial-boundary-value problem defined by Eq. (2.10), we approximate fields v, ϑ, s, and ψ by using the MLS basis functions (A.14) given in Appendix A.1:

$$v^h(y,t) = \boldsymbol{\varphi}(y)^{\mathrm{T}}\hat{\mathbf{v}}(t), \tag{2.12a}$$

$$\vartheta^h(y,t) = \boldsymbol{\varphi}(y)^{\mathrm{T}}\hat{\boldsymbol{\vartheta}}(t), \tag{2.12b}$$

$$s^h(y,t) = \boldsymbol{\varphi}(y)^{\mathrm{T}}\hat{\mathbf{s}}(t), \tag{2.12c}$$

$$\psi^h(y,t) = \boldsymbol{\varphi}(y)^{\mathrm{T}}\hat{\boldsymbol{\psi}}(t). \tag{2.12d}$$

Here, $\boldsymbol{\varphi}$ are basis functions, and $\hat{\mathbf{v}}$ the vector of fictitious nodal velocities. For convenience, we collect the fictitious nodal unknowns and the Lagrange multipliers into the $4N$- and the 2-dimensional vectors:

$$\hat{\mathbf{u}}(t) := \left[\hat{\mathbf{v}}(t) \;\; \hat{\boldsymbol{\vartheta}}(t) \;\; \hat{\mathbf{s}}(t) \;\; \hat{\boldsymbol{\psi}}(t)\right]^{\mathrm{T}}, \tag{2.13a}$$

$$\boldsymbol{\lambda}(t) := \left[\lambda_0(t) \;\; \lambda_1(t)\right]^{\mathrm{T}}, \tag{2.13b}$$

where N is the number of nodes in the global domain $[0,1]$.

In order to obtain $4N+2$ equations for the $4N+2$ unknowns $\hat{\mathbf{u}}(t)$ and $\boldsymbol{\lambda}(t)$, we consider $4N+2$ independent test functions in Eq. (2.10):

$$\tilde{v}_1,\ldots,\tilde{v}_N, \quad \tilde{\vartheta}_1,\ldots,\tilde{\vartheta}_N, \quad \tilde{s}_1,\ldots,\tilde{s}_N, \quad \tilde{\psi}_1,\ldots,\tilde{\psi}_N, \quad \tilde{\lambda}_0,\tilde{\lambda}_1. \tag{2.14}$$

We choose the support of the MLS basis function for the i-th node to be the i-th subdomain Ω_{S}^i, and the related test function to be the MLS basis function. Therefore, since the test and the trial functions are chosen from the same space, we get the following local nonlinear Bubnov-Galerkin (MLPG6) semidiscrete formulation:

$$\mathbf{M}\dot{\hat{\mathbf{u}}}(t) = \mathbf{G}\left(\hat{\mathbf{u}}(t)\right) + \mathbf{L}^{\mathrm{T}}\boldsymbol{\lambda}(t), \tag{2.15}$$

$$\mathbf{L}\hat{\mathbf{u}}(t) = \bar{\mathbf{u}}, \tag{2.16}$$

where $\mathbf{M}$ is a $(4N\times 4N)$-matrix, given by

$$\mathbf{M} = \mathrm{DIAG}\left[\mathbf{D},\mathbf{D},\mathbf{D},\mathbf{D}\right], \qquad \left[\mathbf{D}\right]_{ij} = \int_{\Omega_{\mathrm{S}}^i}\varphi_i\varphi_j\mathrm{d}y, \quad i,j=1,\ldots N, \tag{2.17}$$

and $\mathbf{L}$ is a $(2 \times 4N)$-matrix given by

$$[\mathbf{L}]_{1j} = [\delta_0 \varphi_j]|_{\Gamma_{\mathrm{S}}^{j-}}, \quad [\mathbf{L}]_{2j} = [-\delta_1 \varphi_j]|_{\Gamma_{\mathrm{S}}^{j+}}, \qquad j = 1, \ldots, 4N. \tag{2.18}$$

Eq. (2.16) is the affine constraint, with the 2-vector $\bar{\mathbf{u}}$ given by

$$\bar{\mathbf{u}} = [0 \;\; 1]^{\mathrm{T}}. \tag{2.19}$$

The nonlinear operator $\mathbf{G}$ appearing on the right-hand side of Eq. (2.15) can be conveniently written as

$$\mathbf{G}(\hat{\mathbf{u}}(t)) = \left[\mathbf{G}^1(\hat{\mathbf{u}}(t)) \;\; \mathbf{G}^2(\hat{\mathbf{u}}(t)) \;\; \mathbf{G}^3(\hat{\mathbf{u}}(t)) \;\; \mathbf{G}^4(\hat{\mathbf{u}}(t))\right]^{\mathrm{T}}, \tag{2.20}$$

with

$$\left[\mathbf{G}^1(\hat{\mathbf{u}})\right]_i = \int_{\Omega_{\mathrm{S}}^i} \varrho^{-1} \varphi_i \, \varphi_j' \hat{s}_j \mathrm{d}y, \tag{2.21a}$$

$$\left[\mathbf{G}^2(\hat{\mathbf{u}})\right]_i = -\int_{\Omega_{\mathrm{S}}^i} \kappa \varphi_i' \, \varphi_j' \hat{\vartheta}_j \mathrm{d}y + \int_{\Omega_{\mathrm{S}}^i} \varphi_i \, \Lambda^h(\hat{\mathbf{u}}) \, (\varphi_j \hat{s}_j)^2 \, \mathrm{d}y, \tag{2.21b}$$

$$\left[\mathbf{G}^3(\hat{\mathbf{u}})\right]_i = \int_{\Omega_{\mathrm{S}}^i} \mu \varphi_i \, \left(\varphi_j' \hat{v}_j - \Lambda^h(\hat{\mathbf{u}}) \, \varphi_j \hat{s}_j\right) \mathrm{d}y, \tag{2.21c}$$

$$\left[\mathbf{G}^4(\hat{\mathbf{u}})\right]_i = \int_{\Omega_{\mathrm{S}}^i} \varphi_i \, \Lambda^h(\hat{\mathbf{u}}) \, (\varphi_j \hat{s}_j)^2 \left(1 + \frac{\varphi_j \hat{\psi}_j}{\psi_0}\right)^{-n} \mathrm{d}y, \tag{2.21d}$$

$i = 1, 2, \ldots, N$. In Eqs. (2.21) and (2.22), a repeated index is summed over the range $1, \ldots, N$ of the index, and the term $\Lambda^h(\hat{\mathbf{u}})$ is given by

$$\mathbf{\Lambda}^h(\hat{\mathbf{u}}) = \max\left\{0, \frac{1}{b\varphi_j \hat{\mathbf{s}}_j}\left(\left(\frac{\varphi_j \hat{\mathbf{s}}_j}{\left(1 - a\varphi_j \hat{\vartheta}_j\right)\left(1 + \frac{\varphi_j \hat{\psi}_j}{\psi_0}\right)^n}\right)^{1/m} - 1\right)\right\}. \tag{2.22}$$

Let $\mathbf{L}^*$ be the pseudoinverse (see e.g. Press et al. (1992)) of the matrix $\mathbf{L}$. Introducing

$$\underline{\mathbf{u}} := \mathbf{L}^* \bar{\mathbf{u}}, \tag{2.23}$$

the affine constraint (2.16) can be rewritten as

$$\mathbf{L}(\hat{\mathbf{u}}(t) - \underline{\mathbf{u}}) = \mathbf{0}. \tag{2.24}$$

Let rows of the $((4N-2) \times 4N)$-matrix $\mathbf{X}$ be comprised of $(4N-2)$ linearly independent null vectors of the $(2 \times 4N)$-matrix $\mathbf{L}$, and set

$$\hat{\mathbf{u}}(t) = \underline{\mathbf{u}} + \mathbf{X}^{\mathrm{T}} \mathbf{u}(t). \tag{2.25}$$

Substitution from Eq. (2.25) into Eq. (2.24) gives

$$\mathbf{L}\,\mathbf{X}^{\mathrm{T}} \mathbf{u} = \mathbf{0}, \tag{2.26}$$

which are identically satisfied for every $(4N-2)$-dimensional vector $\mathbf{u}$. Premultiplying both sides of Eq. (2.15) by $\mathbf{X}$ and substituting from Eq. (2.25) we obtain the following reduced system of $(4N-2)$ nonlinear equations for $\mathbf{u}$:

$$\bar{\mathbf{M}}\,\dot{\mathbf{u}} = \bar{\mathbf{G}}\,(\mathbf{u})\,, \tag{2.27}$$

where

$$\bar{\mathbf{M}} = \mathbf{X}\mathbf{M}\mathbf{X}^{\mathrm{T}}, \qquad \bar{\mathbf{G}}\,(\mathbf{u}) = \mathbf{X}\,\mathbf{G}\left(\underline{\mathbf{u}} + \mathbf{X}^{\mathrm{T}}\mathbf{u}\right). \tag{2.28}$$

Having found $\mathbf{u}$ from Eq. (2.27), $\hat{\mathbf{u}}$ is computed from Eq. (2.25).

2.4 Computation and discussion of results

2.4.1 Time integration scheme

As noted earlier the readily available integrators for ordinary differential equations, such as LSODE used by Batra & Kim (1990) and Batra & Zhang (2004), could not be employed because of a lack of the Kronecker delta property of the MLS basis functions. We briefly describe below the time integration scheme used herein.

Let the solution $\mathbf{u}_{n-1} = \mathbf{u}\,(t_{n-1})$ of the system (2.27) at time t_{n-1} be known. The solution $\mathbf{u}_n = \mathbf{u}_{n-1} + \Delta\mathbf{u}_n$ at time $t_n = t_{n-1} + \Delta t_n$ is obtained as the root of the following nonlinear equation:

$$\mathbf{u}_n = \mathbf{u}_{n-1} + \Delta t_n \mathbf{f}\,(\mathbf{u}_n)\,, \tag{2.29}$$

where $\mathbf{f} = \bar{\mathbf{M}}^{-1} \circ \bar{\mathbf{G}}$. The single step algorithm expressed in Eq. (2.29) can be regarded both as the first order Adam-Moulton implicit method and the first order backward difference method (see e.g. Gear (1971)).

The solution of the set (2.29) of nonlinear equations in terms of unknowns $\Delta\mathbf{u}_n$ is found by using Newton's iterations. Hence the generic α-th iteration is

$$\Delta\mathbf{u}_n^{(\alpha)} = \Delta t_n \left(\mathbf{f}\left(\mathbf{u}_n^{(\alpha-1)}\right) + \left[\nabla_{\mathbf{u}}\mathbf{f}\left(\mathbf{u}_n^{(\alpha-1)}\right)\right]\,\Delta\mathbf{u}_n^{(\alpha)}\right) - \sum_{p=1}^{\alpha-1}\Delta\mathbf{u}_n^{(p)}, \tag{2.30}$$

where $\Delta\mathbf{u}_n^{(\alpha)}$ indicates the α-th solution increment with $\Delta\mathbf{u}_n^{(0)} = \mathbf{0}$, and $\mathbf{u}_n^{(\alpha-1)}$ is the updated solution at the $(\alpha-1)$-th iteration, i.e.,

$$\mathbf{u}_n^{(\alpha-1)} = \mathbf{u}_{n-1} + \sum_{p=1}^{\alpha-1}\Delta\mathbf{u}_n^{(p)}. \tag{2.31}$$

The linear operator $\nabla_{\mathbf{u}}\mathbf{f}$ is the derivative of $\mathbf{f}$ with respect to $\mathbf{u}$; recalling Eq. (2.28) it can be expressed as

$$\nabla_{\mathbf{u}}\mathbf{f} = \bar{\mathbf{M}}^{-1}\left[\nabla_{\mathbf{u}}\bar{\mathbf{G}}\right] = \bar{\mathbf{M}}^{-1}\mathbf{X}\left[\nabla_{\hat{\mathbf{u}}}\mathbf{G}\right]\mathbf{X}^{\mathrm{T}}. \tag{2.32}$$

The gradient of $\mathbf{G}$ can be written as

$$\nabla_{\hat{\mathbf{u}}}\mathbf{G} = \begin{pmatrix} \mathbf{0} & \nabla_{\hat{\mathbf{s}}}\mathbf{G}^1 & \mathbf{0} & \mathbf{0} \\ \mathbf{0} & \nabla_{\hat{\boldsymbol{\vartheta}}}\mathbf{G}^2 & \nabla_{\hat{\mathbf{s}}}\mathbf{G}^2 & \nabla_{\hat{\boldsymbol{\psi}}}\mathbf{G}^2 \\ \nabla_{\hat{\mathbf{v}}}\mathbf{G}^3 & \nabla_{\hat{\boldsymbol{\vartheta}}}\mathbf{G}^3 & \nabla_{\hat{\mathbf{s}}}\mathbf{G}^3 & \nabla_{\hat{\boldsymbol{\psi}}}\mathbf{G}^3 \\ \mathbf{0} & \nabla_{\hat{\boldsymbol{\vartheta}}}\mathbf{G}^4 & \nabla_{\hat{\mathbf{s}}}\mathbf{G}^4 & \nabla_{\hat{\boldsymbol{\psi}}}\mathbf{G}^4 \end{pmatrix}. \tag{2.33}$$

At a generic solution point $\hat{\mathbf{u}}_n$

$$\left[\nabla_{\hat{\mathbf{s}}}\mathbf{G}^1\left(\hat{\mathbf{u}}_n\right)\right]_{ij} = \int_{\Omega_{\mathrm{S}}^i} \varrho^{-1}\varphi_i\,\varphi_j' \mathrm{d}y, \tag{2.34a}$$

$$\left[\nabla_{\hat{\boldsymbol{\vartheta}}}\mathbf{G}^2\left(\hat{\mathbf{u}}_n\right)\right]_{ij} = -\int_{\Omega_{\mathrm{S}}^i} \kappa\varphi_i'\varphi_j' \mathrm{d}y + \int_{\Omega_{\mathrm{S}}^i} \varphi_i\varphi_j\chi^{22}\left(\hat{\mathbf{u}}_n\right)\mathrm{d}y, \tag{2.34b}$$

$$\left[\nabla_{\hat{\mathbf{s}}}\mathbf{G}^2\left(\hat{\mathbf{u}}_n\right)\right]_{ij} = \int_{\Omega_{\mathrm{S}}^i} \varphi_i\varphi_j\chi^{23}\left(\hat{\mathbf{u}}_n\right)\mathrm{d}y, \tag{2.34c}$$

$$\left[\nabla_{\hat{\boldsymbol{\psi}}}\mathbf{G}^2\left(\bar{\hat{\mathbf{u}}}\right)\right]_{ij} = \int_{\Omega_{\mathrm{S}}^i} \varphi_i\varphi_j\chi^{24}\left(\hat{\mathbf{u}}_n\right)\mathrm{d}y, \tag{2.34d}$$

$$\left[\nabla_{\hat{\mathbf{v}}}\mathbf{G}^3\left(\hat{\mathbf{u}}_n\right)\right]_{ij} = \int_{\Omega_{\mathrm{S}}^i} \mu\varphi_i\,\varphi_j' \mathrm{d}y, \tag{2.34e}$$

$$\left[\nabla_{\hat{\boldsymbol{\vartheta}}}\mathbf{G}^3\left(\hat{\mathbf{u}}_n\right)\right]_{ij} = \int_{\Omega_{\mathrm{S}}^i} \varphi_i\varphi_j\chi^{32}\left(\hat{\mathbf{u}}_n\right)\mathrm{d}y, \tag{2.34f}$$

$$\left[\nabla_{\hat{\mathbf{s}}}\mathbf{G}^3\left(\hat{\mathbf{u}}_n\right)\right]_{ij} = \int_{\Omega_{\mathrm{S}}^i} \varphi_i\varphi_j\chi^{33}\left(\hat{\mathbf{u}}_n\right)\mathrm{d}y, \tag{2.34g}$$

$$\left[\nabla_{\hat{\boldsymbol{\psi}}}\mathbf{G}^3\left(\hat{\mathbf{u}}_n\right)\right]_{ij} = \int_{\Omega_{\mathrm{S}}^i} \varphi_i\varphi_j\chi^{34}\left(\hat{\mathbf{u}}_n\right)\mathrm{d}y, \tag{2.34h}$$

$$\left[\nabla_{\hat{\boldsymbol{\vartheta}}}\mathbf{G}^4\left(\hat{\mathbf{u}}_n\right)\right]_{ij} = \int_{\Omega_{\mathrm{S}}^i} \varphi_i\varphi_j\chi^{42}\left(\hat{\mathbf{u}}_n\right)\mathrm{d}y, \tag{2.34i}$$

$$\left[\nabla_{\hat{\mathbf{s}}}\mathbf{G}^4\left(\hat{\mathbf{u}}_n\right)\right]_{ij} = \int_{\Omega_{\mathrm{S}}^i} \varphi_i\varphi_j\chi^{43}\left(\hat{\mathbf{u}}_n\right)\mathrm{d}y, \tag{2.34j}$$

$$\left[\nabla_{\hat{\boldsymbol{\psi}}}\mathbf{G}^4\left(\hat{\mathbf{u}}_n\right)\right]_{ij} = \int_{\Omega_{\mathrm{S}}^i} \varphi_i\varphi_j\chi^{44}\left(\hat{\mathbf{u}}_n\right)\mathrm{d}y, \tag{2.34k}$$

$i, j = 1, 2, \ldots, N$. Expressions for functions χ are given in Appendix D.

The increment $\Delta\mathbf{u}_n^{(\alpha)}$ at the α-th iteration is then the solution of the linear system

$$\mathbf{K}_n^{(\alpha)}\Delta\mathbf{u}_n^{(\alpha)} = \mathbf{F}_n^{(\alpha)}, \tag{2.35}$$

where

$$\mathbf{K}_n^{(\alpha)} := \mathbf{1} - \Delta t_n\,\nabla_{\mathbf{u}}\mathbf{f}\left(\mathbf{u}_n^{(\alpha-1)}\right), \qquad \mathbf{F}_n^{(\alpha)} := \Delta t_n\,\mathbf{f}\left(\mathbf{u}_n^{(\alpha-1)}\right) - \sum_{p=1}^{\alpha-1}\Delta\mathbf{u}_n^{(p)}, \tag{2.36}$$

and $\mathbf{1}$ is the $(4N-2)\times(4N-2)$-identity matrix. Iterations are performed until a suitable magnitude of the increment reaches a prescribed tolerance ε_{T}. In particular, we choose to monitor the sum of L^2 norms of increments in the approximate solutions:

$$\left\|\Delta\hat{\mathbf{u}}_n^{(\alpha)}\right\|_{L^2_{4N}}^2 := \int_0^1 \left(\left(\boldsymbol{\varphi}^{\mathrm{T}}\Delta\hat{\mathbf{v}}_n^{(\alpha)}\right)^2 + \left(\boldsymbol{\varphi}^{\mathrm{T}}\Delta\hat{\boldsymbol{\vartheta}}_n^{(\alpha)}\right)^2 + \left(\boldsymbol{\varphi}^{\mathrm{T}}\Delta\hat{\mathbf{s}}_n^{(\alpha)}\right)^2 + \left(\boldsymbol{\varphi}^{\mathrm{T}}\Delta\hat{\boldsymbol{\psi}}_n^{(\alpha)}\right)^2 \right) \mathrm{d}y < \varepsilon_{\mathrm{T}}, \quad (2.37)$$

where

$$\varepsilon_{\mathrm{T}} = \varepsilon_{\mathrm{A}} + \varepsilon_{\mathrm{R}} \left\|\Delta\hat{\mathbf{u}}_n^{(1)}\right\|_{L^2_{4N}}, \quad (2.38)$$

and ε_{A} and ε_{R} are the absolute and the relative tolerances respectively. If the solution increment fails to converge in the norm (2.37) after 50 iterations, the process is restarted with the time step reduced by $1/\sqrt{2}$.

After convergence is achieved, the local truncation error test is performed. The local truncation error $\boldsymbol{\epsilon}_n$ is defined as the amount by which the solution of the differential equation fails to satisfy the equation used in the numerical integration algorithm (see Gear (1971)). Thus, for the one step algorithm (2.29),

$$\boldsymbol{\epsilon}_n = \Delta\mathbf{u}_n - \Delta t_n \mathbf{f}\left(\mathbf{u}_n\right), \quad (2.39)$$

where $\mathbf{u}_n$ is the converged solution. The estimate for $\boldsymbol{\epsilon}_n$ is given by

$$\frac{\Delta t_n^2}{2}\ddot{\mathbf{u}}_n, \quad (2.40)$$

or equivalently, by using Eq. (2.27)

$$\boldsymbol{\epsilon}_n = \frac{\Delta t_n^2}{2}\dot{\mathbf{f}}\left(\mathbf{u}_n\right) = \frac{\Delta t_n^2}{2}\left[\nabla_{\mathbf{u}}\mathbf{f}\left(\mathbf{u}_n\right)\right]\dot{\mathbf{u}}_n = \frac{\Delta t_n^2}{2}\left[\nabla_{\mathbf{u}}\mathbf{f}\left(\mathbf{u}_n\right)\right]\mathbf{f}\left(\mathbf{u}_n\right). \quad (2.41)$$

If the following test

$$\|\hat{\boldsymbol{\epsilon}}_n\|_{L^2_{4N}} \leq \varepsilon_{\mathrm{A}}^{\mathrm{LT}} + \varepsilon_{\mathrm{R}}^{\mathrm{LT}} \|\Delta\hat{\mathbf{u}}_n\|_{L^2_{4N}}, \quad (2.42)$$

fails, then the process is restarted with a time step reduced by $\sqrt{2}$. In Eq. (2.42), $\varepsilon_{\mathrm{A}}^{\mathrm{LT}}$ and $\varepsilon_{\mathrm{R}}^{\mathrm{LT}}$ are the absolute and the relative tolerances for the local truncation error test. From Eqs. (2.40) and (2.25), we get $\hat{\boldsymbol{\epsilon}}_n = \mathbf{X}^{\mathrm{T}}\boldsymbol{\epsilon}_n$.

2.4.2 Numerical results

Results presented below have been obtained by assigning following values to nondimensional parameters:

$$\varrho = 3.928\times10^{-5}, \quad \mu = 240.3, \quad a = 0.4973, \quad n = 0.09, \quad (2.43a)$$

$$\kappa = 3.978\times10^{-3}, \quad \psi_0 = 0.017, \quad m = 0.025, \quad b = 5\times10^{6}. \quad (2.43b)$$

These values are for a typical steel when the average strain rate $\dot{\gamma}_0$ is $500\,\mathrm{s}^{-1}$, except for the thermal softening parameter a whose value is enhanced in order to reduce the computational time. Batra & Zhang (2004) performed a parametric study to delineate the effect of a in Eq. (2.2), revealing that for $a = 0.2$ and 0.25 the drop in the shear stress is catastrophic enough for the elastic unloading wave to emanate from the center of the ASB, while for $a = 0.15$ and 0.1 the shear stress does not decrease rapidly enough for the wave to emanate. An expression for the ASB initiation time with a is derived in Batra & Zhang (2004) by fitting a curve to the computed data. The temperature rise in °C is obtained by multiplying the nondimensional one with 89.6 °C. The block height H has been chosen as 2.58 mm.

The MLS approximation (see Appendix A.1) uses linear monomial bases. A nonuniform placement of nodes with nodal coordinates given by

$$y_j = \left(\frac{j-1}{N-1}\right)^3, \qquad j = 1, \ldots, N, \tag{2.44}$$

has been used. Because of the small distance between two adjacent nodes near the origin, and for the matrix $\mathbf{A}$ to be well conditioned in the entire domain, we set the radii of the spline weight functions (A.22) as

$$r_j = \varepsilon_j \left(y_{j+1} - y_j\right), \quad j = 1, 2, \ldots, N-1, \qquad r_N = \varepsilon_N \left(y_N - y_{N-1}\right), \tag{2.45}$$

with

$$\varepsilon_j = 5 + \left(1 - y_j\right)^3, \qquad j = 1, 2, \ldots, N. \tag{2.46}$$

From numerical experiments we found that the radii of weight functions supports as given by Eqs. (2.45) and (2.46), are the minimum required for matrix $\mathbf{A}$ to be well conditioned. As previously mentioned, the subdomain Ω_{S}^i is chosen to be the support of the MLS basis function φ_i for node i with coordinate y_i.

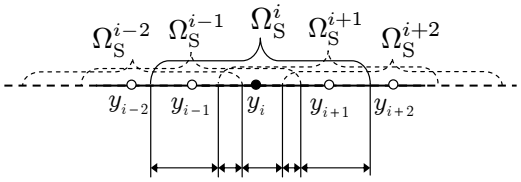

Figure 2.2: Subdomain Ω_{S}^i associated with the node at y_i, and subregions for integration given by boundaries of intersecting subdomains.

Since the MLS basis functions are not polynomials the use of the standard Gauss quadrature rule requires a large number of quadrature points to accurately evaluate domain integrals in

Eqs. (2.34). This is overcome by using the integration procedure proposed by Atluri et al. (1999). The idea is sketched in Fig. 2.2, where a possible arrangement of nodes is shown. The integrations on Ω_S^i are performed on each subregion, obtained by dividing the subdomain by boundaries of intersecting subdomains of other nodes. In the present work the numerical integration has been performed by placing 5 quadrature points in each subregion.

The absolute and the relative tolerances ε_A and ε_R in Eq. (2.38) have been set equal to 10^{-7}, while tolerances ε_A^{LT} and ε_R^{LT} in Eq. (2.42) have been set equal to 10^{-4}.

In the absence of an analytical solution, computed results are compared with the numerical solution obtained by the FE code developed by Batra & Kim (1990) with a nonuniform mesh given by

$$y_j = \left(\frac{j-1}{200}\right)^5, \quad j = 1, 2, \ldots, 201, \tag{2.47}$$

and with the MSPH numerical solution obtained by Batra & Zhang (2004) with 442 particles; in Batra & Kim (1990) and Batra & Zhang (2004) the time integration has been performed with the subroutine LSODE taken from the package ODEPACK, and the number of nodes and particles was large enough to get a converged solution of the problem. The following error measure

$$\eta(y,t) = \frac{s(y,t)}{s^{FE}(y,t)} - 1, \qquad \eta_0 = \sup_{\substack{0\le y\le 1\\ 0\le t\le T}} |\eta(y,t)|, \tag{2.48}$$

has been considered, where s^{FE} is the reference converged FE solution obtained with the nodal distribution (2.47), and $T = 60.8\,\mu$s.

Table 2.1: ASB initiation times, maximum errors η_0 (Eq. (2.48)), speeds of the elastic unloading wave, and the ASB width, obtained with the MLPG6 method for different number of nodes, compared with those obtained by Batra & Zhang (2004) with the FE and the MSPH methods.

	Number of nodes (particles for MSPH)	ASB initiation time, [μs]	η_0	Speed of the unloading elastic wave	ASB width, [μm]
	161	60.42	0.606	2510	13.67
	201	60.46	0.473	2500	12.39
	301	60.50	0.378	2487	10.32
	401	60.50	0.378	2487	10.32
FE	201	60.55	–	2473	12.54
MSPH	442	60.56	0.0590	2473	10.32

In Table 2.1 the ASB initiation times at the point $y = 0$, for different values of N in Eq. (2.44), are compared with those obtained by Batra & Zhang (2004) with the FE and the MSPH methods. An ASB is assumed to initiate at a point when the shear stress there has dropped

to 80% of its peak value at that point, and the material point is deforming plastically. This criterion reflects Marchand & Duffy's (1988) observation that the torque required to twist thin-walled tubes drops precipitously upon the initiation of an ASB. It is evident from the results listed in Table 2.1 that there is no difference between values obtained by using 301 and 401 nodes. The percentage error in the presently computed value of the ASB initiation time with 301 nodes is

$$100 \times \left| 1 - \frac{t_{\rm ASB}^{\rm MLPG6}}{t_{\rm ASB}^{\rm FE}} \right| \simeq 0.08. \tag{2.49}$$

From an examination of values of η_0 defined by Eq. (2.48) and given in Table 2.1, it is clear that the maximum error decreases with an increase in the number of nodes. The primary reason for a rather large value of η_0 is the slight difference in the ASB initiation times. Because of the earlier initiation of an ASB in the present work, the shear stress at $y = 0$ has dropped drastically at $t = 60.5\mu$s but not in the FE solution. As the presently computed ASB initiation time approaches that obtained with the FEM, the difference in the two spatial variations of the shear stress, the particle velocity, and the temperature rise decreases and the value of η_0 decreases. We note that, for the present problem, the FEM gives a converged value of the ASB initiation time with 201 nonuniformly spaced nodes and requires the least amount of CPU time out of the FE, the MSPH, and the MLPG methods. Whereas for most linear elastic problems the MLPG method requires more CPU time than the FEM but gives results of the same accuracy with fewer nodes. Here, for the problem involving the localization of deformation into a narrow band, the MSPH and the MLPG6 methods require more nodes (particles) than the FEM. We note that the FE solution of the problem computed with 201 nodes with coordinates given by Eq. (2.44) is virtually identical to that obtained with nodal positions given by Eq. (2.47). Thus the slight difference in results computed with the MLPG6 and the FE methods is not due to the spatial locations of nodes. We have experimented with using multiquadratic basis functions in the MLPG6 formulation and found that they work well when nodes are uniformly distributed and, at least for the present problem, are not advantageous. We also used MLPG1 formulation with weight functions in the MLS basis functions taken as the test functions. This resulted in asymmetric mass matrix and neither reduced the CPU time required to numerically solve the problem nor improved the accuracy of results.

All results presented below have been computed with $N = 301$ in Eq. (2.44).

In Fig. 2.3(a) is shown the time history of evolution of the nondimensional shear stress s at $y = 0$; Fig. 2.3(b) depicts the same results for $60.3\,\mu\text{s} \le t \le 61.1\,\mu\text{s}$, and reveals that the collapse in the shear stress at $y = 0$ occurs during the $0.15\,\mu$s time interval that starts at $t = 60.5\,\mu$s; the beginning of the collapse at this instant signifies the initiation of an ASB at $t = 60.5\,\mu$s. The dramatic drop in the shear stress at $y = 0$ results in an elastic unloading shock wave that propagates outwards from the specimen center; this is shown in

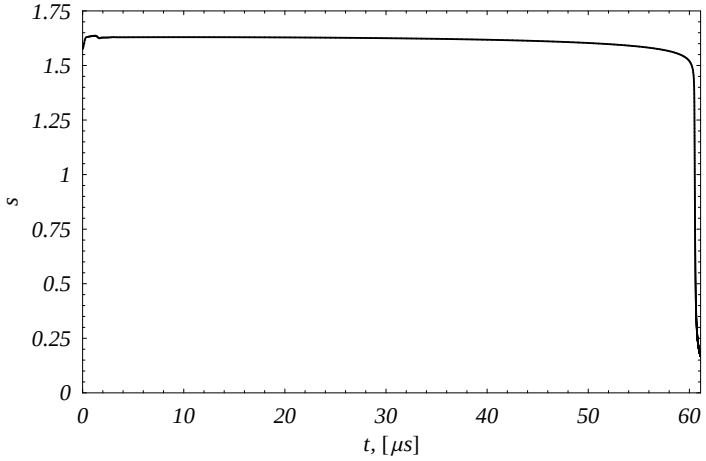

(a)

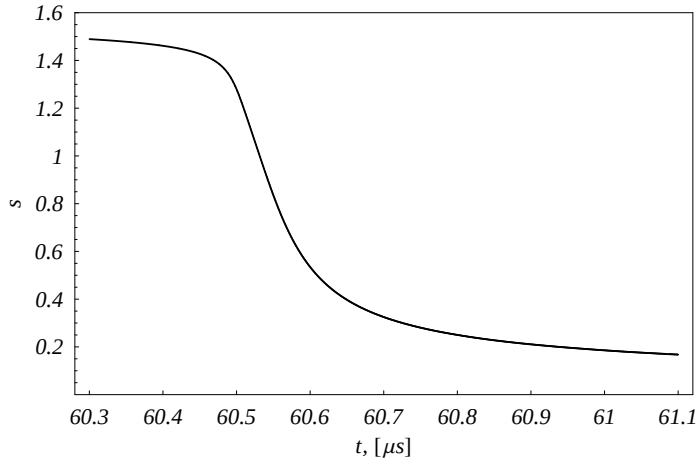

(b)

Figure 2.3: Time history of the nondimensional shear stress at the specimen center (a) 0μs $\leq t \leq$ 61.1μs, (b) 60.3μs $\leq t \leq 61.1\mu$s.

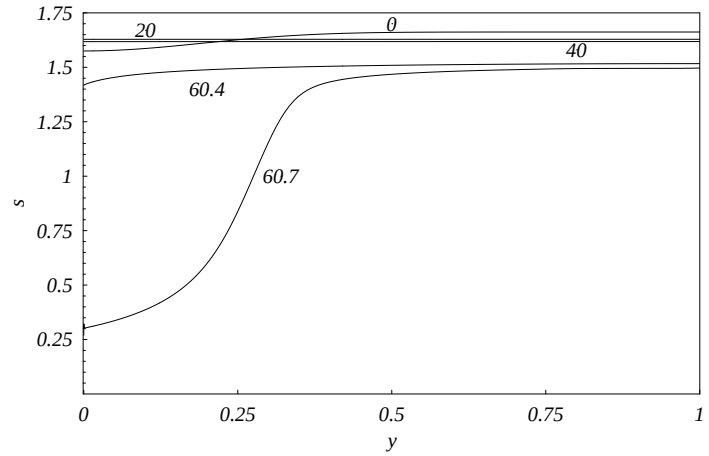

(a)

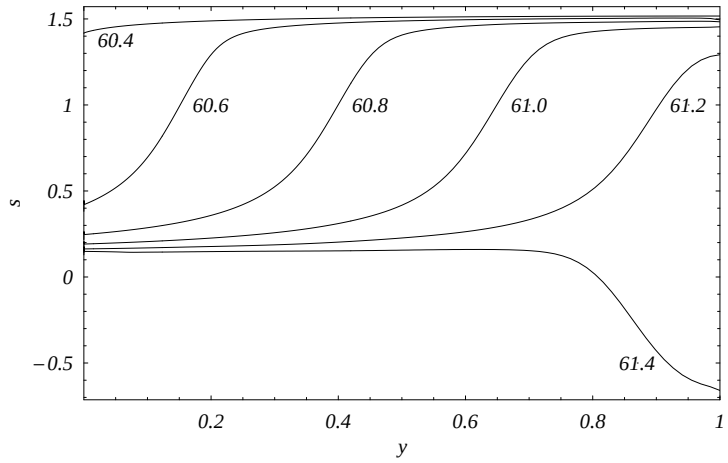

(b)

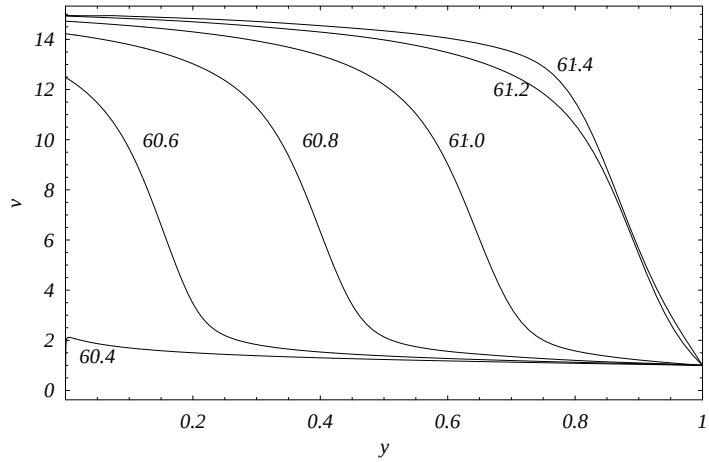

(c)

Figure 2.4: (a) Spatial distribution of the nondimensional shear stress at times 0, 20, 40, 60.4 and 60.7μs; (b) and (c): Spatial distribution of (b) the shear stress and (c) the velocity at different times during the localization phenomenon. Curves are plotted at 0.2μs interval with the first one at 60.4μs.

Figs. 2.4(b) and 2.4(c), where the spatial variation of the shear stress and the velocity are plotted at different times. The nondimensional wave speed computed from the shear stress data is 2487, which is very close to the analytical value $\sqrt{\mu/\varrho} = 2473.38$. It takes about $0.8\,\mu$s for the wave to reach $y = 1$ from where it is reflected back with a negative value of the shear stress; the reflected wave is shown in Figs. 2.4(b) and 2.4(c) at $61.4\,\mu$s. Values of the nondimensional wave speed computed from solutions with different node numbers are compared in Table 2.1 with those from the MSPH and the FE methods. It is clear that with an increase in the number of nodes, the presently computed speed of the elastic unloading wave approaches the analytical value, and also that computed with the MSPH and the FE methods. We note that results plotted in Fig. 2.4 when adjusted for the difference in the ASB initiation time agree very well with those computed with the FE and the MSPH methods.

In Fig. 2.5(a) the spatial distribution of the temperature rise at four different times is shown, and in Fig. 2.5(b) the same result is plotted for $0 \leq y \leq 5 \times 10^{-3}$. One can see that for $t \leq 60.4\,\mu$s the temperature at $y = 0$ rises slowly and that it increases more near the origin than at points away from $y = 0$. During the $0.3\,\mu$s time interval between $t = 60.4\,\mu$s and $t = 60.7\,\mu$s the temperature near the origin rises sharply; in the same time interval the shear stress in the same region collapses. The average rate of rise of temperature during this $0.3\,\mu$s interval equals $3 \times 10^7\,\mathrm{s}^{-1}$ or $2.7 \times 10^9\,^\circ$C/s. The monotonic increase in the rate of temperature rise suggests that in the shear banded region the rate of increase in the plastic strain rate is higher than the rate of decrease in the shear stress. Eventually, most of the heat generated within the ASB is conducted out of edges of the ASB, and the temperature within the shear banded region does not increase much. For a typical steel, Batra & Chen (2001) found that 95% of the heat produced due to plastic working is conducted out of the shear banded region. The sudden jump in the rate of increase of the temperature at $t = 60.5\,\mu$s is shown in Figs. 2.6(a) and 2.6(b). For a heterogeneous material Batra & Love (2005) regarded a sudden jump in the rate of temperature rise as the ASB initiation criterion, and for a tungsten/nickel-iron composite found its value to be of the order of $10^7\,^\circ$C/s.

Recalling that the temperature is higher where plastic deformation is larger, and assuming that the edge of the ASB is located at the point where the temperature rise is 40% of its peak value, the width of the ASB determined from the numerical data equals $2 \times H \times 0.0020 = 10.32\,\mu$m, which is close to the experimental value of $\sim 10\,\mu$m in Marchand & Duffy (1988). Values of ASB width so computed from solutions with different node numbers are compared in Table 2.1 with those from the MSPH and the FE methods. We note that our definition of the edge of the ASB is arbitrary; one could equally well define it as the point where the plastic strain equals 90% of its peak value at the ASB center. Of course, different definitions of the ASB edge yield varying values of the ASB width.

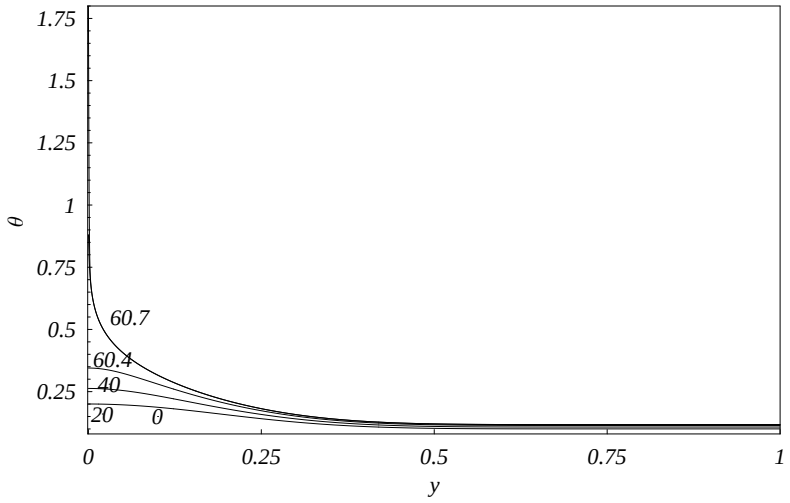

(a)

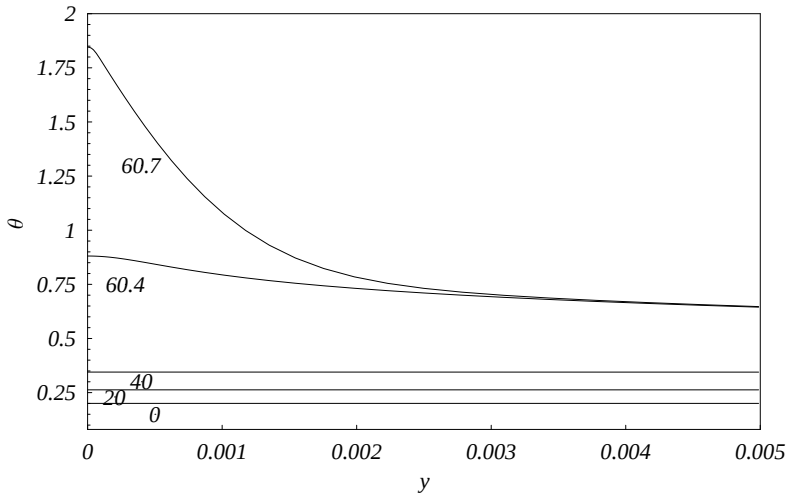

(b)

Figure 2.5: Spatial distribution of the nondimensional temperature rise at times 0, 20, 40, 60.4 and 60.7μs (a) $0 \leq y \leq 1$, (b) $0 \leq y \leq 0.005$.

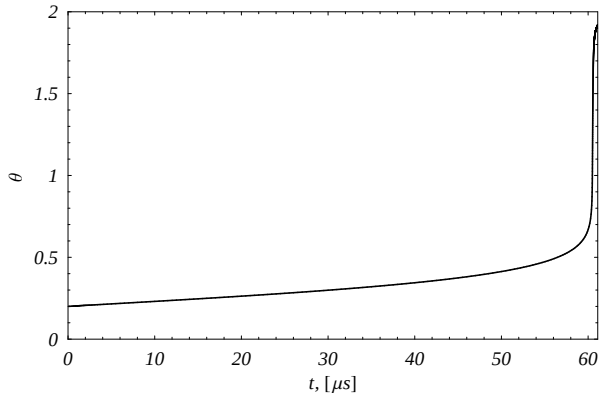

(a)

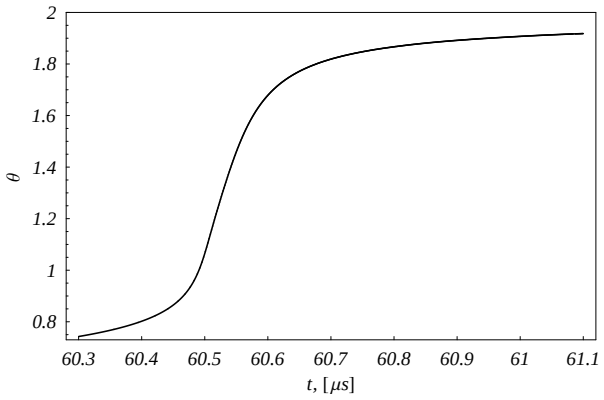

(b)

Figure 2.6: Time history of the temperature rise at the specimen center for (a) $0\mu\text{s} \leq t \leq 61.4\mu\text{s}$, and (b) $60.3\mu\text{s} \leq t \leq 61.1\mu\text{s}$.

2.4.3 Remarks

For the simple shearing problem analyzed here, the Lagrangian FE mesh is not distorted, and the FEM gives very good results. Moreover, because of the Kronecker delta property of the FE bases functions, essential boundary conditions are easily satisfied, and it is possible to integrate in time the semidiscrete system of ordinary differential equations by using the subroutine LSODE, which computes the norms for the corrector iterations and the local truncation error on the nodal values. The MLPG method employing the MLS bases functions, because of the necessity of checking the convergence of the actual nodal values that differ from the nodal unknowns, can not use LSODE. A possibility is to use in the MLPG method multiquadratic radial basis functions (Hardy (1971)) that possess the Kronecker delta property; however, they have been found to work well only with a uniform distribution of nodes.

Whereas adjacent nodes can be placed arbitrarily close to each other in the FEM without affecting significantly the number of iterations required for the solution to converge within one time-step, it is not so in the MLPG and the MSPH methods. For the present formulation of the problem a wide variation in the distance between two adjacent nodes affects noticeably the convergence of the solution.

For two dimensional problems, one can still use a Lagrangian FE mesh, but the mapping from the reference to the current configuration can become singular when elements have been severely distorted; therefore the time step required for stable integration can be reduced immensely and computations cannot be performed in a reasonable CPU time. In the MLPG method, no nodal connectivity is required; therefore one expects that satisfactory results can be computed for two dimensional ASB problems. When the point where an ASB initiates is unknown nodal locations can be adaptively adjusted (Batra & Ko (1988)) to delineate an ASB. This work is left for a future study.

Differences and similarities between the MLPG and the FE methods for a transient linear thermoelastic problem are given in Qian et al. (2004). For the present nonlinear problem the MLPG6 method requires considerably more CPU time than the FEM. The reduction in the data preparation time for 2- and 3-dimensional problems may alleviate the cost associated with the higher CPU time.

2.5 Conclusions

We analyzed, with the meshless local Bubnov-Galerkin method, transient simple shearing deformations of a body made of an elasto-thermo-viscoplastic material. Effects of strain-

hardening, strain-rate hardening, thermal softening, heat conduction and inertia forces have been considered. On the two thermally insulated bounding surfaces of the block, equal and opposite velocity is prescribed, and the corresponding boundary conditions are satisfied by the method of Lagrange multipliers. When a homogeneous solution is perturbed near the center, deformations have been found to localize into a narrow region, $\backsimeq 10\,\mu$m wide, of intense plastic deformation. Results computed with the present method are found to agree very well with those obtained by the finite element and the modified smoothed particle hydrodynamics methods.

Chapter 3

Conclusions

The main contributions of the present work can be summarized as follows.

The pseudoarclength continuation method has been implemented in the MLPG formulation for analyzing the pull-in instability and the symmetry breaking in electrostatically actuated micromembranes. A local symmetric augmented nonlinear weak formulation of the problem has been derived wherein essential boundary conditions are enforced by the method of Lagrange multipliers. The accuracy and the reliability of the proposed technique is assessed through comparisons of the presently computed results with those from other numerical methods.

It is shown that a reduced number of nodes (~ 160) and a few steps (~ 100) in the pseudoarclength continuation method are sufficient for estimating the pull-in parameters and the symmetry-breaking bifurcations with an error of at most 1.53%. The convergence rate of the pseudoarclength continuation method does not vanish when the pull-in state is approached; moreover, since the applied voltage is treated as an unknown, the number of iterations remains bounded.

The effect of the scale on micromembranes has been studied by including the Casimir force in the mathematical model. The effect of the Casimir force on pull-in and symmetry breaking parameters has been investigated. It has been shown that in the miniaturization process there is a minimum size for the device below which the system spontaneously collapses with zero applied voltage. A closed form relation based on a simple lumped model that is suitable for MEMS design is given.

A novel formula for estimating the line to ground capacitance for narrow electrostatically actuated microbeams is proposed. The formula takes into account the finite thickness and the aspect ratio of the beam's cross section. Residual errors in the capacitance with respect to a fully converged solution obtained with the method of moments are less than 0.2%.

The capacitance, and the resulting pull-in instability parameters are compared with the corresponding values derived from other formulas commonly used in the literature, which variously neglect some or all the contributions of the fringing fields.

A one degree-of-freedom model that gives very good values of the pull-in parameters and the fundamental frequency for narrow microbeams has been proposed. It differs from the classical spring-mass model since the nonlinear stiffening due to the axial stress, charge redistribution and fringing fields are considered. Moreover, the complete nonlinear behavior of the electrostatic force is retained and the pull-in voltage and deflections are treated as unknowns, i.e., the pull-in deflection is not empirically chosen as was done in Pamidighantam et al. (2002). It is shown that the pull-in deflections noticeably change with the aspect ratio of the beam cross-section, and can not be a-priori determined. The one degree-of-freedom model results have been validated by comparing them with those obtained by solving the nonlinear one-dimensional boundary-value and the associated eigenvalue problems with the MLPG, and the FE methods in conjunction with the DIPIE algorithm.

The computed pull-in parameters and the fundamental frequency are found to match well with those obtained from the solution of the 3-dimensional problem with the commercial computer code ANSYS. The 3-dimensional simulations are considerably more expensive than those for the proposed one-dimensional distributed model, and the one degree-of-freedom model.

We have also analyzed, with the meshless local Bubnov-Galerkin method, transient simple shearing deformations of a body made of an elasto-thermo-viscoplastic material. Effects of strain-hardening, strain-rate hardening, thermal softening, heat conduction and inertia forces have been considered. Essential boundary conditions in the local symmetric augmented nonlinear weak formulation of the problem are satisfied by the method of Lagrange multipliers. When a homogeneous solution of the problem is perturbed, deformations have been found to localize into a narrow region of intense plastic deformation. Results computed with the present method are found to agree very well with those obtained by the finite element and the modified smoothed particle hydrodynamics methods. This represents the first application of the MLPG method to a transient nonlinear thermoviscoelastoplastic problem involving localization of deformation into a narrow band.

Bibliography

Abdel-Rahman, E. M., Younis, M. I. & Nayfeh, A. H. (2002), 'Characterization of the mechanical behavior of an electrically actuated microbeam', *Journal of Micromechanics and Microengineering* **12**(6), 759–766.

Andreaus, U., Batra, R. C. & Porfiri, M. (2005), 'Vibrations of cracked Euler-Bernoulli beams using Meshless Local Petrov-Galerkin (MLPG) method', *CMES: Computer Modeling in Engineering & Sciences* **9**, 111–132.

ANSYS (2003), *ANSYS Release 8.0 documentation*, ANSYS Inc.

Antman, S. S. (2004), *Nonlinear Problems of Elasticity*, Applied Mathematical Sciences, 2nd edn, Springer-Verlag, New York.

Atluri, S. N., Cho, J. Y. & Kim, H.-G. (1999), 'Analysis of thin beams, using the meshless local Petrov-Galerkin method, with generalized moving least squares interpolations', *Computational Mechanics* **24**, 334–347.

Atluri, S. N. & Shen, S. (2002), 'The meshless local Petrov-Galerkin (MLPG) method: A simple & less-costly alternative to the finite element and boundary element methods', *CMES: Computer Modeling in Engineering & Sciences* **3**(1), 11–51.

Atluri, S. N. & Zhu, T. (1998), 'A new meshless local Petrov-Galerkin (MLPG) approach in computational mechanics', *Computational Mechanics* **22**, 117–127.

Bárcenas, J., Reyes, L. & Esquivel-Sirvent, R. (2005), 'Scaling of micro- and nanodevices actuated by Casimir forces', *Applied Physics Letters* **87**, 263106.

Barke, E. (1988), 'Line-to-ground capacitance calculation for VLSI: A comparison', *IEEE Transactions on Computer-Aided Design of Integrated Circuits and Systems* **7**(2), 295–298.

Bathe, K. J. (1996), *Finite Element Procedures*, Prentice-Hall, Englewood Cliffs, New Jersey.

Batra, R. C. (1987), 'The initiation and growth of, and the interaction among, adiabatic shear bands in simple and dipolar materials', *International Journal of Plasticity* **3**, 75–89.

Batra, R. C. (2005), *Elements of Continuum Mechanics*, AIAA: American Institute of Aeronautics and Astronautics.

Batra, R. C. & Chen, L. (2001), 'Effect of viscoplastic relations on the instability strain, shear band initiation strain, the strain corresponding to the minimum shear band spacing, and the band width in a thermoviscoplastic material', *International Journal of Plasticity* **17**, 1465–1489.

Batra, R. C. & Kim, C. H. (1990), 'Adiabatic shear banding in elastic-viscoplastic nonpolar and dipolar materials', *International Journal of Plasticity* **6**, 127–141.

Batra, R. C. & Ko, K. I. (1988), 'An adaptive mesh refinement technique for the analysis of shear bands in plane strain compression of a thermoviscoplastic solid', *Computational Mechanics* **4**, 741–748.

Batra, R. C. & Love, B. (2005), 'Mesoscale analysis of shear bands in high strain rate deformations of tungsten/nickel-iron composites', *Journal of Thermal Stresses* **28**, 747–782.

Batra, R. C., Porfiri, M. & Spinello, D. (2004), 'Treatment of material discontinuity in two meshless local Petrov-Galerkin (MLPG) formulations of axisymmetric transient heat conduction', *International Journal for Numerical Methods in Engineering* **61**, 2461–2479.

Batra, R. C., Porfiri, M. & Spinello, D. (2006*a*), 'Analysis of electrostatic MEMS using meshless local Petrov-Galerkin (MLPG) method', *Engineering Analysis with Boundary Elements*.

Batra, R. C., Porfiri, M. & Spinello, D. (2006*b*), 'Electromechanical model of electrically actuated narrow microbeams', *Journal of Microelectromechanical Systems*. In press.

Batra, R. C., Porfiri, M. & Spinello, D. (2006*c*), 'Free and forced vibrations of a segmented bar by a meshless local Petrov-Galerkin (MLPG) formulation', *Computational Mechanics*. In press.

Batra, R. C. & Zhang, G. M. (2004), 'Analysis of adiabatic shear bands in elasto-thermo-viscoplastic materials by modified smoothed-particle hydrodynamics (MSPH) method', *Journal of Computational Physics* **201**, 172–190.

Belytschko, T., Lu, Y. Y. & Gu, L. (1994), 'Element-free Galerkin methods', *International Journal for Numerical Methods in Engineering* **37**, 229–256.

Bochobza-Degani, O., Elata, D. & Nemirovsky, Y. (2002), 'An efficient DIPIE algorithm for CAD of electrostatically actuated MEMS devices', *Journal of Microelectromechanical Systems* **11**(5), 612–620.

Borgag, M., Mohideen, U. & Mostepanenko, V. M. (2001), 'New developments in the Casimir effect', *Physics reports* **353**, 1–205.

Bowen, R. M. & Wang, C.-C. (1976), *Introduction to vectors and tensors*, Vol. 2, Plenum Press.

Boyer, T. H. (1968), 'Quantum Electromagnetic Zero-Point Energy of a Conducting Spherical Shell and the Casimir Model for a Charged Particle', *Physical Review* **174**(5), 1764–1776.

Burns, D., Zook, J., Horning, R., Herb, W. & Guckel, H. (1995), 'Sealed-cavity resonant microbeam pressure sensor', *Sensors and Actuators A* **48**(3), 179–186.

Casimir, H. B. G. (1948), 'On the attraction between two perfectly conducting plates', *Proceedings of the Koninklijke Nederlandse Akademie Van Wetenschappen* **51**, 793.

Castañer, L. M. & Senturia, S. D. (1999), 'Speed-energy optimization of electrostatic actuators based on pull-in', *Journal of Microelectromechanical Systems* **8**(3), 290–298.

Chu, P. B., Nelson, P. R., Tachiki, M. L. & Pister, K. S. (1996), 'Dynamics of polysilicon parallel-plate electrostatic actuators', *Sensors and Actuators A* **52**, 216–220.

Collins, E. R. (1992), *Foundations for Microwave Engineering*, 2nd edn, New York: McGraw-Hill.

De, S. K. & Aluru, N. R. (2004), 'Full-Lagrangian schemes for dynamic analysis of electrostatic MEMS', *Journal of Microelectromechanical Systems* **13**(5), 737–758.

Ding, J.-N., Wen, S.-Z. & Meng, Y.-G. (2001), 'Theoretical study of the sticking of a membrane strip in MEMS under the Casimir effect', *Journal of Micromechanics and Microengineering* **11**, 202–208.

Doedel, E., Keller, H. B. & Kernevez, J. P. (1991*a*), 'Numerical analysis and control of bifurcation problems (I) Bifurcation in finite dimensions', *International Journal of Bifurcation and Chaos* **1**, 493–520.

Doedel, E., Keller, H. B. & Kernevez, J. P. (1991*b*), 'Numerical analysis and control of bifurcation problems (II) Bifurcation in infinite dimensions', *International Journal of Bifurcation and Chaos* **1**, 745–772.

Duarte, C. A. M. & Oden, J. T. (1996), 'Hp clouds-an hp meshless method', *Numerical Methods for Partial Differential Equations* **12**, 673–05.

Fargas Marquès, A., Costa Castelló, R. & Shkel, A. M. (2005), Modelling the electrostatic actuation of MEMS: state of the art 2005, Technical report.

Francais, O. & Dufour, I. (1999), 'Normalized abacus for the global behavior of diaphragms: pneumatic, electrostatic, piezoelectric or electromagnetic actuation', *Journal of Modeling and Simulation of Microsystems* **2**, 149–160.

Gabbay, L. D., Mehner, J. E. & Senturia, S. D. (2000), 'Computer-aided generation of nonlinear reduced-order dynamic macromodels II: Non-stress-stiffened case', *Journal of Microelectromechanical Systems* **9**(2), 262–269.

Gear, W. C. (1971), *Numerical initial value problems in ordinary differential equations*, Prentice-Hall, New Jersey.

Gu, Y. T. & Liu, G. R. (2001), 'A meshless local Petrov-Galerkin (MLPG) formulation for static and free vibration analysis of thin plates', *CMES: Computer Modeling in Engineering & Sciences* **2**, 463–476.

Gupta, R. K. & Senturia, S. D. (1997), Pull-in time dynamics as a measure of absolute pressure, *in* 'Proc. IEEE Int. Workshop on Microelectromechanical Systems (MEMS'97)', Nagoya, Japan, pp. 290–294.

Gurtin, M. E. (1981), *An Introduction to Continuum Mechanics*, Academic Press, Inc., San Diego, California.

Hardy, R. L. (1971), 'Multiquadric equations of topography and other irregular surfaces', *Journal of Geophysical Research* **76**, 1905–1915.

Harrington, R. F. (1993), *Field Computation by Moment Methods*, Piscataway, New Jersey.

Harris, B. W., Chen, F. & Mohideen, U. (2000), 'Precision measurement of the Casimir force using gold surfaces', *Physical Review A* **62**(5), 052109.

Hung, E. S. & Senturia, S. D. (1999), 'Extending the travel range of analog-tuned electrostatic actuators', *Journal of Microelectromechanical Systems* **8**(4), 497–505.

Iesan, D. (1987), *Saint-Venant's problem*, Springer-Verlag, New York.

Juneau, T., Unterkofler, K., Seliverstov, T., Zhang, S. & Judy, M. (2003), Dual-axis optical mirror positioning using a nonlinear closed-loop controller, *in* 'TRANSDUCERS, Solid-State Sensors, Actuators and Microsystems, 12th International Conference on', Vol. 1, pp. 560–563.

Kansa, E. J. (1990), 'Multiquadrics-a scattered data approximation scheme with applications to computational fluid dynamics, ii: Solutions to parabolic, hyperbolic and elliptic partial differential equations', *Computer & Mathematics with Applications* **19**, 147–161.

Krylov, S. & Maimon, R. (2004), 'Pull-in dynamics of an elastic beam actuated by continuously distributed electrostatic force', *Journal of Vibration and Acoustics* **126**, 332–342.

Kuang, J.-H. & Chen, C.-J. (2004), 'Dynamic characteristics of shaped micro-actuators solved using the differential quadrature method', *Journal of Micromechanics and Microengineering* **14**(4), 647–655.

Lamoreaux, S. K. (1997), 'Demonstration of the Casimir force in the 0.6 to $6\mu m$ range', *Physical Review Letters* **78**(1), 5–8.

Lamoreaux, S. K. (2005), 'The Casimir force: background, experiments, and applications', *Reports on progress in Physics* **68**, 201–236.

Lancaster, P. & Salkauskas, K. (1981), 'Surfaces generated by moving least squares methods', *Mathematics of Computation* **37**, 141–158.

Landau, L. D. & Lifshitz, E. M. (1986), *Theory of elasticity*, Pergamon Press, New York.

Li, G. & Aluru, N. R. (2003), 'Efficient mixed-domain analysis of electrostatic MEMS', *IEEE Transactions on Computer-Aided Design of Integrated Circuits and Systems* **22**(9), 1228–1242.

Lin, W.-H. & Zhao, Y.-P. (2005), 'Casimir effect on the pull-in parameters of nanometer switches', *Microsystem Technologies* **11**(2-3), 80–85.

Liu, W., Jun, S. & Zhang, Y. (1995), 'Reproducing kernel particle method', *International Journal for Numerical Methods in Fluids* **20**, 1081–1106.

Lucy, L. B. (1977), 'A numerical approach to the testing of the fission hypothesis', *The Astronomical Journal* **82**, 1013–1024.

Mansfield, E. H. (1989), *The bending & stretching of plates*, 2nd edn, Cambridge University Press, Cambridge; New York. Chapter 9.

Marchand, A. & Duffy, J. (1988), 'An experimental study of the formation process of adiabatic shear bands in a structural steel', *Journal of the Mechanics and Physics of Solids* **36**, 251–283.

Meijs, N. V. D. & Fokkema, J. T. (1984), 'VLSI circuit reconstruction from mask topology', *Integration* **2**(2), 85–119.

Melenk, J. M. & Babuska, I. (1996), 'The partition of unity finite element method: Basic theory and applications', *Computer Methods in Applied Mechanics and Engineering* **139**, 289–314.

Mura, T. & Koya, T. (1992), *Variational methods in mechanics*, Oxford Univ. Press, New York.

Naghdi, P. M. (1972), *The Theory of Shells and Plates*, Vol. VIa/2 of *Handbuch der Physik*, Springer-Verlag, Berlin-New York, pp. 425–640.

Naghdi, P. M. (1980), Finite deformations of rods and shells, *in* D. E. Carlson & R. T. Shield, eds, 'Proceedings of the IUTAM Symposium on Finite Elasticity', Martinus Nijhoff Publishers, The Hague/Boston/London, pp. 47–103.

Nathanson, H. C., Newell, W. E., Wickstrom, R. A. & Davis, J. R. (1967), 'The resonant gate transistor', *IEEE Transactions on Electron Devices* **14**(3), 117–133.

Nayfeh, A. H. & Younis, M. I. (2005), 'Dynamics of MEMS resonators under superharmonic and subharmonic excitations', *Journal of Micromechanics and Microengineering* **15**, 1840–1847.

Nayroles, B., Touzot, G. & Villon, P. (1992), 'Generalizing the finite element method: diffuse approximation and diffuse elements', *Computational Mechanics* **10**, 307–318.

Newell, W. (1968), 'Miniaturization of tuning forks', *Science* **161**(3848), 1320–1326.

Ng, T. Y., Jiang, T. Y., Lam, K. Y. & Reddy, J. N. (2004), 'A coupled field study on the non-linear dynamic characteristics of an electrostatic micropump', *Journal of Sound and Vibration* **273**, 989–1006.

Nguyen, C. T. C., Katehi, L. P. B. & Rebeiz, G. M. (1998), 'Micromachined devices for wireless communications', *Proceedings of the IEEE* **86**(8), 1756–1768.

Osterberg, P. M. & Senturia, S. D. (1997), 'M-TEST: A test chip for MEMS material property measurement using electrostatically actuated test structures', *Journal of Microelectromechanical Systems* **6**(2), 107–118.

Palasantzas, G. & De Hosson, J. T. M. (2005), 'Pull-in characteristics of electromechanical switches in the presence of Casimir forces: Influence of self-affine surface roughness', *Physical Review B* **72**, 115426.

Palmer, H. B. (1937), 'Capacitance of a parallel-plate capacitor by the Schwartz-Christoffel transformation', *Transactions of the American Institute of Electrical Engineers* **56**(3), 363–366.

Pamidighantam, S., Puers, R., Baert, K. & Tilmans, H. A. C. (2002), 'Pull-in voltage analysis of electrostatically actuated beam structures with fixed-fixed and fixed-free end conditions', *Journal of Micromechanics and Microengineering* **12**(4), 458–464.

Pelesko, J. A. (2002), 'Mathematical modeling of electrostatics MEMS with tailored dielectric properties', *SIAM Journal of Applied Mathematics* **62**(3), 888–908.

Pelesko, J. A. & Bernstein, D. H. (2002), *Modeling MEMS and NEMS*, Chapman & Hall. Chapter 7.

Pelesko, J. A., Bernstein, D. H. & McCuan, J. (2003), Symmetry and symmetry breaking in electrostatic MEMS, *in* 'Proceedings of Modeling and Simulation of Microsystems', pp. 304–307.

Pelesko, J. A. & Chen, X. Y. (2003), 'Electrostatic deflections of circular elastic membranes', *Journal of Electrostatics* **57**, 1–12.

Pelesko, J. & Triolo, A. (2001), 'Nonlocal problems in MEMS device control', *Journal of Engineering Mathematics* **41**(4), 345–366.

Press, W. H., Teukolsky, S. A., Vetterling, W. T. & Flannery, B. P. (1992), *Numerical Recipes in C. The art of scientific computing, Second Edition*, Cambridge University Press, New York.

Qian, L. F., Batra, R. C. & Chen, L. M. (2004), 'Analysis of cylindrical bending thermoelastic deformations of functionally graded plates by a meshless local Petrov-Galerkin method', *Computational Mechanics* **33**, 263–273.

Radhakrishnan, K. & Hindmarsh, A. C. (1993), Description and use of LSODE, the Livermore solver for ordinary differential equations, Technical report, Lawrence Livermore National Laboratory Report UCRL-ID-113855.

Raju, I. S. & Phillips, D. R. (2003), 'Further developments in the MLPG method for beam problems', *CMES: Computer Modeling in Engineering & Sciences* **4**(1), 141–159.

Rhoads, J. F., Shaw, S. W. & Turner, K. L. (2006), 'The nonlinear response of resonant microbeam systems with purely-parametric electrostatic actuation', *Journal of Micromechanics and Microengineering* **16**, 890–899.

Senturia, S. D., Aluru, N. R. & White, J. (1997), 'Simulating the behavior of MEMS devices: Computational methods and needs', *IEEE Computational Science and Engineering* **4**(1), 30–43.

Senturia, S. D., Harris, R. M., Johnson, B. P., Kim, S., Nabors, K., Shulman, M. A. & White, J. K. (1992), 'A computer-aided design system for microelectromechanical systems (MEMCAD)', *Journal of Microelectromechanical Systems* **1**(1), 3–13.

Serry, F. M., Walliser, D. & Maclay, G. J. (1998), 'The role of the Casimir effect in the static deflection and stiction of membrane strips in microelectromechanical systems (MEMS)', *Journal of Applied Physics* **84**(5), 2501–2506.

Shapoorabadi, R. J. & Kirk, A. G. (2004), Comparison of three finite element models for analysis of MEMS micromirrors, *in* 'Proceedings SPIE, International Conference on Applications of Photonic Technology, Photonics North', Vol. 5577, pp. 849–859.

Shi, F., Ramesh, P. & Mukherjee, S. (1995), 'On the application of 2D potential theory to electrostatic simulation', *Communications in Numerical Methods in Engineering* **11**, 691–701.

Shi, F., Ramesh, P. & Mukherjee, S. (1996), 'Dynamic analysis of micromicroelectromechanical systems', *International Journal for Numerical Methods in Engineering* **39**, 4119–4139.

Sukenik, C. I., Boshier, M. G., Cho, D., Sandoghdar, V. & Hinds, E. A. (1993), 'Measurement of the Casimir-Polder force', *Physical Review Letters* **70**(5), 560–563.

Sukumar, N., Moran, B. & Belytschko, T. (1998), 'The natural element method in solid mechanics', *International Journal for Numerical Methods in Engineering* **43**, 839–887.

Taylor, G. I. (1968), 'The coalescence of closely spaced drops when they are at different electric potentials', *Proceedings of the Royal Society A* **306**, 423–434.

Teymoory, M. & Abbaspour-Sany, E. (2002), A novel electrostatic micromachined pump for drug delivery systems, *in* 'Semiconductor Electronics 2002. Proceedings. ICSE 2002. IEEE International Conference on'.

Tilmans, H. A. & Legtenberg, R. (1994*a*), 'Electrostatically driven vacuum-encapsulated polysilicon resonators: Part I. Design and fabrication', *Sensors and Actuators A* **45**, 57–66.

Tilmans, H. A. & Legtenberg, R. (1994*b*), 'Electrostatically driven vacuum-encapsulated polysilicon resonators: Part II. Theory and performance', *Sensors and Actuators A* **45**(1), 67–84.

Timoshenko, S. (1970), *Theory of Elasticity*, 3rd edn, McGraw-Hill Companies.

Wendland, H. (1995), 'Piecewise polynomial, positive definite and compactly supported radial basis functions of minimal degree', *Advances in Computational Mathematics* **4**, 389–396.

Whittaker, E. T. & Watson, G. N. (1963), *A Course of Modern Analysis*, 4th edn, Cambridge University Press, London.

Xie, W. C., Lee, H. P. & Lim, S. P. (2003), 'Nonlinear dynamic analysis of MEMS switches by nonlinear modal analysis', *Nonlinear Dynamics* **31**, 243–256.

Younis, M. I., Abdel-Rahman, E. M. & Nayfeh, A. H. (2003), 'A reduced-order model for electrically actuated microbeam-based MEMS', *Journal of Microelectromechanical Systems* **12**(5), 672–680.

Younis, M. I. & Nayfeh, A. H. (2003), 'A study of the nonlinear response of a resonant microbeam to an electric actuation', *Nonlinear Dynamics* **31**, 91–117.

Zhang, G. M. & Batra, R. C. (2004), 'Modified smoothed particle hydrodynamics method and its application to transient problems', *Computational Mechanics* **34**, 137–146.

Zhao, X., Abdel-Rahman, E. M. & Nayfeh, A. H. (2004), 'A reduced-order model for electrically actuated microplates', *Journal of Micromechanics and Microengineering* **14**(7), 900–906.

Zhu, T., Zhang, J. D. & Atluri, S. N. (1998), 'A local boundary integral equation (LBIE) method in computational mechanics, and a meshless discretization approach', *Computational Mechanics* **21**, 223–235.

Appendix A

MLS and GMLS approximations

A.1 Moving Least Square (MLS) basis functions

We use the moving least squares approximation (MLS) proposed by Lancaster & Salkauskas (1981), that allows for an accurate reconstruction of a given trial function on the entire domain, from the knowledge of its values at some, suitably chosen, scattered points.

Consider a continuous scalar function u defined on the d-dimensional connected domain Ω. The generic point in Ω is indicated by $\mathbf{x}$, and its coordinates in a rectangular Cartesian coordinate system are $x^1, x^2, \ldots, x^d$. The (fictitious) nodal values at N scattered points $\mathcal{N} = \{\mathbf{x}_1, \mathbf{x}_2, \ldots \mathbf{x}_N\}$ in $\bar{\Omega}$ are collected into the N-vector $\hat{\mathbf{u}} = [\hat{u}_1 \ \cdots \ \hat{u}_N]^{\mathrm{T}}$, where the superscript T indicates transposition. The global approximation u^h of u in Ω is defined by

$$u(\mathbf{x}) \simeq u^h(\mathbf{x}) = \mathbf{p}^{\mathrm{T}}(\mathbf{x})\, \mathbf{a}(\mathbf{x}), \quad \mathbf{x} \in \Omega, \tag{A.1}$$

where

$$\mathbf{p}^{\mathrm{T}}(\mathbf{x}) = [p_1(\mathbf{x}) \ \ p_2(\mathbf{x}) \ \ \cdots \ \ p_q(\mathbf{x})], \tag{A.2}$$

is a monomial basis. For example in the one-dimensional problem a complete monomial basis of order 2 is

$$\mathbf{p}^{\mathrm{T}}(\mathbf{x}) = \begin{bmatrix} 1 & x^1 \end{bmatrix}, \qquad \text{linear basis,} \qquad q = 2, \tag{A.3}$$

while for a two-dimensional problem a complete monomial basis of order 2 is

$$\mathbf{p}^{\mathrm{T}}(\mathbf{x}) = \begin{bmatrix} 1 & x^1 & x^2 \end{bmatrix}, \qquad \text{linear basis,} \qquad q = 3. \tag{A.4}$$

The q-vector $\mathbf{a}(\mathbf{x}) = [a_1(\mathbf{x}) \ \cdots \ a_q(\mathbf{x})]^{\mathrm{T}}$ is composed of indeterminate coefficients, which vary with the point $\mathbf{x}$ of the domain Ω. At each location $\bar{\mathbf{x}}$ in Ω these coefficients are determined by a local least square approximation of $u(\mathbf{x})$ on a small neighborhood $\Omega_{\bar{\mathbf{x}}}$ of $\bar{\mathbf{x}}$. The local approximation $u_{\bar{\mathbf{x}}}(\mathbf{x})$ is defined by

$$u(\mathbf{x}) \simeq u_{\bar{\mathbf{x}}}(\mathbf{x}) = \mathbf{p}^{\mathrm{T}}(\mathbf{x})\, \mathbf{a}(\bar{\mathbf{x}}), \quad \mathbf{x} \in \Omega_{\bar{\mathbf{x}}} \subset \Omega. \tag{A.5}$$

Therefore, in a small neighborhood of a generic point $\bar{\mathbf{x}}$ the coefficients a_i are treated as unknown constants of the classical polynomial least square approximation, and they are determined by minimizing the following functional $J_{\bar{\mathbf{x}}}$ representing the weighted discrete L^2 error norm

$$J_{\bar{\mathbf{x}}}(\mathbf{a}) = \sum_{i=1}^{N} W_i(\bar{\mathbf{x}}) \left[u_{\bar{\mathbf{x}}}(\mathbf{x}_i) - \hat{u}_i\right]^2. \tag{A.6}$$

The function W_i, the weight function of node i, is a continuous positive function which equals 1 at $\mathbf{x} = \mathbf{x}_i$ and has a compact support.

At a given location $\bar{\mathbf{x}}$ only few terms in summation (A.6) are nonzero since supports of weight functions W_i are much smaller than the domain Ω. This reduces memory requirements when implementing the algorithm in a computer code, and strengthens the local character of the MLS approximation. We denote by n the number of nonvanishing terms at the point $\bar{\mathbf{x}}$ and emphasize that n is a function of $\bar{\mathbf{x}}$. Lower bounds for the diameters of supports of weight functions are established below to assure the regularity of the MLS basis functions.

The functional $J_{\bar{\mathbf{x}}}$ may be conveniently rewritten in matrix notation as follows:

$$J_{\bar{\mathbf{x}}}(\mathbf{a}) = (\mathbf{P}\mathbf{a} - \hat{\mathbf{u}})^{\mathrm{T}} \mathbf{W}(\bar{\mathbf{x}}) (\mathbf{P}\mathbf{a} - \hat{\mathbf{u}}), \tag{A.7}$$

where $\mathbf{P}$ is a $(N \times q)$ matrix of real numbers:

$$\mathbf{P}^{\mathrm{T}} = \left[\mathbf{p}^{\mathrm{T}}(\mathbf{x}_1) \ \cdots \ \mathbf{p}^{\mathrm{T}}(\mathbf{x}_N)\right] \tag{A.8}$$

and $\mathbf{W}$ is a $(N \times N)$ diagonal matrix defined by

$$\mathbf{W}(\bar{\mathbf{x}}) = \mathrm{DIAG}\left[W_1(\bar{\mathbf{x}}) \ \cdots \ W_N(\bar{\mathbf{x}})\right]. \tag{A.9}$$

The local nature of the MLS approximation requires that only n terms of the matrix $\mathbf{W}$ are different from zero.

The stationarity of $J_{\bar{\mathbf{x}}}$ with respect of $\mathbf{a}$ yields

$$\mathbf{A}(\bar{\mathbf{x}}) \mathbf{a}(\bar{\mathbf{x}}) = \mathbf{B}(\bar{\mathbf{x}}) \hat{\mathbf{u}}, \tag{A.10}$$

where the $(q \times q)$ and the $(q \times N)$ matrices $\mathbf{A}$ and $\mathbf{B}$ are defined by

$$\mathbf{A}(\bar{\mathbf{x}}) = \mathbf{P}^{\mathrm{T}} \mathbf{W}(\bar{\mathbf{x}}) \mathbf{P}, \qquad \mathbf{B}(\bar{\mathbf{x}}) = \mathbf{P}^{\mathrm{T}} \mathbf{W}(\bar{\mathbf{x}}). \tag{A.11}$$

We note that matrices $\mathbf{A}$ and $\mathbf{B}$ depend on the spatial coordinate $\bar{\mathbf{x}}$ only through the weight functions, since $\mathbf{P}$ is a matrix of real numbers. Solving for $\mathbf{a}$ in Eq. (A.10), we obtain

$$\mathbf{a}(\bar{\mathbf{x}}) = \mathbf{A}(\bar{\mathbf{x}})^{-1} \mathbf{B}(\bar{\mathbf{x}}) \hat{\mathbf{u}}. \tag{A.12}$$

Substituting this expression for $\mathbf{a}$ in the global approximation (A.1) we get the MLS approximation

$$u^h(\mathbf{x}) = \mathbf{p}^{\mathrm{T}}(\mathbf{x})\,\mathbf{A}^{-1}(\mathbf{x})\,\mathbf{B}(\mathbf{x})\,\hat{\mathbf{u}}, \tag{A.13}$$

which, upon introducing the vector of basis functions $\boldsymbol{\varphi}(\mathbf{x})$, can be expressed as

$$u^h(\mathbf{x}) = \boldsymbol{\varphi}(\mathbf{x})^{\mathrm{T}}\,\hat{\mathbf{u}}, \tag{A.14}$$

with

$$\boldsymbol{\varphi} = \left[\varphi_1 \;\; \cdots \;\; \varphi_N\right]^{\mathrm{T}}. \tag{A.15}$$

The basis functions are directly computed from Eqs. (A.11) and (A.13) by using

$$\boldsymbol{\varphi}(\mathbf{x}) = \mathbf{p}(\mathbf{x})^{\mathrm{T}}\,\mathbf{A}^{-1}(\mathbf{x})\,\mathbf{P}^{\mathrm{T}}\mathbf{W}(\mathbf{x}). \tag{A.16}$$

We emphasize that for an arbitrary node $\mathbf{x}_i$ the fictitious nodal value does not equal the value at the node of the function being interpolated, i.e.

$$u^h(\mathbf{x}_i) \neq \hat{u}_i. \tag{A.17}$$

Indeed, the nodal values of the approximating function collected in the vector $\mathbf{u}^h$ are related to $\hat{\mathbf{u}}$ by

$$\mathbf{u}^h = \boldsymbol{\Phi}\hat{\mathbf{u}}, \tag{A.18}$$

where the non-diagonal matrix $\boldsymbol{\Phi}$ is defined by

$$[\boldsymbol{\Phi}]_{ij} = \varphi_j(\mathbf{x}_i). \tag{A.19}$$

The MLS expansion in (A.14) is well defined only if matrix $\mathbf{A}$ in (A.11) is non-singular. It can be seen that this is the case if and only if the rank of the $n \times q$ matrix $\mathbf{P}_{\bar{\mathbf{x}}}$, obtained from $\mathbf{P}$ by deleting rows corresponding to those nodes whose weight function vanishes at $\bar{\mathbf{x}}$, equals q. Obviously, a necessary condition for a well-defined MLS approximation is that at least q nodal weight functions do not vanish at $\bar{\mathbf{x}}$. However, this condition is not sufficient (see Atluri et al. (1999)).

The smoothness of the MLS trial functions is completely determined by the smoothness of the weight functions, since the polynomial basis is infinitely differentiable. If α indicates the minimum order of differentiability of weight functions associated with all nodes in Ω , then from (A.11) it is evident that the trial functions are at least α times differentiable. In the following, we consider weight functions that are at least once continuously differentiable everywhere in Ω.

In the analysis, the computation of derivative of MLS basis functions in (A.16) is needed. To save computational effort, it is better to compute explicitly the first derivative of the inverse of the matrix $\mathbf{A}$ with respect to the coordinate $\mathbf{x}$ from the identity

$$\mathbf{A}\mathbf{A}^{-1} = \mathbf{1}. \tag{A.20}$$

Hence

$$\frac{\partial \mathbf{A}^{-1}}{\partial x^i} = -\mathbf{A}^{-1}\frac{\partial \mathbf{A}}{\partial x^i}\mathbf{A}^{-1}. \tag{A.21}$$

Therefore, only the knowledge of weight functions and their derivatives is needed to compute the derivative of the inverse of $\mathbf{A}$ appearing in (A.16).

In the literature (see e.g. Atluri & Shen (2002)), fourth-order spline and Gauss weight functions are widely used. For the shear band problem in Chapter 2 we employ the fourth-order spline weight function:

$$W_i\left(x^1\right) = \begin{cases} 1 - 6\left(\dfrac{d_i}{r_i}\right)^2 + 8\left(\dfrac{d_i}{r_i}\right)^3 - 3\left(\dfrac{d_i}{r_i}\right)^4, & d_i < r_i \\ 0, & d_i \geq r_i \end{cases}, \tag{A.22}$$

where $d_i = |x^1 - x_i|$ is the distance from node x_i to point x^1, and r_i is the radius of support of the weight function W_i. For two dimensional MEMS problems in Chapter 1 we employ Gauss weight functions:

$$W_i\left(\mathbf{x}\right) = \begin{cases} \dfrac{\exp\left[-\left(d_i/c_i\right)^{2k}\right] - \exp\left[-\left(r_i/c_i\right)^{2k}\right]}{1 - \exp\left[-\left(r_i/c_i\right)^{2k}\right]}, & d_i < r_i \\ 0, & d_i \geq r_i \end{cases} \tag{A.23}$$

where c_i and k are parameters controlling the shape and, as in Eq. (A.22), $d_i = |\mathbf{x} - \mathbf{x}_i|$ is the distance from node $\mathbf{x}_i$ to point $\mathbf{x}$, and r_i is the radius of the support.

A.2 Generalized Moving Least Squares (GMLS) basis functions

The generalized moving least squares approximation (GMLS) proposed by Atluri et al. (1999) generalizes that proposed in Lancaster & Salkauskas (1981) by allowing for the accurate reconstruction of a given trial function on the entire domain, from the knowledge of its values and of its first derivatives at some, suitably chosen, scattered points.

Consider the function u having continuous first derivative on the domain Ω. The (fictitious) nodal values and (fictitious) derivatives at the scattered points $\mathcal{N} = \{x_1, x_2, ..., x_N\}$ in Ω are collected into the two N-vectors $\hat{\mathbf{w}} = \left[\hat{w}_1 \cdots \hat{w}_N\right]^{\mathrm{T}}$ and $\hat{\boldsymbol{\theta}} = \left[\hat{\theta}_1 \cdots \hat{\theta}_N\right]^{\mathrm{T}}$ respectively, where the superscript T indicates transposition. The global approximation u^h on Ω is defined as

$$u\left(x\right) \simeq u^h\left(x\right) = \mathbf{p}^{\mathrm{T}}\left(x\right)\mathbf{a}\left(x\right), \quad x \in \Omega, \tag{A.24}$$

where

$$\mathbf{p}^{\mathrm{T}}\left(x\right) = \begin{bmatrix} 1 & x & x^2 & \cdots & x^{m-1} \end{bmatrix} \tag{A.25}$$

is a complete monomial basis of degree $m-1$.

The m-vector $\mathbf{a}(x) = [a_1(x) \ \cdots \ a_m(x)]^{\mathrm{T}}$ is composed of indeterminate coefficients, which vary with the abscissa x on the domain Ω. At each location $\bar{x}$ on Ω these coefficients are determined by a local least square approximation of $u(x)$ on a small neighborhood $\Omega_{\bar{x}}$ of $\bar{x}$. The local approximation $u_{\bar{x}}(x)$ is defined by

$$u(x) \simeq u_{\bar{x}}(x) = \mathbf{p}^{\mathrm{T}}(x)\,\mathbf{a}(\bar{x}), \quad x \in \Omega_{\bar{x}} \subset \Omega. \tag{A.26}$$

In a small neighborhood of a generic point $\bar{x}$ the coefficients a_i are treated as the unknown constants of a classical polynomial least square approximation. Therefore, they are determined by minimizing the functional $J_{\bar{x}}$ representing the weighted discrete H^1 error norm (see, e.g., Atluri et al. (1999)), and defined by

$$J_{\bar{x}}(\mathbf{a}) = \sum_{i=1}^{N} W_i^{(w)}(\bar{x})\,[u_{\bar{x}}(x_i) - \hat{w}_i]^2 + \sum_{i=1}^{N} W_i^{(\theta)}(\bar{x})\left[u'_{\bar{x}}(x_i) - \hat{\theta}_i\right]^2, \tag{A.27}$$

where the superimposed prime indicates derivative with respect to the x coordinate. Functions $W_i^{(w)}$ and $W_i^{(\theta)}$ are weight functions of node i and are characterized by the following properties: (i) they are continuous, (ii) they equal one at $x = x_i$, (iii) they vanish when $x \notin \left(x_i - R_i^{(w)}, x_i + R_i^{(w)}\right)$ and $x \notin \left(x_i - R_i^{(\theta)}, x_i + R_i^{(\theta)}\right)$, respectively, and are positive elsewhere. The parameters $R_i^{(w)}$ and $R_i^{(\theta)}$ measure semi-supports of the weight functions $W_i^{(w)}$ and $W_i^{(\theta)}$ respectively.

At a given location $\bar{x}$ only a few terms in summation (A.27) do not vanish since the supports $R_i^{(w)}$ and $R_i^{(\theta)}$ of the weight functions $W_i^{(w)}$ and $W_i^{(\theta)}$ are much smaller than the size of Ω. This is used to reduce the memory allocations when implementing the algorithm in a computer code. Lower bounds of $R_i^{(w)}$ and $R_i^{(\theta)}$ are stated in Atluri et al. (1999) for assuring the regularity of the GMLS basis functions.

The stationarity of $J_{\bar{x}}$ with respect of $\mathbf{a}$ yields

$$\mathbf{A}(\bar{x})\,\mathbf{a}(\bar{x}) = \mathbf{B}(\bar{x}) \begin{bmatrix} \hat{\mathbf{w}} \\ \hat{\boldsymbol{\theta}} \end{bmatrix}, \tag{A.28}$$

where the (m,m) and the (m,N) matrices $\mathbf{A}$ and $\mathbf{B}$ are defined by

$$\mathbf{A}(\bar{x}) = \mathbf{P}^{\mathrm{T}}\mathbf{W}^{(w)}(\bar{x})\,\mathbf{P} + (\mathbf{P}')^{\mathrm{T}}\mathbf{W}^{(\theta)}(\bar{x})\,\mathbf{P}', \tag{A.29a}$$

$$\mathbf{B}(\bar{x}) = \begin{bmatrix} \mathbf{P}^{\mathrm{T}}\mathbf{W}^{(w)}(\bar{x}) & (\mathbf{P}')^{\mathrm{T}}\mathbf{W}^{(\theta)}(\bar{x}) \end{bmatrix}. \tag{A.29b}$$

Here $\mathbf{W}^{(w)}$ and $\mathbf{W}^{(\theta)}$ are (N,N) diagonal matrices defined by

$$\mathbf{W}^{(w)}(\bar{x}) = \mathrm{DIAG}\begin{bmatrix} W_1^{(w)}(\bar{x}) & \cdots & W_N^{(w)}(\bar{x}) \end{bmatrix}, \tag{A.30}$$

$$\mathbf{W}^{(\theta)}(\bar{x}) = \mathrm{DIAG}\begin{bmatrix} W_1^{(\theta)}(\bar{x}) & \cdots & W_N^{(\theta)}(\bar{x}) \end{bmatrix}, \tag{A.31}$$

and $\mathbf{P}$, $\mathbf{P}'$ are (N, m) matrices of real numbers defined by

$$\mathbf{P}^{\mathrm{T}} = \left[\begin{array}{ccc} \mathbf{p}(x_1) & \cdots & \mathbf{p}(x_N) \end{array} \right], \quad (\mathbf{P}')^{\mathrm{T}} = \left[\begin{array}{ccc} \mathbf{p}'(x_1) & \cdots & \mathbf{p}'(x_N) \end{array} \right]. \tag{A.32}$$

Solving (A.10) for $\mathbf{a}(\bar{x})$ and substituting for $\mathbf{a}(\bar{x})$ in the global approximation (A.26) we obtain the GMLS approximation

$$u^h(x) = \boldsymbol{\psi}^{(w)}(x)^{\mathrm{T}} \hat{\mathbf{w}} + \boldsymbol{\psi}^{(\theta)}(x)^{\mathrm{T}} \hat{\boldsymbol{\theta}}, \tag{A.33}$$

where the vectors of basis functions $\boldsymbol{\psi}^{(w)}(x)$ and $\boldsymbol{\psi}^{(\theta)}(x)$ are given by

$$\boldsymbol{\psi}^{(w)}(x) = \mathbf{p}(x)^{\mathrm{T}} \mathbf{A}^{-1}(x) \mathbf{P}^{\mathrm{T}} \mathbf{W}^{(w)}(x), \tag{A.34a}$$

$$\boldsymbol{\psi}^{(\theta)}(x) = \mathbf{p}^{\mathrm{T}}(x) \mathbf{A}^{-1}(x) (\mathbf{P}')^{\mathrm{T}} \mathbf{W}^{(\theta)}(x). \tag{A.34b}$$

It is convenient to group the nodal variables and the GMLS basis functions in the $2N$-vectors

$$\hat{\mathbf{u}} = \left[\hat{\mathbf{w}} \;\; \hat{\boldsymbol{\theta}} \right]^{\mathrm{T}}, \qquad \boldsymbol{\psi} = \left[\boldsymbol{\psi}^{(w)} \;\; \boldsymbol{\psi}^{(\theta)} \right]. \tag{A.35}$$

The smoothness of the GMLS trial functions is completely determined by the smoothness of the weight functions, since the monomial basis is infinitely differentiable. If $\alpha - 1$ indicates the minimum order of differentiability of all weight functions, then from Eqs. (A.29) and (A.34) it is evident that the trial functions will be at least $\alpha - 1$ times differentiable.

In the present work, following Atluri et al. (1999), and Raju & Phillips (2003), we assume the same $C^{\alpha-1}(\Omega)$ structure for all weight functions and no distinction is made between the deflection and the rotation weight functions, namely

$$W_i^{(w)}(x) = W_i^{(\theta)}(x) = \begin{cases} \left(1 - \left(\frac{x - x_i}{R_i}\right)^2\right)^{\alpha} & \text{if } x \in (x_i - R_i, x_i + R_i) \\ 0 & \text{if } x \notin (x_i - R_i, x_i + R_i) \end{cases}. \tag{A.36}$$

Appendix B

Confocal elliptic coordinates

For elliptic MEMS problems solved with the finite difference method, elliptic coordinates (ξ^1, ξ^2) are introduced. They are related to rectangular Cartesian coordinates (x^1, x^2) by

$$\begin{array}{l} x^1 = c\cosh\xi^1\cos\xi^2 \\ x^2 = c\sinh\xi^1\sin\xi^2 \end{array} \quad , \qquad \xi^1 \in \left[0, \operatorname{arctanh}\left(\frac{b}{a}\right)\right], \quad \xi^2 \in [0, 2\pi)\,, \tag{B.1}$$

where $c^2 = a^2 - b^2$, and a and b are the semi-major and the semi-minor axes of the ellipse, respectively. Thus the elliptical domain becomes a strip. Curves $\xi^1 = \text{const.}$ are confocal ellipses with the focal points located in $x^1 = \pm c$; similarly, curves $\xi^2 = \text{const.}$ are confocal hyperbolas.

In elliptical coordinates, the Laplacian of a scalar field $u : [0, \operatorname{arctanh}(b/a)] \times [0, 2\pi) \to \mathbb{R}$ becomes (see Bowen & Wang (1976))

$$\triangle u \equiv \left[\frac{2}{c^2\left(\cosh 2\xi^1 - \cos 2\xi^2\right)}\left(\frac{\partial^2}{\left(\partial\xi^1\right)^2} + \frac{\partial^2}{\left(\partial\xi^2\right)^2}\right)\right] u. \tag{B.2}$$

Appendix C

Method of Moments

The potential ϕ for an arbitrary charge distribution per unit surface $\sigma^\star$ is given by

$$\phi\left(y,z\right)=-\frac{1}{2\pi\epsilon_0\epsilon_{\mathrm{r}}}\int_\Gamma\sigma^\star\left(\theta,\zeta\right)\ln\left\|\left(y,z\right)-\left(\theta,\zeta\right)\right\|\,\mathrm{d}\Gamma+C_{\mathrm{T}},\tag{C.1}$$

where $\left\|\left(y,z\right)-\left(\theta,\zeta\right)\right\|=\sqrt{\left(y-\theta\right)^2+\left(z-\zeta\right)^2}$ is the distance from the source point (θ,ζ) to the observation point (y,z), Γ is the overall boundary of the conductors, and C_{T} is a constant that may be neglected since it does not affect the charge distribution. Boundary conditions on the top and the bottom rectangle, say Γ^1 and Γ^2, are $\phi=\bar{V}$ and $\phi=0$ respectively (see Fig. 1.29). The boundary of each plate is subdivided into small elements and the charge density $\sigma_i^\star$ is assumed to be constant in element i (piecewise constant basis functions). For convenience we use the same mesh of N_{e} elements for the two identical rectangles. By substituting the charge approximation into (C.1) and by imposing the boundary conditions at the geometric centers P_i of the $2N_{\mathrm{e}}$ elements (collocation method), we obtain the following linear system of $2N_{\mathrm{e}}$ equations in $2N_{\mathrm{e}}$ unknowns collected in the vector $\boldsymbol{\sigma}^\star$:

$$\mathbf{L}\,\boldsymbol{\sigma}^\star=\mathbf{g}.\tag{C.2}$$

The generic entry of the coefficient matrix $\mathbf{L}$ is given by:

$$i=j:\ \left[\mathbf{L}\right]_{ii}=\Delta\Gamma_i\left(\ln\left(\Delta\Gamma_i/2\right)-1\right),\tag{C.3a}$$

$$\begin{aligned}i\neq j:\ \left[\mathbf{L}\right]_{ij}=&-\Delta\Gamma_j\left(1-\ln\left\|P_j^{(2)}-P_i\right\|\right)-\left\|P_j^{(1)}-P_i\right\|\cos\beta_{ij}\\&\times\ln\frac{\left\|P_j^{(2)}-P_i\right\|}{\left\|P_j^{(1)}-P_i\right\|}+\alpha_{ij}\left\|P_j^{(1)}-P_i\right\|\sin\beta_{ij}\end{aligned}\tag{C.3b}$$

where $\Delta\Gamma_i$ is the length of the i-th element, $P_j^{(1)}$ and $P_j^{(2)}$ are the extrema of the j-th element, β_{ij} is the angle between the segments $P_j^{(1)}P_j^{(2)}$ and $P_j^{(1)}P_i$, and α_{ij} is the angle between the

segments $P_i P_j^{(2)}$ and $P_i P_j^{(1)}$. We note that these angles can be computed by using Carnot's theorem. The element of the vector $\mathbf{g}$ equals $\bar{V}$ if it refers to an element of Γ^1 and 0 if it refers to an element of Γ^2. From the knowledge of the distributed charge per unit surface area, the charge stored per unit line in each plate may be directly computed and the capacitance per unit line estimated.

Appendix D

Functions χ

Expressions for functions χ appearing in Eqs. (2.34) are given below. For $\Lambda^h(\hat{\mathbf{u}}) > 0$

$$\chi^{22}(\hat{\mathbf{u}}) = \frac{a}{bm}\left(1 - a\boldsymbol{\varphi}^{\mathrm{T}}\hat{\boldsymbol{\vartheta}}\right)^{-1-\frac{1}{m}}\left(\boldsymbol{\varphi}^{\mathrm{T}}\hat{\mathbf{s}}\right)^{1+\frac{1}{m}}\left(1 + \frac{\boldsymbol{\varphi}^{\mathrm{T}}\hat{\boldsymbol{\psi}}}{\psi_0}\right)^{-\frac{n}{m}}, \tag{D.1}$$

$$\chi^{23}(\hat{\mathbf{u}}) = \frac{1}{bm}(1+m) \times \left(\left(1 - a\boldsymbol{\varphi}^{\mathrm{T}}\hat{\boldsymbol{\vartheta}}\right)^{-\frac{1}{m}}\left(\boldsymbol{\varphi}^{\mathrm{T}}\hat{\mathbf{s}}\right)^{\frac{1}{m}}\left(1 + \frac{\boldsymbol{\varphi}^{\mathrm{T}}\hat{\boldsymbol{\psi}}}{\psi_0}\right)^{-\frac{n}{m}} - m\right), \tag{D.2}$$

$$\chi^{24}(\hat{\mathbf{u}}) = -\frac{n}{bm\psi_0}\left(1 - a\boldsymbol{\varphi}^{\mathrm{T}}\hat{\boldsymbol{\vartheta}}\right)^{-\frac{1}{m}}\left(\boldsymbol{\varphi}^{\mathrm{T}}\hat{\mathbf{s}}\right)^{1+\frac{1}{m}}\left(1 + \frac{\boldsymbol{\varphi}^{\mathrm{T}}\hat{\boldsymbol{\psi}}}{\psi_0}\right)^{-\frac{n+m}{m}}, \tag{D.3}$$

$$\chi^{32}(\hat{\mathbf{u}}) = -\frac{a\mu}{bm}\left(1 - a\boldsymbol{\varphi}^{\mathrm{T}}\hat{\boldsymbol{\vartheta}}\right)^{-1-\frac{1}{m}}\left(\boldsymbol{\varphi}^{\mathrm{T}}\hat{\mathbf{s}}\right)^{\frac{1}{m}}\left(1 + \frac{\boldsymbol{\varphi}^{\mathrm{T}}\hat{\boldsymbol{\psi}}}{\psi_0}\right)^{-\frac{n}{m}}, \tag{D.4}$$

$$\chi^{33}(\hat{\mathbf{u}}) = -\frac{\mu}{bm}\left(1 - a\boldsymbol{\varphi}^{\mathrm{T}}\hat{\boldsymbol{\vartheta}}\right)^{-\frac{1}{m}}\left(\boldsymbol{\varphi}^{\mathrm{T}}\hat{\mathbf{s}}\right)^{-1+\frac{1}{m}}\left(1 + \frac{\boldsymbol{\varphi}^{\mathrm{T}}\hat{\boldsymbol{\psi}}}{\psi_0}\right)^{-\frac{n}{m}}, \tag{D.5}$$

$$\chi^{34}(\hat{\mathbf{u}}) = \frac{\mu n}{bm}\left(1 - a\boldsymbol{\varphi}^{\mathrm{T}}\hat{\boldsymbol{\vartheta}}\right)^{-\frac{1}{m}}\left(\boldsymbol{\varphi}^{\mathrm{T}}\hat{\mathbf{s}}\right)^{\frac{1}{m}}\left(1 + \frac{\boldsymbol{\varphi}^{\mathrm{T}}\hat{\boldsymbol{\psi}}}{\psi_0}\right)^{-\frac{n+m}{m}}, \tag{D.6}$$

$$\chi^{42}(\hat{\mathbf{u}}) = \frac{a}{bm}\left(1 - a\boldsymbol{\varphi}^{\mathrm{T}}\hat{\boldsymbol{\vartheta}}\right)^{-1-\frac{1}{m}}\left(\boldsymbol{\varphi}^{\mathrm{T}}\hat{\mathbf{s}}\right)^{1+\frac{1}{m}}\left(1 + \frac{\boldsymbol{\varphi}^{\mathrm{T}}\hat{\boldsymbol{\psi}}}{\psi_0}\right)^{-\frac{n(1+m)}{m}}, \tag{D.7}$$

$$\chi^{43}(\hat{\mathbf{u}}) = \frac{1}{b}\left(1+\frac{\boldsymbol{\varphi}^{\mathrm{T}}\hat{\boldsymbol{\psi}}}{\psi_0}\right)^{-\frac{n(1+m)}{m}} \times\left(\frac{(1+m)\left(1-a\boldsymbol{\varphi}^{\mathrm{T}}\hat{\boldsymbol{\vartheta}}\right)^{-\frac{1}{m}}\left(\boldsymbol{\varphi}^{\mathrm{T}}\hat{\mathbf{s}}\right)^{\frac{1}{m}}}{m}-\left(1+\frac{\boldsymbol{\varphi}^{\mathrm{T}}\hat{\boldsymbol{\psi}}}{\psi_0}\right)^{\frac{n}{m}}\right), \tag{D.8}$$

$$\chi^{44}(\hat{\mathbf{u}}) = -\frac{n}{bm\psi_0}\left(1-a\boldsymbol{\varphi}^{\mathrm{T}}\hat{\boldsymbol{\vartheta}}\right)^{-\frac{1}{m}}\left(\boldsymbol{\varphi}^{\mathrm{T}}\hat{\mathbf{s}}\right)\left(1+\frac{\boldsymbol{\varphi}^{\mathrm{T}}\hat{\boldsymbol{\psi}}}{\psi_0}\right)^{-\frac{n+m+mn}{m}} \times\left((1+m)\left(\boldsymbol{\varphi}^{\mathrm{T}}\hat{\mathbf{s}}\right)^{\frac{1}{m}}-m\left(1-a\boldsymbol{\varphi}^{\mathrm{T}}\hat{\boldsymbol{\vartheta}}\right)^{\frac{1}{m}}\left(1+\frac{\boldsymbol{\varphi}^{\mathrm{T}}\hat{\boldsymbol{\psi}}}{\psi_0}\right)^{\frac{n}{m}}\right). \tag{D.9}$$

When $\Lambda^h(\hat{\mathbf{u}}) \leq 0$ these functions identically vanish.

Vita

Davide Spinello was born in Latina, Italy, on July 20, 1977. In 2001 he received the Bachelor of Science degree in Environmental Engineering from the University of Roma "La Sapienza", Roma, Italy. In 2005 he earned the "Laurea" degree in Environmental Engineering with honors from the University of Roma "La Sapienza".

His research interest include computational mechanics, and micro- and nano-electromechanical systems.